NASA/CR-2004-213255

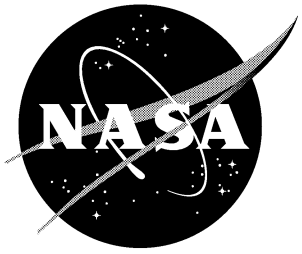

Airframe Noise Sub-Component Definition and Model

Rahul Sen
Boeing Commercial Airplane Company, Seattle, Washington

Bruce Hardy, Kingo Yamamoto, and Yueping Guo
Boeing Phantom Works, Long Beach, California

Gergory Miller
Boeing Commercial Airplane Company, Seattle, Washington

September 2004

The NASA STI Program Office . . . in Profile

Since its founding, NASA has been dedicated to the advancement of aeronautics and space science. The NASA Scientific and Technical Information (STI) Program Office plays a key part in helping NASA maintain this important role.

The NASA STI Program Office is operated by Langley Research Center, the lead center for NASA's scientific and technical information. The NASA STI Program Office provides access to the NASA STI Database, the largest collection of aeronautical and space science STI in the world. The Program Office is also NASA's institutional mechanism for disseminating the results of its research and development activities. These results are published by NASA in the NASA STI Report Series, which includes the following report types:

- TECHNICAL PUBLICATION. Reports of completed research or a major significant phase of research that present the results of NASA programs and include extensive data or theoretical analysis. Includes compilations of significant scientific and technical data and information deemed to be of continuing reference value. NASA counterpart of peer-reviewed formal professional papers, but having less stringent limitations on manuscript length and extent of graphic presentations.

- TECHNICAL MEMORANDUM. Scientific and technical findings that are preliminary or of specialized interest, e.g., quick release reports, working papers, and bibliographies that contain minimal annotation. Does not contain extensive analysis.

- CONTRACTOR REPORT. Scientific and technical findings by NASA-sponsored contractors and grantees.

- CONFERENCE PUBLICATION. Collected papers from scientific and technical conferences, symposia, seminars, or other meetings sponsored or co-sponsored by NASA.

- SPECIAL PUBLICATION. Scientific, technical, or historical information from NASA programs, projects, and missions, often concerned with subjects having substantial public interest.

- TECHNICAL TRANSLATION. English-language translations of foreign scientific and technical material pertinent to NASA's mission.

Specialized services that complement the STI Program Office's diverse offerings include creating custom thesauri, building customized databases, organizing and publishing research results ... even providing videos.

For more information about the NASA STI Program Office, see the following:

- Access the NASA STI Program Home Page at ***http://www.sti.nasa.gov***

- E-mail your question via the Internet to help@sti.nasa.gov

- Fax your question to the NASA STI Help Desk at (301) 621-0134

- Phone the NASA STI Help Desk at (301) 621-0390

- Write to:
  NASA STI Help Desk
  NASA Center for AeroSpace Information
  7121 Standard Drive
  Hanover, MD 21076-1320

NASA/CR-2004-213255

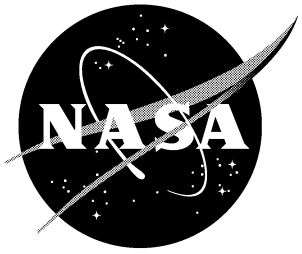

Airframe Noise Sub-Component Definition and Model

Rahul Sen
Boeing Commercial Airplane Company, Seattle, Washington

Bruce Hardy, Kingo Yamamoto, and Yueping Guo
Boeing Phantom Works, Long Beach, California

Gergory Miller
Boeing Commercial Airplane Company, Seattle, Washington

National Aeronautics and
Space Administration

Langley Research Center
Hampton, Virginia 23681-2199

Prepared for Langley Research Center
under Contract NAS1-97040

September 2004

Available from:

NASA Center for AeroSpace Information (CASI)
7121 Standard Drive
Hanover, MD 21076-1320
(301) 621-0390

National Technical Information Service (NTIS)
5285 Port Royal Road
Springfield, VA 22161-2171
(703) 605-6000

Table of Contents

List of figures

List of Tables

1 Introduction

1.1 Background

Since Fink's 1977 work (Ref. 1.1) on an airframe noise prediction scheme, there have been very few efforts to incorporate new technical results into empirical formulations of airframe noise. This is partly no doubt due to the dormant state of research in the field, in the roughly decade and half following Fink's report. However, there has been renewed activity in airframe noise under the NASA Advanced Subsonic Technology (AST) initiative. Based on early results of the AST program, an initial report on a new empirical scheme was advanced by Sen *et al* (Ref. 1.2) in 1997. The present work takes Ref. 1.2 as a starting point and attempts to add a number of improvements.

One of the main contributions of Ref. 1.2 is a new source-region classification scheme for high-lift noise. Fink's scheme was comprised of a landing-gear source and spanwise-constant high-lift sources (Ref. 1.3). In contrast, the Ref. 1.2 scheme proposed new edge sources and slat gap sources, based on newly available directional-microphone data.

At the same time, the preliminary nature of the new model was recognized in Ref. 1.2, principally due to the lack of detailed aerodynamic calculations, but also because new research on high-lift sources was at that time in its initial stages.

Thus one of the principal tasks in the current project has been the calculation of aerodynamic quantities of use to empirical noise modeling. A second task has been the incorporation of new data and new ideas about airframe noise source mechanisms. The most significant change in this respect is in the landing-gear source model. The empirical basis of this source has been completely revamped, with explicit attention paid to full-scale source features that are notoriously absent in previous work.

1.2 Summary of objectives and achievements

The main objectives of this project may be summarized as follows :

- greater number of fluid-dynamic parameters
- greater detail in source models
- more-detailed source classification scheme
- detailed landing-gear source model that incorporates full-scale spectral features
- larger database of airplanes

- inclusion of high-resolution phased-array data
- inclusion of data-based (where available) source directivity models

While progress has been good in all of these areas, it has also been somewhat uneven. This is mainly due to the relatively large effort expended on aerodynamic calculations. Consequently, acoustic modeling of the high-lift sources has not been able to take full advantage of the available aerodynamic database. A related consequence is that the trailing-edge noise source has not been updated at this point; for this source, Fink's model thus stands for the time being. On the other hand, an extensive aerodynamic database is now in place, providing a solid foundation for subsequent source-model refinements.

Source directivity modeling is another area in which progress was somewhat hampered, in this case due to a scarcity of experimental data.

The greatest changes at this stage are in the landing-gear model, despite the currently limited availability of full-scale gear-noise data. The model presented here establishes a totally new paradigm for landing-gear source components, much as Ref. 1.2 did for sources associated with the high-lift system.

1.3 References for this chapter

Ref. 1.1 : M.R. Fink, *Airframe Noise Prediction method,* Federal Aviation Administration Report FAA-RD-77-29 (1977)

Ref. 1.2 : R. Sen, A. Blackner, P. Yee, and R. Stoker, *Airframe Noise Generation and Radiation,* NASA informal Contractor Report, contract NAS1-20090, Task 2 (1997); also released as Boeing Document D6-81956TN.

Ref. 1.3 : R. Sen, Assessment of the NASA ANOPP method of airframe-noise prediction from a noise-reduction point of view, Boeing Document D6-81619TN (1995).

2 Acoustic Data Processing

2.1 *Introduction*

The acoustic database consists of elliptic mirror data for B737, B757 and B777 and phased microphone array data for B767, DC10 and MD11. The former is also the database used by Boeing to develop the original component-based prediction models (Yee *et al* 1996), while the latter is made available only in recent years (under the NASA AST Program). In addition, free microphone data are also available for DC10 and MD11, not only at the fly-over location, but also in other directions. Thus, these data are used to develop directivity models. To derive the prediction models for the individual components of the high lift system, a methodology is developed for the data processing, which can be summarized as

- analyze the source map to identify major noise sources;
- determine sub-regions of main sources;
- identify main aerodynamic parameters for each sub-component;
- integrate source map to derive far field spectra for sub-components;
- calibrate integrated spectra with free microphone data;
- apply corrections to small-scale data;
- extrapolate data to full-scale at certification conditions.

In this chapter, this process of processing the acoustic data is described in detail, together with discussions on the methods and hypotheses used in each step. After the data are processed, a regression analysis is then applied to derive empirical prediction formula for all the components, which is described in the next chapter.

2.2 *Sub-component Sources*

The source maps from the phased microphone array and the elliptic mirror can be used to identify major sources and hence to define sub-regions for the source integration. To illustrate, Figure 2-1 shows the source map for the 4.7% DC10 model at 6 kHz with M=0.207 and the flaps and slats respectively deployed at 35 and 20 degrees. At this frequency, the source map shows a dominant source at the outboard edge of the outboard flap. Other sources with relatively smaller amplitudes are also seen at the flap inboard edges and the leading edge slat location. To further quantify the relative importance of the sources at different locations, we choose a few cuts on the source map and plot the source strength along these cuts. The cut locations are shown in Figure 2-1 and the source strengths along these cuts are plotted in Figure 2-2. Cut 1 goes through the

dominant source at the outboard edge of the outboard flap. The source strength plot (the top diagram in Figure 2-2) clearly shows the dominance of this source. Along this cut, the flap source is at least 15 dB stronger than other sources. When the cuts are taken at other locations, other sources are revealed very clearly. Cut 2 (the second diagram from the top in Figure 2-2) is at the inboard flap edges and shows both the flap and the slat sources. At this location, the amplitudes of these two sources are quite comparable. By comparing the top two diagrams in Figure 2-2, it is clear that the source at the outboard edge of the outboard flap has much stronger source strength than those at the slat locations (about 9 dB stronger). This however does not necessarily mean that the slat sources are less important. This is because though the slat sources have weaker strengths, they have a much larger source area than the flap source. The far field noise is determined by the integration of the source strength over the source area. Thus, a weaker source distribution with a larger source area may lead to more noise in the far field. This also applies to the trailing edge sources. These sources have weaker strengths but are distributed over an extensive region basically covering the entire wing span. The bottom two diagrams in Figure 2-2 illustrate this very clearly. Cut 3 in this figure is approximately at the middle span location of the outboard flap. Two sources are seen at this location, namely the slat source and the trailing edge source. The trailing edge source is weaker than the slat source by about 1.5 dB (and hence still weaker than the flap source). Note also that the trailing edge source does not show up at all in the source map in Figure 2-1 because of the cutoff of the color scheme in the plotting procedure. The bottom diagram in Figure 2-2 shows the extensive distribution of the trailing edge sources. This is a cut at a location close to the wing tip where no other sources are present. However, the trailing edge source is clearly seen there and furthermore its strength is basically the same as that at the middle span location (Cut 3), indicating almost constant source strength along the span.

Based the analysis of the source maps and the source strengths at different locations, we divide the wing area into sub-regions for the component analysis. The sub-regions are used for source integration to derive far field spectra. They also correspond to sub-components of the wing/high lift system, each of which may have different noise generation mechanisms. There are altogether six components

- leading edge slat;
- outboard flap edge;
- inboard flap edge;
- trailing edge;
- high-speed aileron;
- residue noise floor.

Two examples of the definitions for the sub-regions are illustrated in Figure 2-3 for the DC10 and the B767 model. For other models, the sub-regions are similarly defined. It is appropriate to point out that this definition of sub-regions does involve a certain degree of arbitrariness, especially in the shapes and sizes of the sub-regions. For example, the high-speed aileron component is defined as a rectangular region close to the wing tip. This region actually contains some trailing edge sources. It is not further divided for the sake of simplifying the computations. The arbitrariness in the definition of the sub-regions, however, does not pose a severe limitation on the analysis for two reasons. The first is that the sub-regions are always required to cover the entire wing area so that the sum of the noise components is always equal to the total noise of the wing, though the noise components themselves may vary with different definitions of the sub-regions. The second reason is that the sub-regions are required to contain the respective dominant sources in the regions. Since the dominant sources are much stronger than other sources within each sub-region, the variations in shape and size of the sub-region definition is not very critical in the source strength integration. The integration is dominated by the major sources. It should also be noted that the locations and the sizes of the sub-regions are frequency-dependent. As frequency varies, the source characteristics also change. Thus, the decomposition of the sources should also change with frequency.

2.3 Integrated Spectra

Once the sub-regions are defined, the noise spectra for each sub-component can be derived by integrating the source strengths. The technique is standard, involving summing all the beam-forming steering points within a sub-region and dividing the result by the calibration integral. The latter basically established the relation between the source integration and the far field spectrum. In summing the source strengths, a local maximum is identified within each sub-region at each frequency so that contributions more than 6 dB below the local maximum are ignored in the summation. This is to ensure the exclusion of side-lobes in the integration. This works well with sub-regions that contain dominant sources with well-defined local maximum. For sub-regions with no apparent dominant source, such as the residue component and the high-speed aileron component at some frequencies, the 6 dB cutoff may include some side-lobe contributions in the integration, which causes spectral build-up in the far field spectral, especially at high frequencies. This in turn affects the total noise when the components are added. To demonstrate this, Figure 2-4 shows the integrated component spectra for both the 4.7% DC10 and the 6.3% B767 model. The operation conditions are all shown in the figure. All the major components show a negative slope, which is expected. The residue term and the high-speed aileron term, however, show trends of noise increases with frequency. The build-up of the

spectrum for the two exceptions is due to the fact that there is no dominant source in these two sub-regions at high frequencies so that the 6 dB cutoff includes contributions from the side-lobes that are not physically real. Thus, this kind of spectral build-up must be corrected. This is done mainly by imposing a fall-off with frequency. The precise form of the fall-off is not critical because the components that need correction are usually not the dominant components; their contributions to the total noise are not noticeable. An example of this kind of correction is shown in Figure 2-5 for the B767 model.

With the spectral build-up corrected, the total integrated spectra can be compared with those taken by free field microphones. Some examples are given in Figure 2-6 for the 4.7% DC10 model, for which free microphone data are available. The comparisons are clearly favorable with quite satisfactory results for both the spectral shapes and the absolute amplitudes. Further comparison can be made for the B737, B757 and B767 models, which are shown in Figure 2-7 for the inboard flap edge source. The data for the first two (B737 and B757) are taken by the elliptic mirror while those for the B767 are from the integrated phased microphone array. Evidently, both the spectral shapes and the absolute levels of the spectra show quite reasonable comparison, validating the method for deriving the spectra from beam-forming source maps.

2.4 Extrapolation to Full-Scale

According to conventional procedures (Yee *et al* 1996; Allen *et al* 1997; Hayes *et al* 1997), the critical parameter in the extrapolation process is the ratio of the model dimension to that of the full scale aircraft. This ratio is important because both frequencies and amplitudes are scaled by it. The extrapolation procedure is quite straightforward and has been previously described. Thus, it will be described here only very briefly. The process basically involves first extrapolating the measured wind tunnel data from the microphone locations to unit distance from the assumed source location. This essentially scales out the effects of spherical spreading, as well as atmospheric absorption under the test day conditions. The second step is then to scale the results at unit distance from the source from small scale to full scale, which involves scaling the frequencies down and amplitudes up, both by the model dimension ratio. The scaled data are then extrapolated to the far field, typically the certification distance of 394 feet away from the aircraft center. By doing so, the losses due to spherical spreading and atmospheric absorption at standard acoustic day conditions are accounted for.

Following this procedure, the small-scale data can be extrapolated to full-scale at certification conditions. The extrapolated results, however, do not agree well with full-scale measurements. Some examples are shown in Figure 2-8 for the DC10 model and the B767

model. The comparisons in this figure are reasonably good for frequencies below about 500 Hz, but shows significant discrepancies for higher frequencies. The extrapolated data significantly underestimate the fly-over data in the middle and high frequency region by as much as 10 dB. It is apparent that our limited database does not allow us to satisfactorily understand the reasons for these large discrepancies. Thus, we postulate that the small scale of the model aircraft may cause quite different flow behavior from that of the full scale aircraft, as is commonly described as Reynolds number effects.

An attempt to derive a correction for the Reynolds number effects has been made recently (Guo *et al* 1998). In this case, we argue that the dominant length scale in the flow should be dependent on the Reynolds number, instead of the physical dimension of the model aircraft. There are many cases in which the flow is governed by a length scale dependent of the flow conditions, turbulent boundary layer flow being a typical example where the thickness of the boundary layer is determined by the local Reynolds number (Blake 1986). If this idea holds for the flow surrounding the high lift system of the aircraft, it implies that the procedure for the extrapolation from small to full scale should be modified. In particular, the length scale extrapolation should depend on the flow conditions, as well as the physical dimensions of the models. One consequence of this is a quite different frequency scaling law from that in the conventional approach described earlier in this section. The difference between the two is quite significant for models smaller than about 10% of the full-scale aircraft. For example, for the 4.7% DC10 model, the scale-down of the small scale frequencies should be done by the factor 0.087, when the Reynolds number effects are taken account of, instead of 0.047 as in the conventional extrapolation procedures. With this correction alone, the comparison between the extrapolated data and flight data can be greatly improved. This is demonstrated in Figure 2-9. Clearly, the comparison between small-scale data and full-scale data becomes much more satisfactory than that in Figure 2-8. When both frequency and amplitude corrections are applied, the extrapolated data agree very well with full-scale measurements in the entire frequency domain. To clearly demonstrate the Reynolds number corrections, the lower diagram (for the B767 model) also includes the curve without any correction and the curve with only frequency correction. The set of curves thus shows the progressive improvement achieved by the Reynold number corrections.

2.5 References for this chapter

Allen C. S. & Soderman P. T. 1997 Scaling and extrapolating small-scale in-flow wind tunnel jet noise to full scale fly-over jet noise. *AIAA Paper 97-1602.*

Blake W. K. 1986 *Mechanics of Flow-Induced Sound and Vibration.* Academic Press.

Guo Y. P. 1998 A semi-analytical/semi-empirical model for flap side edge noise prediction. NASA Contract Report, CRAD-93-TR-3765.

Guo Y. P., Bent P., Yamamoto K. & Joshi M. 1998 Surface pressure fluctuations on DC-10 high lift system and their correlation with far field noise. NASA Contract Report CRAD-9310-TR-4872.

Guo Y. P., Hardy B. A., Bent P., Yamamoto K. & Joshi M. C. 1998 Noise characteristics of DC-10 aircraft high lift system. NASA Contract Report CRAD-9310-TR-4893.

Guo Y. P., Stoker B., Hardy B. A., Bent P. & Joshi M. 1998 DC-10/MD-11 acoustic test in NASA Ames 12-ft pressurized wind tunnel. NASA Contract Report CRAD-9310-TR-4894.

Hayes J. A., Horne W. C., Soderman P. T. and Bent P. H. 1997 Airframe noise characteristics of a 4.7% scale DC-10 model. *AIAA Paper 97-1594.*

Yamamoto K. J., Donelson M. J., Huang S. C. & Joshi M. C. 1995 Airframe noise prediction evaluation. NASA Contract Report 4695.

Yee P., Underbrink J. R., Sen R., Kusunose K., Dougherty R. & Blackner A. M. 1996 Airframe noise generation and radiation. NASA Contract Report.

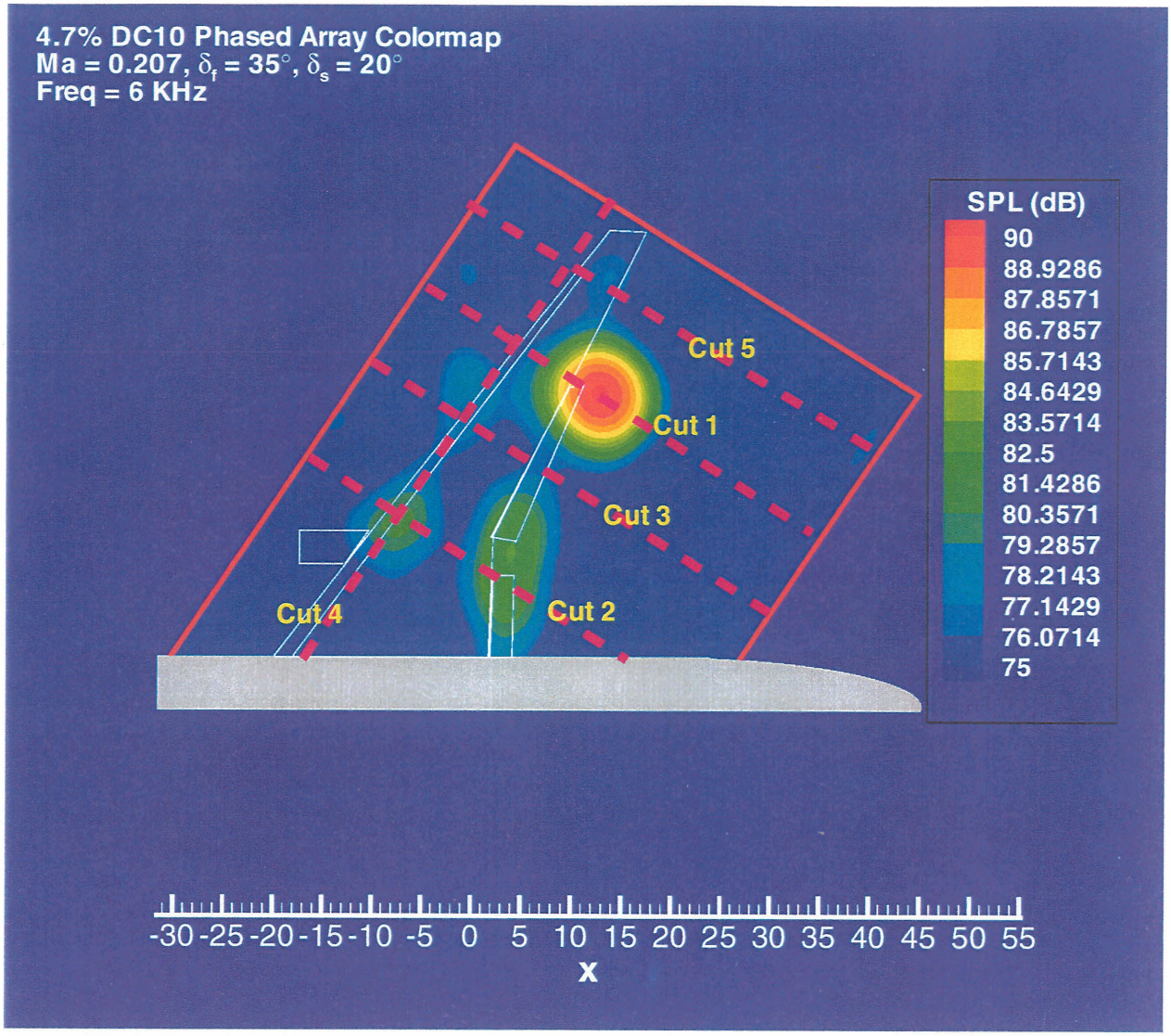

Figure 2-1 Source map for the 4.7% DC10 model from phased microphone array data. The source strengths along the cuts are shown in figure 2.

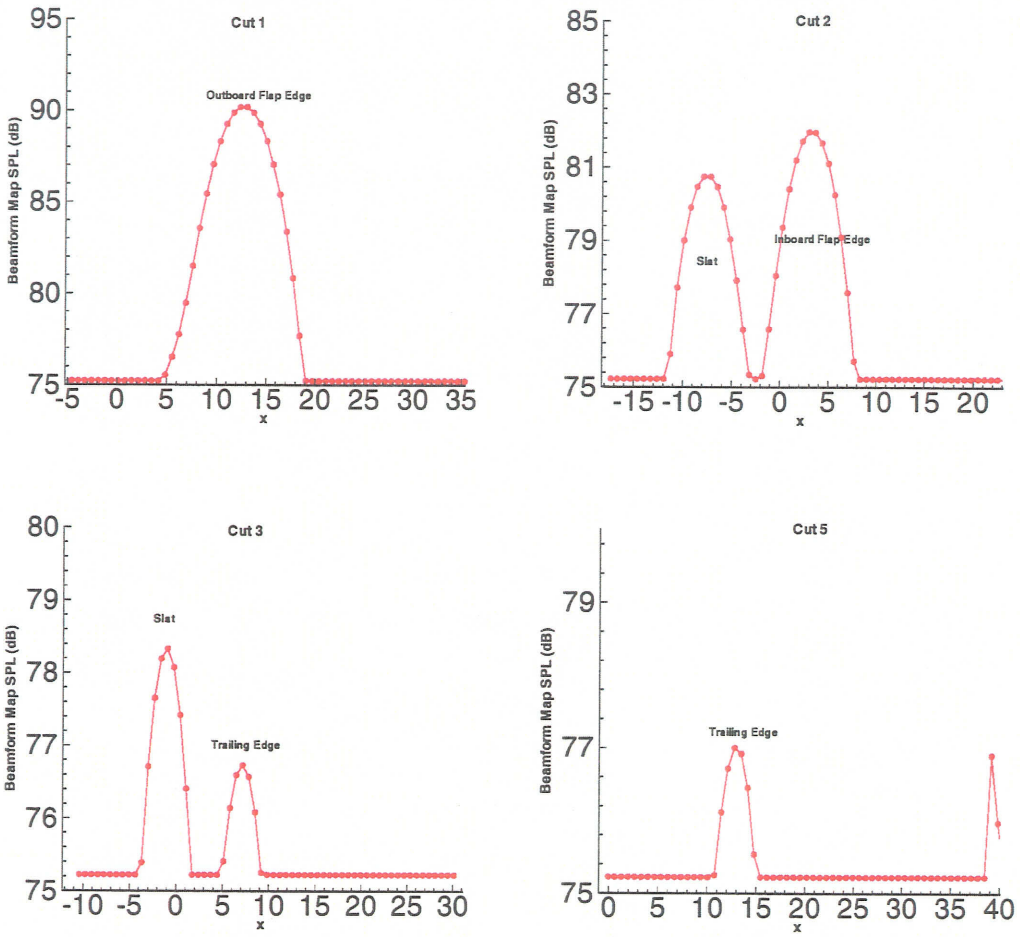

Figure 2-2 Source strengths along some cuts at different span-wise locations for the 4.7% DC10 model. The locations of the cuts, together with the flow conditions and high lift system settings, are given in figure 1.

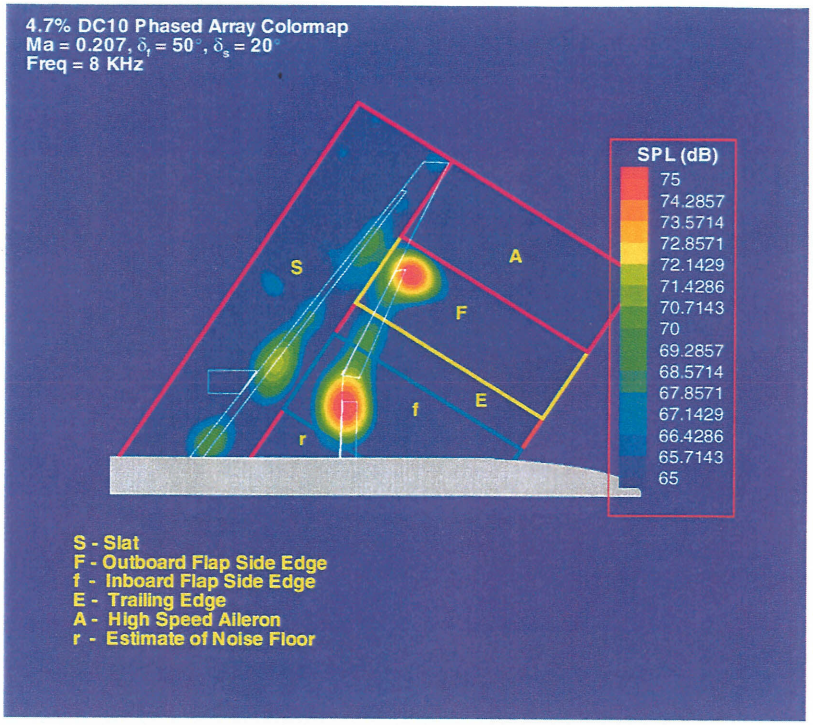

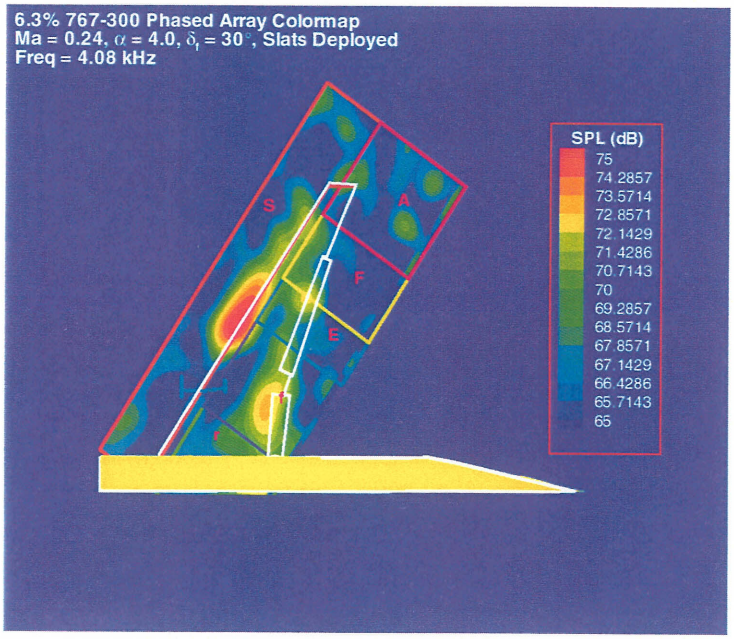

Figure 2-3 Definitions of the sub-regions for component analysis for the 4.7% DC10 and the 6.3% B767 model. Note that the definitions (locations and sizes) of the sub-regions are frequency-dependent because of the changing characteristics of the sources with frequency.

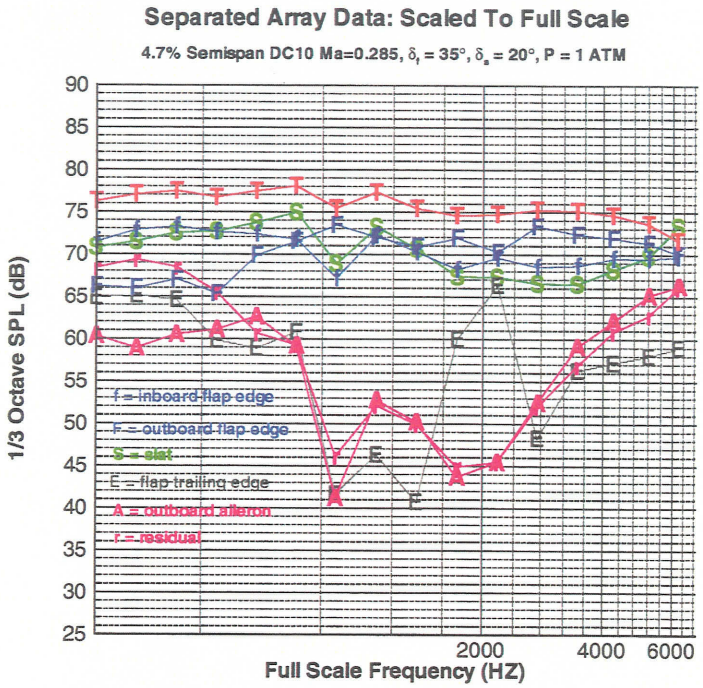

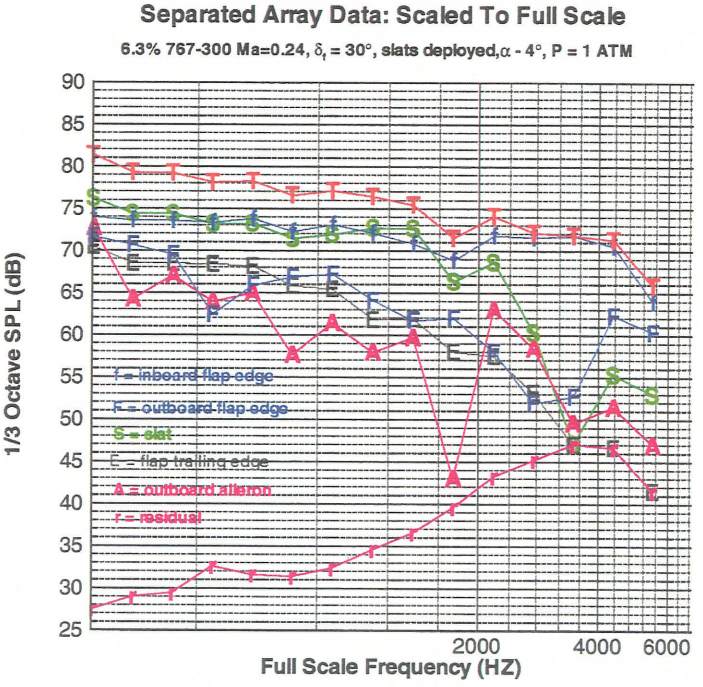

Figure 2-4 Examples of the integrated spectra for the sub-components.

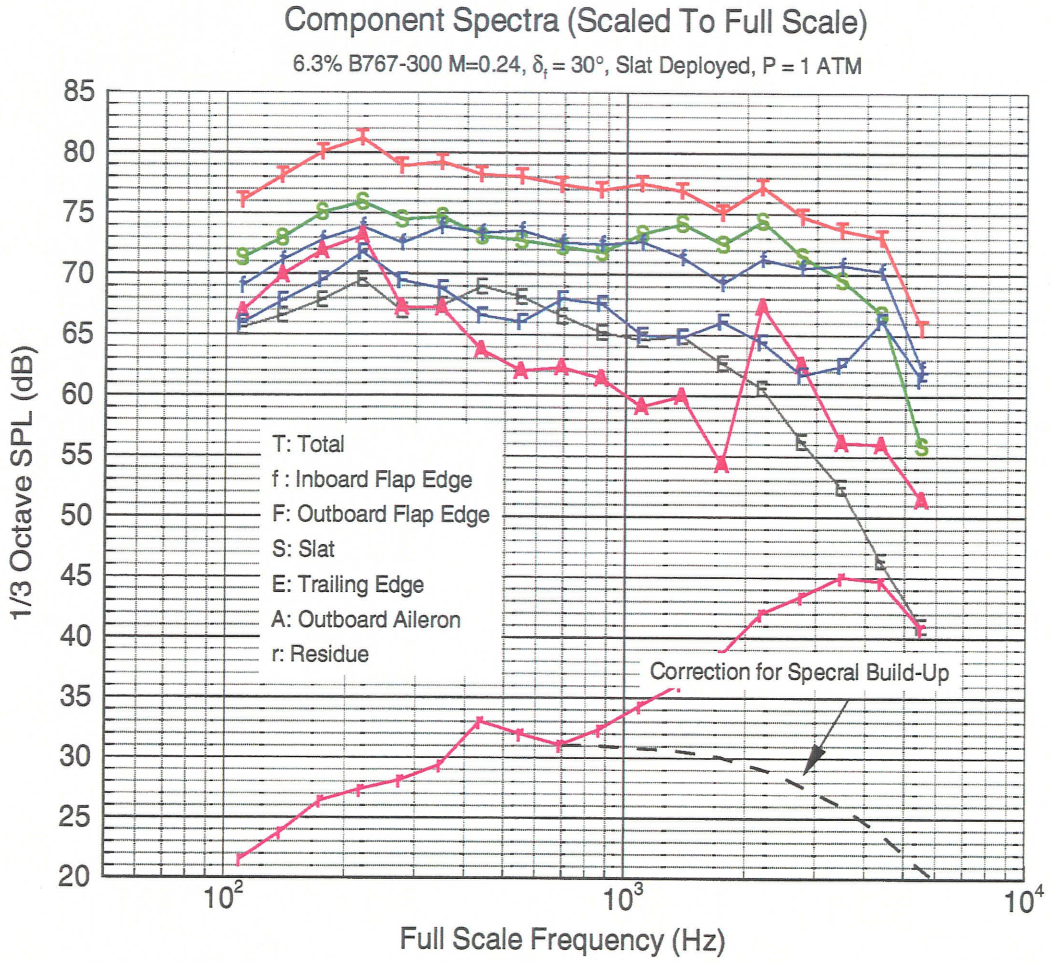

Figure 2-5 Correction for spectral build-up (indicated by the broken black lines).

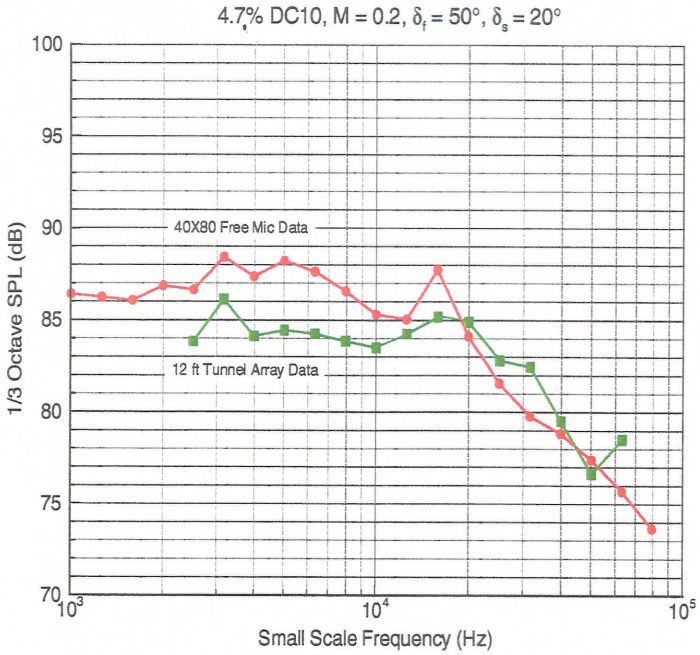

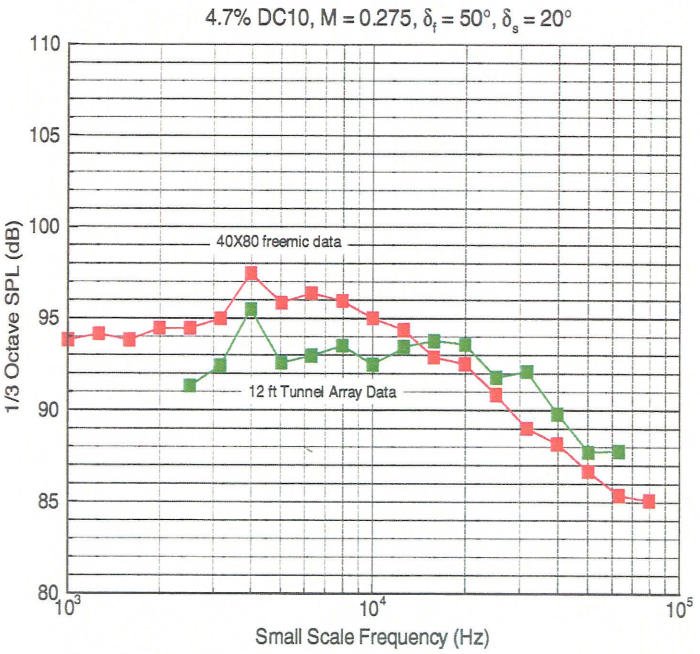

Figure 2-6 Comparisons between integrated spectra and free field microphone measurements.

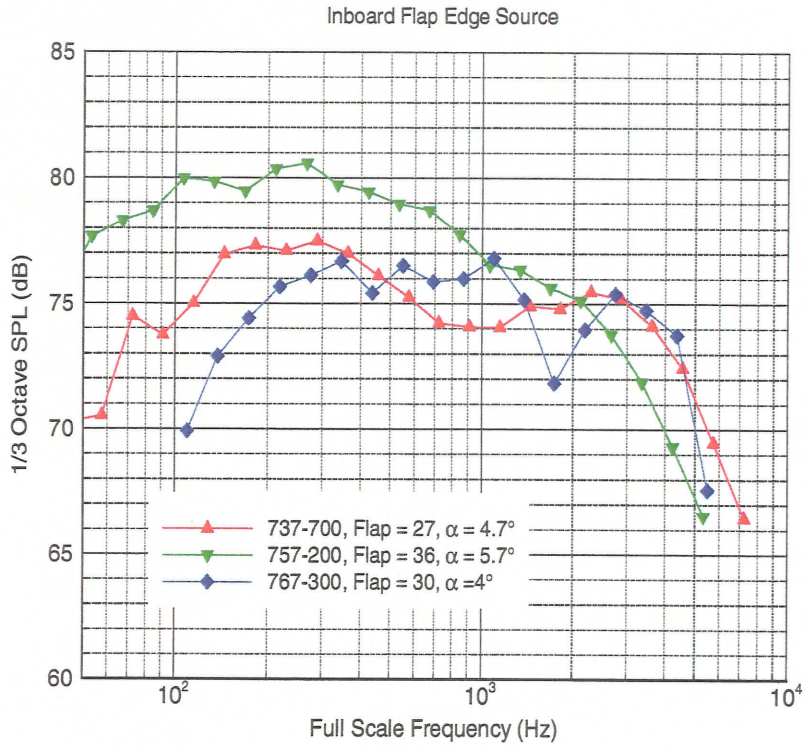

Figure 2-7 Comparisons between elliptic mirror data and phased microphone array data.

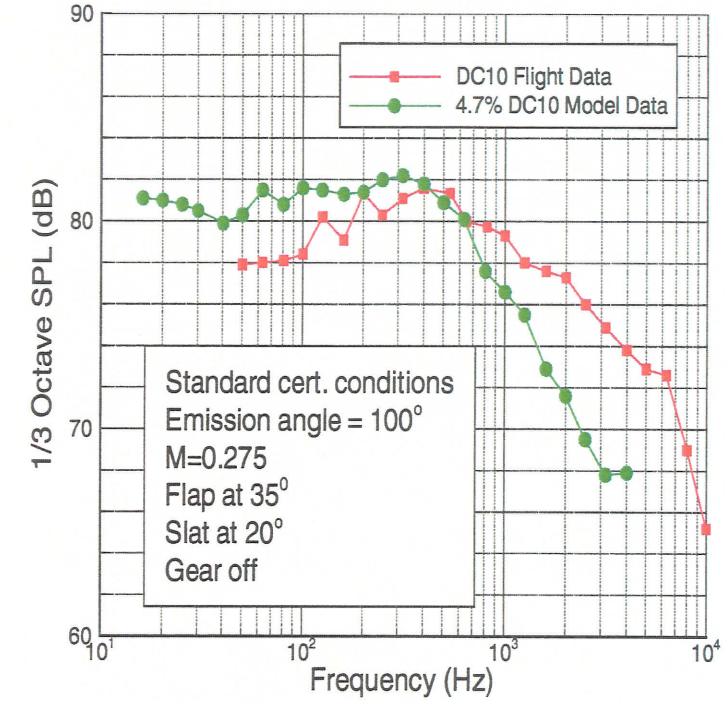

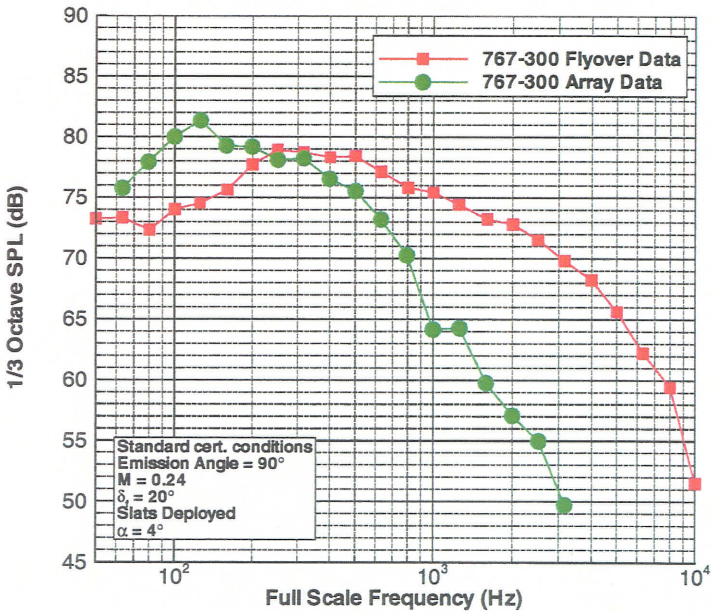

Figure 2-8 Comparisons between extrapolated data and full-scale measurements. The upper diagram is for the DC10 model and the lower diagram for the B767 model.

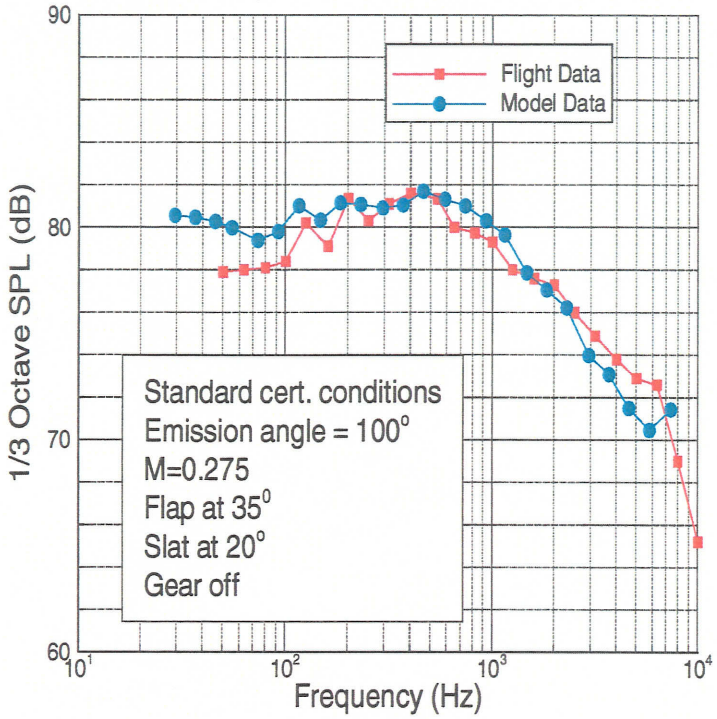

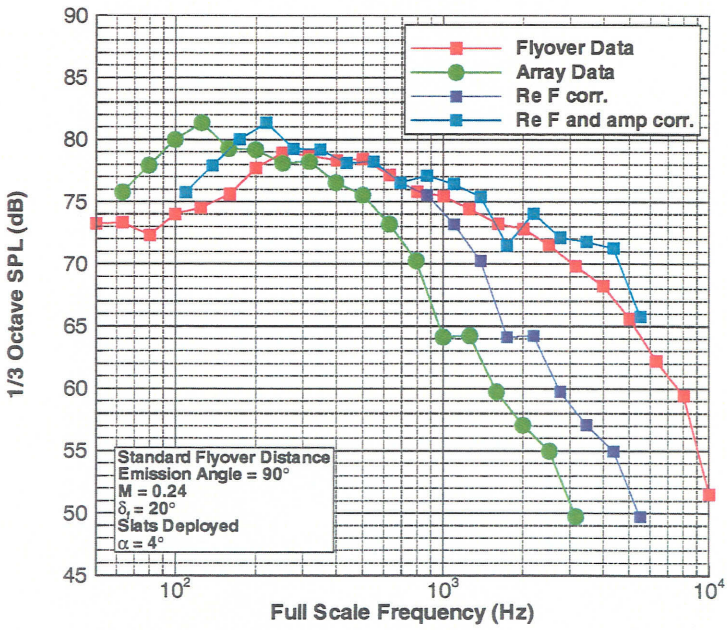

Figure 2-9 Improvement of comparisons between extrapolated and full-scale data by Reynolds number effect corrections.

3 Regression Analysis of Acoustic Data

3.1 General Approach

In the present study, two sets of data base were used. The integrated output of phased array microphone data were used to determine one-third-octave spectra at 90°. The directivity factor for OASPL was determined based on the DC-10 scale model test data. The one-third-octave spectrum for each airframe noise (outboard aileron, inboard flap side edge, outboard flap side edge and slat) at 90° was determined in two steps.

First, OASPL was correlated to the key aerodynamic and geometric parameters associated with the component source in concern. Then, (SPL – OASPL) was normalized in terms of logarithmic Strouhal number. The directivity factor defined as the difference in SPL(θ, f) at $\theta = 90°$ and desired emission angle was determined with the DC-10 scale model test data over a range of emission angle ($10° \leq \theta \leq 170°$).

3.2 Prediction Method for Component Noise

Airframe noise components considered in the present study are outboard aileron noise, inboard flap side edge noise, outboard flap side edge noise and slat noise. Acoustic data from a total of 126 runs were analyzed to develop prediction methods for these airframe noise components. The far-field acoustic data are projected to the overhead distance (394 ft) of the certification approach. The data include noise reduction by the atmospheric absorption.

3.2.1 Outboard Aileron Noise:

The aerodynamic and geometry parameters used to correlate to outboard aileron noise included flow Mach number, angle of attack and semi-span (of wing). Since geometry information about outboard aileron was not available, the chord of the outboard primary flap element was used together with the lift coefficient of this flap element. In addition, the outboard flap deflection angle was also taken into account to address the aileron noise. Using the multiple linear regression method far-field OASPL(90°) was correlated to these parameters. It was found that a fixed value for the power index of flight Mach number tends to give some- what larger values for larger aircraft (which means that this power index is configuration dependent.) This difficulty was solved by relating the power index to the semi-span.

The one-third-octave spectra were normalized in terms of logarithmic Strouhal number defined using the effective length scale ($\xi \cdot t$) and local flow velocity. In the present study the length scale factor, ξ was assumed to be unity. The normalized spectrum is determined by a curve-fitting in terms of the 6^{th} order polynomial equation , which is illustrated in Figure 3-1. In the following, the OASPL correlation and the formulation for the normalized spectrum are shown.

$$OASPL(90°) = 109.7 + n \cdot Log(M) + 3.36Log(C_{l^\circ} \cdot Sin\ \delta) + 3.46Log(Sin\ \alpha) + 3.46Log((\xi \cdot t)$$

$$n = 52 - 5.8565 \times (Z - 1); \quad Z = b/47.4$$

$$SPL(f, 90°) - OASPL(90°) = a_6 \cdot X^6 + a_5 \cdot X^5 + a_4 \cdot X^4 + a_3 \cdot X^3 + a_2 \cdot X^2 + a_1 \cdot X + a_o$$

$$X = Log(f \cdot \xi \cdot t / V)$$

a_0	a_1	a_2	a_3	a_4	a_5	a_6
-14.0467	9.0187	-6.4007	-4.3267	2.1149	5.7254E-1	-7.062E-1

M = Flight Mach number, C_l = Lift coefficient for outboard flap (1^{st} flap element),
δ = Flap deflection angle, t = Outboard flap edge chord (1^{st} element), α = Angle of attack,
V = Flight velocity, f = One-third-octave center frequency ,
b = Semi-Span, ξ = length scale factor

Note: Arguments of logarithmic function are non-dimensionalized by reference values.

3.2.2 Flap Side Edge Noise:

The aerodynamic and geometry parameters associated with flap side edge noise modeling included flight mach number, flap deflection angle, lift coefficient, chord length , cross flow velocity and circulation.

For both inboard and outboard flaps, only the primary (first) flap element was considered. The multiple linear regression yielded almost identical power index for inboard and outboard flap side edge noise components except that for the chord length. The regression analysis showed that both cross flow velocity and circulation around the primary flap element practically have no effect on the flap side edge noise. This result may be contradictory to theory. Further detailed analysis would be needed to investigate this issue. The length scale factor ξ was set equal to unity for both inboard and outboard flap cases.

3.2.2.1 Inboard Flap Side Edge Noise

For inboard flap edge noise modeling, the aerodynamic and geometry parameters related to the primary flap element of the inboard flap assembly. The regression analysis showed that

OASPL at overhead direction is proportional to the flight Mach number raised to the 5.3th power, square of sine of flap angle and roughly square of effective chord length. The lift coefficient, together with cross flow velocity and circulation, appears to have no effect on the overall sound pressure level at this emission angle. The normalization of one-third-octave spectrum was performed in terms of Strouhal number calculated with the effective chord as its length scale. Figure 3-2 shows the normalized spectra for the inboard flap side edge noise component. The normalized spectrum is determined by a curve-fitting in terms of the 6^{th} order polynomial equation , which is illustrated in Figure 3-2. In the following, the OASPL correlation and the formulation for the normalized spectrum are shown.

$$OASPL(90°) = 92.1 + 53.0Log(M) + 20.15Log(\text{Sin}\,\delta) + 0.5Log(C_l) + 17.8Log(\xi \cdot t) + 0.11Log(V_y) + 0.12Log(\Gamma)$$

$$SPL(f, 90°) - OASPL(90°) = a_6 \cdot X^6 + a_5 \cdot X^5 + a_4 \cdot X^4 + a_3 \cdot X^3 + a_2 \cdot X^2 + a_1 \cdot X + a_o$$
$$X = Log(f \cdot \xi \cdot t / V)$$

a_0	a_1	a_2	a_3	a_4	a_5	a_6
-13.1814	10.0319	-9.4077	-6.6166	4.0970	1.4162	-1.0740

M = Flight Mach number, C_l = Lift coefficient for inboard flap (1^{st} flap element),
δ = Flap deflection angle, t = Inboard flap edge chord (1^{st} element), V_y = Spanwise flow velocity,
Γ = Circulation, V = Flight velocity, f = One-third-octave center frequency,
ξ = length scale factor

Note: Arguments of logarithmic function are non-dimensionalized by reference values.

3.2.2.2 Outboard Flap Side Edge Noise

As mentioned above, the dependency of overall sound pressure level at the overhead direction for the outboard flap side edge noise component on its related aerodynamic and geometry parameters is very much similar to that for the inboard flap side edge noise component. Only difference observed is the dependency on the chord length. It was found that a fixed value for the power index for the chord length tends to yield somewhat larger values for larger aircraft. This difficulty, however, was overcome by relating the power index to the semi-span. As for the inboard flap side edge noise, the one-third-octave spectra were normalized in terms of Strouhal Number defined using the effective chord length. The normalized spectrum is determined by a curve-fitting in terms of the 6^{th} order polynomial equation , which is illustrated in Figure 3-3. In the following, the OASPL correlation and the formulation for the normalized spectrum are shown.

$$OASPL(90°) = 93.3 + 53.0Log(M) + 20.15Log(\sin\delta) + 0.5Log(C_l) + m\cdot Log(\xi\cdot t) + 0.11Log(V_y) + 0.12Log(\Gamma)$$
$$m = 10 \times (b_3\cdot Z^3 + b_2\cdot Z^2 + b_1\cdot Z + b_0) \quad Z = b/47.41$$

$$SPL(f, 90°) - OASPL(90°) = a_6\cdot X^6 + a_5\cdot X^5 + a_4\cdot X^4 + a_3\cdot X^3 + a_2\cdot X^2 + a_1\cdot X + a_o$$
$$X = Log(f\cdot\xi\cdot t / V)$$

b_0	b_1	b_2	b_3
4.1204	-6.2200	5.5040	-1.6245

a_0	a_1	a_2	a_3	a_4	a_5	a_6
-14.5121	9.1991	-4.7859	-3.8899	1.3238	4.1053E-1	-5.8664E-1

M = Flight Mach number, C_l = Lift coefficient for outboard flap (1st flap element),
δ = Flap deflection angle, t = Outboard flap edge chord (1st element), V_y = Spanwise flow velocity,
Γ = Circulation, V = Flight velocity, f = One-third-octave center frequency
b = Semi-span, ξ = length scale factor

Note: Arguments of logarithmic function are non-dimensionalized by reference values.

3.2.3 Slat Noise:

The aerodynamic and geometry parameters used to correlate to slat noise included flow Mach number, angle of attack, lift coefficient and effective slat chord length. Probably, slat angle and mass flow rate through the slat gap should be considered in modeling. Unfortunately, these parameters were not available when the correlation was performed. A detailed analysis of the data showed that the behavior of DC-10 and MD-11 slat noise is significantly different from that for other aircraft configurations analyzed in the present study (such as 737, 757, 767 or 777). Because of this reason, the slat noise data from DC-10 and MD-11 was excluded in the multiple linear regression analysis. In practical application, however, the slat noise data determined from B767-400 may be used as a substitute for DC-10 or MD-11. As in the case of aileron noise modeling, the value of the power index for flight Mach number was defined as a function of semi-span for better match to the data. Again, the one-third-octave spectra were normalized in terms of Strouhal Number defined using the effective slat chord length. The normalized spectrum is determined by a curve-fitting in terms of the 6th order polynomial equation , which is illustrated in Figure 3-4. In the following, the OASPL correlation and the formulation for the normalized spectrum are shown.

$$OASPL(90°) = 117.4 + n\cdot Log(M) + 10.3Log(\sin\alpha) + 44.5Log(C_l) + 11.5Log(\xi\cdot t)$$
$$n = 10\times(c_2\cdot Z^2 + c_1\cdot Z + c_0);\ Z = b/47.41$$

$$SPL(f, 90°) - OASPL(90°) = a_6 \cdot X^6 + a_5 \cdot X^5 + a_4 \cdot X^4 + a_3 \cdot X^3 + a_2 \cdot X^2 + a_1 \cdot X + a_o$$
$$X = Log(f \cdot \xi\, t / V)$$

c_0	c_1	c_2
7.600	-4.1355	1.7486

a_0	a_1	a_2	a_3	a_4	a_5	a_6
-12.7289	4.05419	-4.3004	-1.8453	1.9039E-1	2.1658E-1	-3.9728E-1

M = Flight Mach number, C_l = Lift coefficient for slat, t = Slat chord, α = Angle of attack
V = Flight velocity, f = One-third-octave center frequency, b = Semi-span ,
ξ = length scale factor

Note: Arguments of logarithmic function are non-dimensionalized by reference values.

3.2.4 Directivity Factor D(θ,f)

The directivity factor which is applied to SPL(90°,f) to define SPL(θ,f) was developed based on the analysis of free microphone data of the DC-10 scale model test. The directivity factor D(θ,f) is related to the reference SPL(90°,f) as

$$10*Log\{D(\theta,f)\} = SPL(\theta,f) - SPL(90°,f)$$

As noted in Figure 3-5, the OASPL directivity of DC-10 total airframe noise (excluding landing gear noise) is relatively flat. In addition, as noted in Figure 3-6, the spectral shape also shows weak directivity dependency. However, to address observed minor variations in the high frequency region (see Figure 3-6) Δ SPL(θ,f) = SPL(θ,f) – SPL(90°,f) was defined as quadratic equation of Strouhal number at each emission angle shown below by applying curve-fitting. The effective length scale, D was estimated from the peak frequency at 90°, assuming that the peak Strouhal number is unity.

$$10*Log\{D(\theta,f)\} = a_2 \cdot X^2 + a_1 \cdot X + a_o$$
$$X = X = Log(St), \quad St = f*D/V$$

The coefficients of this equation are listed in the following table.

θ	a_2	a_1	a_o
25	-0.3897	-0.5585	-2.13
32	-0.4547	-0.4823	-1.16
39	-0.4792	-0.2639	-0.4
48	-0.5964	-0.0682	0.08
57	-0.5097	-0.0378	0.47
68	-0.4392	0.0494	0.4
80	-0.3839	-0.0588	0.34
90	0	0	0
106	0.1552	-0.0665	-0.85
120	0.1565	-0.1438	-1.39
133	-0.0426	-0.7227	-2.01

3.3 Validation of Prediction Method

Limited comparison of the present model with flyover airframe noise data was made. Figure 3-7 shows data versus prediction comparison for a narrowbody aircraft (B737) at typical approach conditions. Reasonably good agreement is noted. The present model seems to capture general features of airframe noise. Figure 3-8 shows a similar comparison with DC-10 flyover data. In this comparison, the predicted

SPL does not include landing gear noise. However, due to rather high flight Mach number (M = 0.26) and a large flap angle (δ = 50°), the relative magnitude of landing gear noise is believed to be much smaller than flap side edge noise or slat noise. Addition of landing gear noise may slightly increase low frequency noise.

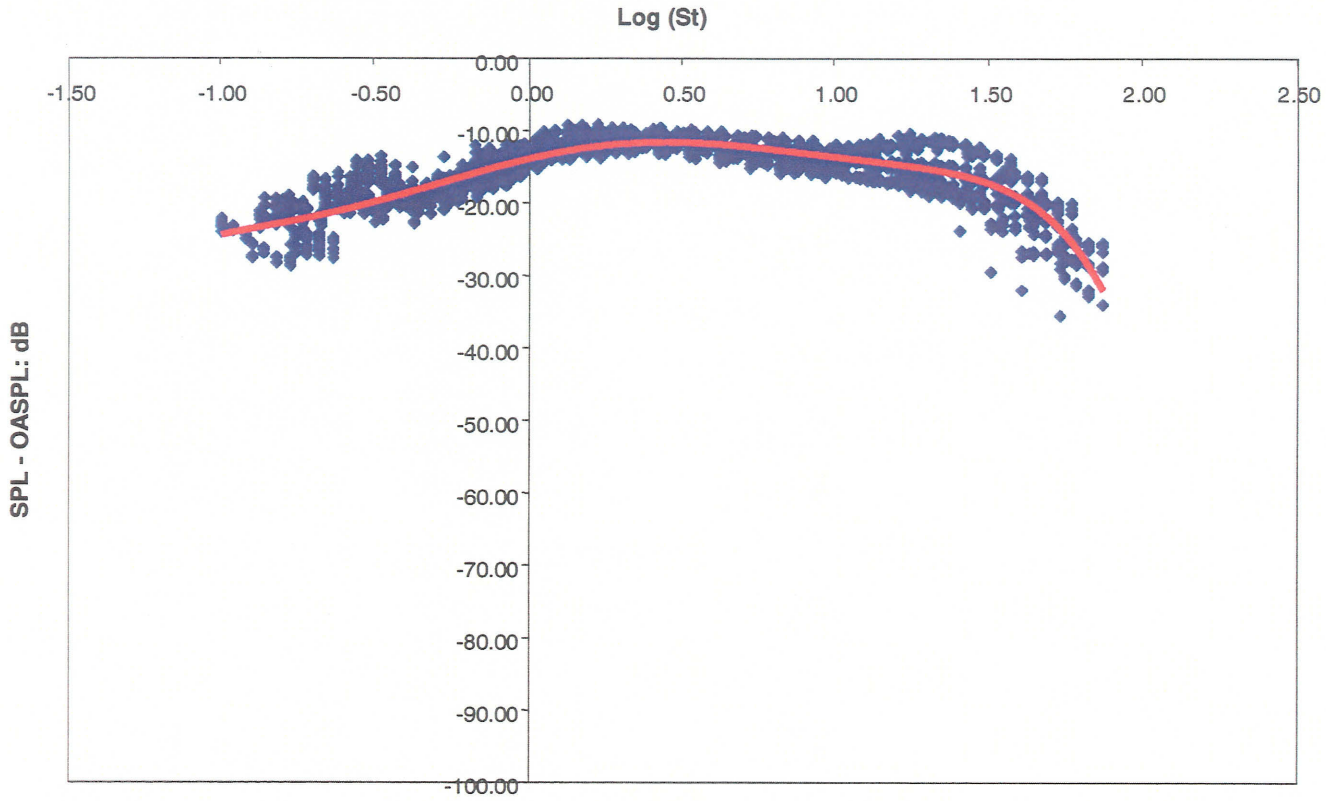

Figure 3-1 Airframe noise, outboard ailerons :normalized spectra

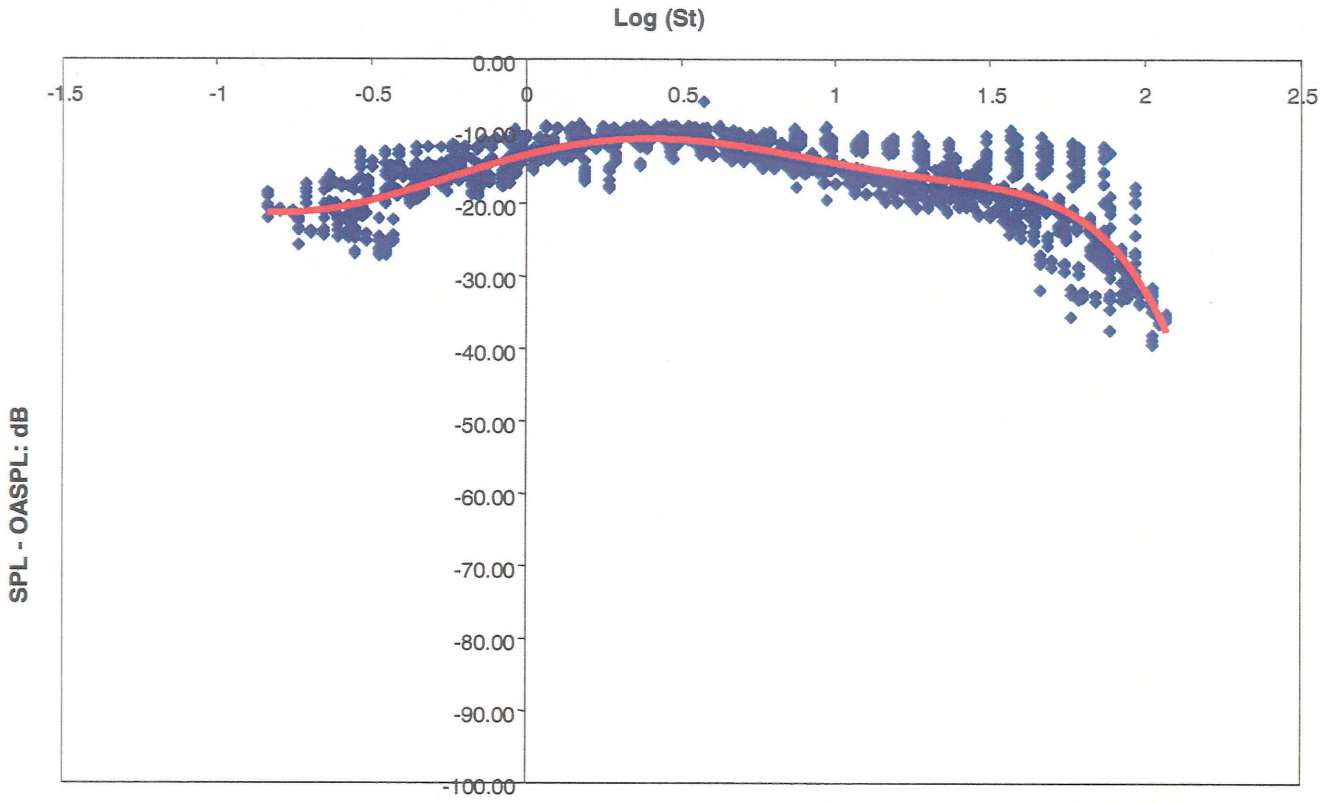

Figure 3-2 Airframe noise, inboard flap edge : normalized spectra

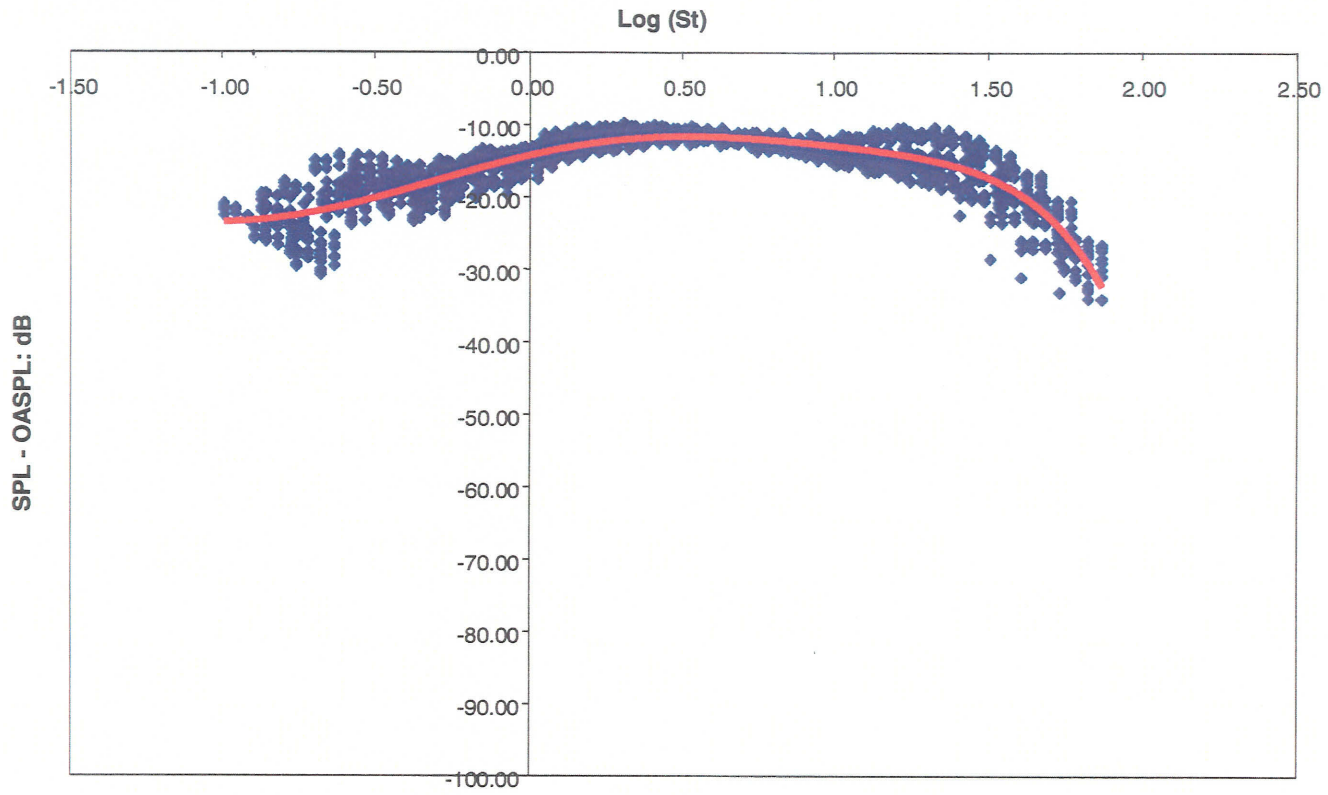

Figure 3-3: Airframe Noise, outboard flap edge : normalized spectra

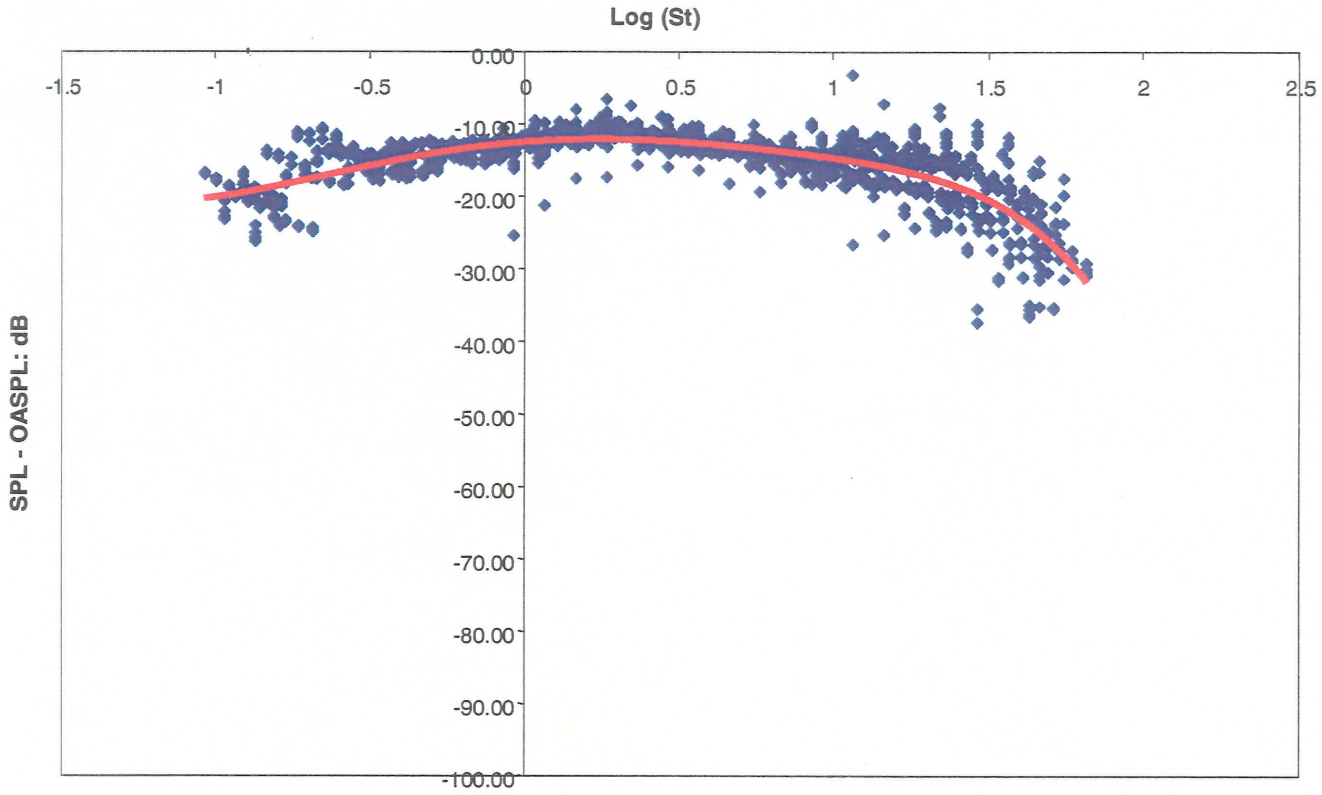

Figure 3-4 : Airframe noise, slat source : normalized spectra

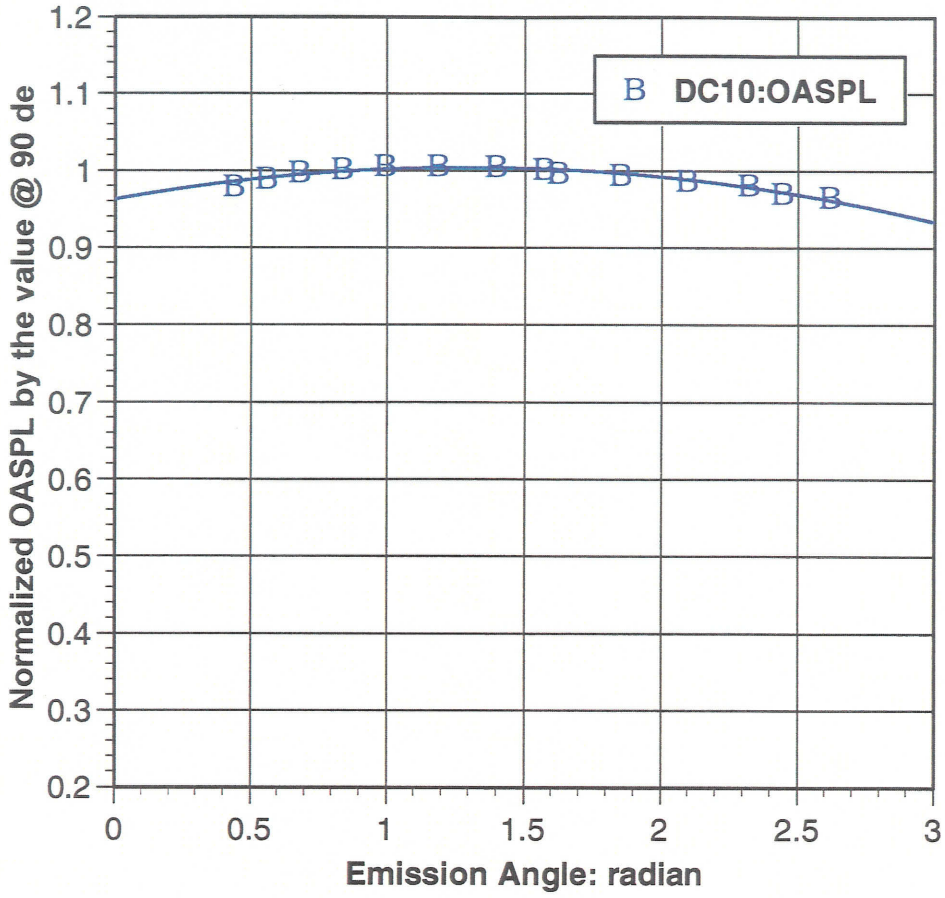

Figure 3-5 : DC-10 Scale Model OASPL Directivity

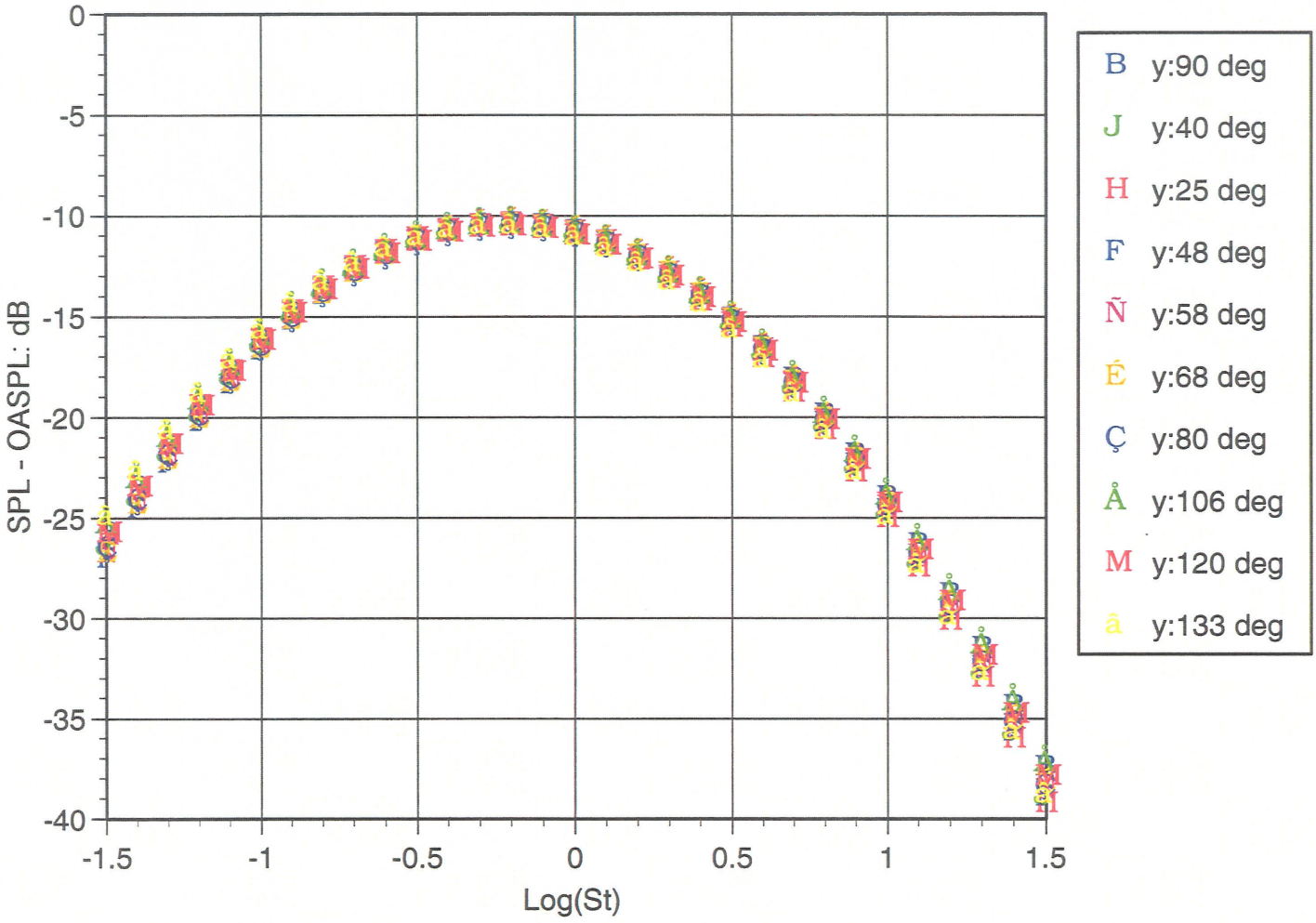

Figure 3-6 : DC-10 Scale Model Normalized Spectra At Various Emission Angles

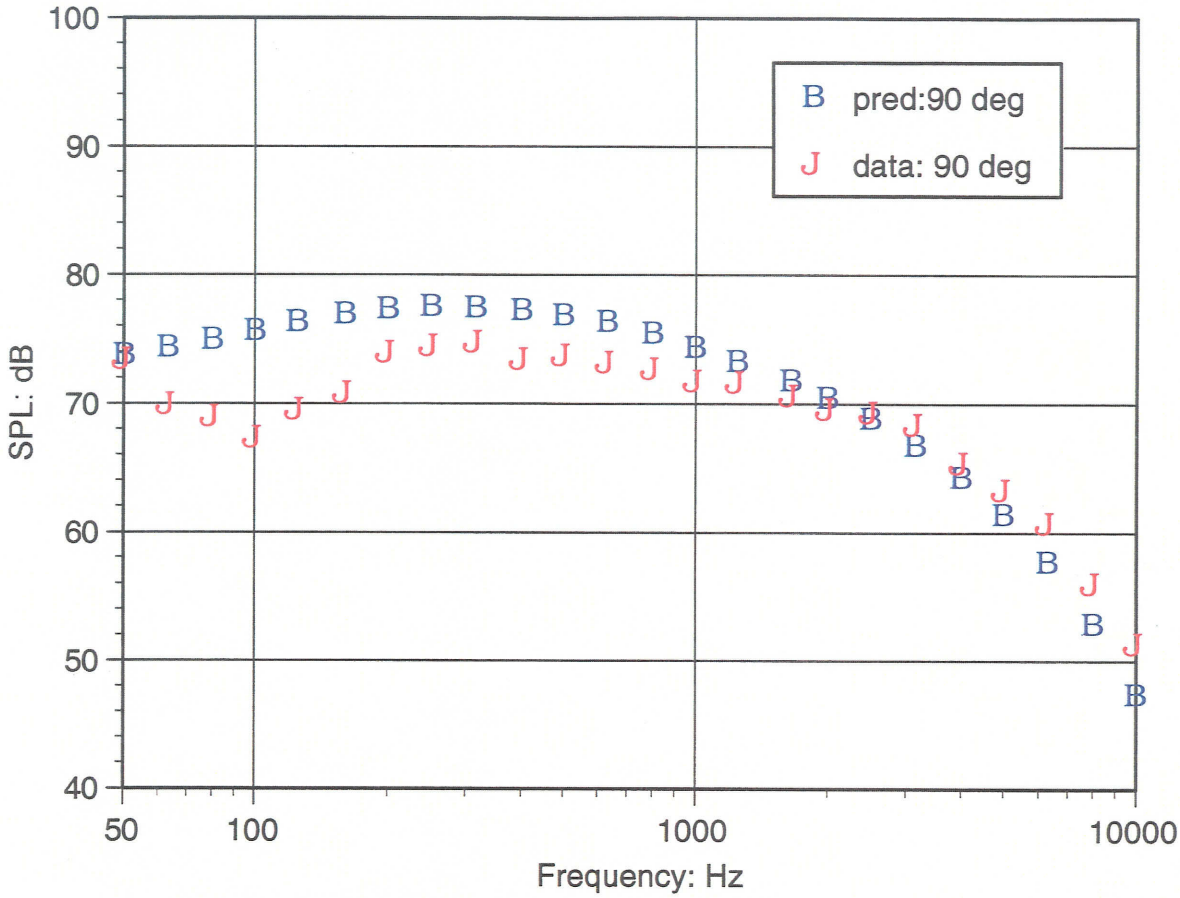

Figure 3-7 : B737 Airframe Noise: Data vs. Prediction M = 0.238, Flap Angle = 40°, Gear Down Overhead Location of 394 ft

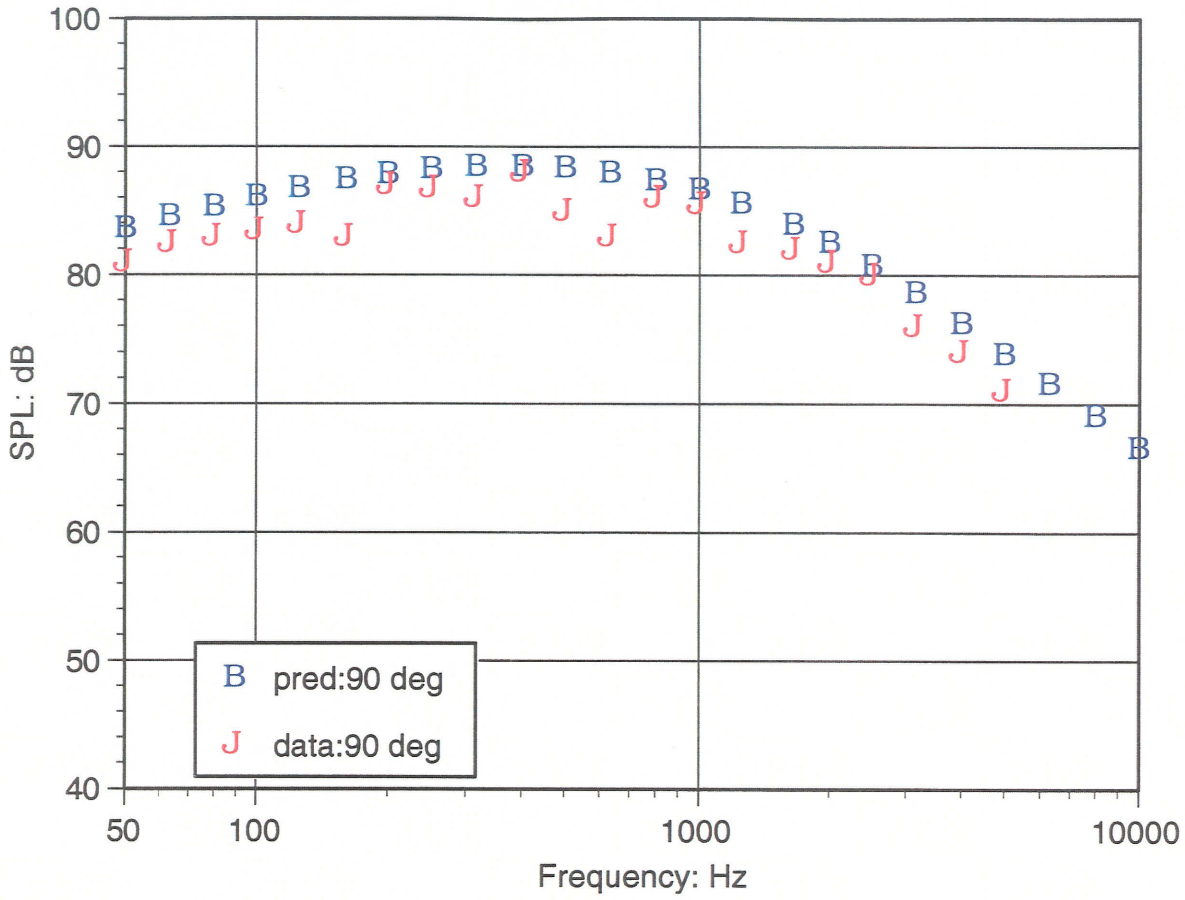

Figure 3-8 : DC-10 Airframe Noise: Data vs. Prediction M = 0.26, Flap Angle = 50°, Gear Down Overhead Location of 394 ft

4 Landing Gear Noise

4.1 Introduction

Landing gear noise has been regarded as a minor player in the airframe noise generation, probably due to the misconception that landing gear noise is significant only in the low frequency region. The Fink model (Ref.1), most widely quoted airframe noise prediction code considers gear strut and tire as noise source when landing gear noise is addressed.

The length scale for strut or tire is generally large and the aircraft speed at typical approach conditions is small. This gives a low peak frequency for landing gear noise. A recent flight test with B777 has indicated, however, that landing gear noise is a significant contributor to the total airframe noise. This result may indicate that the actual spectrum of the landing gear noise does not roll off as faster as Fink code predicts but rather rolls off more slowly yielding high PNL values. It may also indicate that much smaller length scales are involved in the landing gear noise generation.

A full size landing gear system includes a brake assembly with various dressing items such as hydraulic pipes, electric wires, holes and bolts in addition to strut, torque links and tires. It is reasonable to think that these dressings may be relevant to the high frequency noise generation. Motivated with this idea, a full-scale landing gear with all dressings was tested in the LSAF chamber (Ref.2).

4.2 Test Outline

A full-scale B737-400 landing gear was tested in the Low Speed Aeroacoustic Facility (LSAF). The objective of the test was to evaluate noise from a full-scale landing gear with particular emphasis on the examination of effects of geometry details on the far-field noise gear noise spectrum. The landing gear was tested in two configurations, fully dressed (dirty) configuration and clean configuration which lacks the brake assembly and other dressing items such as hydraulic hoses or electric wires. The test was run over a range of wind tunnel Mach number (0.18 – 0.24) and two sets of acoustic data were acquired, free-field microphone data and phased array microphone data covering the emission angle range of 65° to 150°.

4.3 Data Base

In the prediction code development process of the present study, three sets of data were used, free-field microphone data, phased array microphone data and flow field CFD data. The normalized one-third-octave spectra, one of the key elements in the prediction model were developed exclusively using the free-field microphone data. To identify the source location of landing gear noise component the phased array data were used. (Analysis of the phased array data was not performed in the present study. The results reported in Ref.2 were utilized.) The PAN AIR Technology code (A502) was used to define the flow-field in the vicinity of B737-400 main landing gear assembly. The CFD results were then used to determine the flow velocities near the landing gear noise sources.

Table 4-1 shows the LSAF landing gear noise test matrix. The free-field microphone data of these runs were extensively analyzed. Before analysis, the data were corrected for the tunnel shear layer effects using a standard method (Ref.3).

4.4 Development of Prediction Method

In this section a detailed discussion on the landing gear noise component separation, prediction methodology, data normalization and comparison with the data and existing prediction code is presented.

4.4.1 Component Separation

A detailed analysis of the free-field microphone and phased array microphone data has indicated that the main landing gear noise can be broken down into four major noise components, low frequency, mid frequency, high frequency and tire noise components as schematically illustrated in Figure 4-1. In what follows, the term "dirty" indicates presence of dressing items such as electrical wires or hydraulic hoses associated with the brake assembly while "clean" means lack of these items. Before developing normalized one-third-octave spectra, component noise breakdown was performed.

Separation of component spectra was performed as follows:

- Low frequency component: The data of clean configurations (Runs 45-48, and Runs 84-87) are considered to consist of only low frequency component. It was identified that there is no difference in spectrum between no wheel configuration (Runs 45-48) and small-wheel configuration (Runs 84-87).

- High frequency component: The spectra of clean configuration with large wheels (Runs 70-73) were compared with the spectra of dirty configuration with large wheel (Runs 106-109), and the former was subtracted from the latter, giving high and mid-frequency components as remainder. Similar comparison was made with the spectra from Runs 19-22 and Runs 57-60. Then, a quadratic curve-fitting was applied to the mid-frequency hump (see Figure 4-2) to remove this hump. The remainder, then, gives high frequency component.
- Mid-frequency component: A detailed spectral analysis indicated that the hump observed near 800 Hz for the most of the data can be curve-fitted with a quadratic equation with reasonable accuracy.
- Tire noise component: The spectra of dirty configuration with 2-small wheels (Runs 33-36) were compared with the similarly dirty configuration but with 6- large wheels (Runs 131-134), and the former was subtracted from the latter, giving tire noise spectra representing difference between 6-wheel tires and 2- wheel tires. However, as discussed in a), since practically no difference is observed between no wheel data and small wheel data, the difference between Runs 33-36 and Runs 131-134 can be regarded as the difference between no wheel data and 6-wheel data.

4.4.2 Prediction Methodology

First, overall sound pressure level (OASPL) was defined as a function of several parameters associated with landing gear noise generation.

$$OASPL = f\,(M, D/R, \theta, N_s, N_t),$$

where M = local flow Mach number, D/R = ratio of source length scale to source to monitor distance, θ = polar emission angle, N_s = number of strut and N_t = number of tire, respectively. A detailed analysis indicated that OASPL of total landing gear noise is proportional to the flow Mach number raised to the 6^{th} power.

Then, OASPL(θ) at the emission angle of θ and for the source-to-monitor distance of R is given by

$$OASPL(\theta) = \text{constant} + 60\cdot LOG\,(M) + 20\cdot LOG(D\cdot Sin(\theta)/R) + 10\cdot LOG(N_s\cdot N_t) \text{--- (A1)}$$

The constant term in Eq.A1 can be determined from the normalized OASPL. One-third-octave spectrum then can be normalized using OASPL(θ) in terms of Strouhal number as

$$SPL(f,\theta) - OASPL(\theta) = \Delta SPL(\text{Strouhal number},\theta) \quad \text{-------- (A2),}$$

$$\text{Strouhal number} = (f \cdot D) / V \quad \text{-------- (A3)}$$

where f is the one-third-octave band center frequency and V is the local flow velocity.

Equations (A1) to (A3) should be applied to each landing gear noise component using appropriate length scale.

4.4.3 Data Normalization

According to Ref.2, the cutoff frequency of the anechoic chamber of LSAF is 200 Hz. In the present data analysis, lower frequencies below 200 Hz were discarded when OASPL was determined. However, in the prediction code developed under this task, these low frequencies are recovered by extrapolation.

4.4.3.1 One-Third-Octave Spectrum

Normalization of spectrum was performed according to the following steps:

1. Determine the length scale
2. Determine the local flow velocity
3. Calculate OASPL with spectrum (SPL) over the frequency range of 200 to10,000 Hz.
4. Calculate LOG(Strouhal no.) according to Eq. A3
5. Plot (SPL-OASPL) versus LOG(Strouhal no.)

These steps were applied to all noise components. The resulted normalized spectra are shown from Figure 4-2 to Figure 4-13. The normalized spectra for low frequency component are shown from Figure 4-2 to Figure 4-4. In what follows, unless otherwise stated, the data shown are from 2-wheel configuration. (see Table 4-1) The length scale was set equal to the strut diameter of B737-400. The local flow Mach number was set equal to approximately 83 % of the nominal tunnel flow Mach number based on the CFD result (see Figure 4-18).

The emission angles shown in the label in these figures are the free-field microphone angles, being slightly different from true emission angles due to the presence of tunnel shear layer. (The emission angle (θ) defined in the code is the true emission angle.) The data from Runs 45 to 48 (clean, small tires) and Runs 84 to 87 (clean, large tires) were used in these figures. These figures also include a curve-fitting using the 3rd order polynomial equation.

The sequence Figure 4-5 to Figure 4-7 shows the normalized spectra for high frequency component . The data used for these figures are the spectra determined as the difference between spectrum for dirty configuration and one for clean configuration. The data from Runs 106 to 109 (dirty, large tires) include high frequency noise due to the dressing associated with brake system, while the data from Runs 70 to 73 (clean, large tires) do not. The length scale for high frequency noise was set equal to the typical diameter of electric wire near the brake assembly. A curve-fitting by the 3rd order polynomial equation is also included in these figures.

The sequence from Figure 4-8 to Figure 4-10 shows the normalized spectra for mid-frequencies observed near 800 Hz as a prominent hump. According to Ref.1, the author attributes this hump to the hydraulic pipes near the brake assembly. However, even clean configuration shows a similar hump near this frequency, although the amplitude is much smaller. At this point, the noise source for this mid-frequency hump has not been identified. Tentatively, the length scale for this noise component was set equal to the mean value of the length scales for low and high frequencies. Compared to low or high frequency counterpart, this noise component is not well collapsed. The data used for these figures are from Runs 131 to 134 (dirty, 6-wheels, large tires).

The normalized tire noise component spectra are shown in Figure 4-11- Figure 4-13. The data from Runs 131 to 134 (dirty, 6-wheels, large tires) and Runs 19 to 22 (dirty, 2-wheels, large tires) were used for this normalization. The length scale is the tire diameter. The choice of data for these figures is based on the notion that the 2-wheel configuration should be the baseline in practical applications. Again, the collapse of data is not so good as low or high frequency counterpart. In view of significant scattering of data for tire noise component, it is assumed that the tire noise component does not have directional preference and can be represented by a third-order polynomial equation (from a curve-fitting) shown in Figure 4-12.

4.4.3.2 OASPL

The normalization of OASPL was performed assuming that each noise component follows the 6th-power law for noise dependency on the local flow velocity. Figure 4-14 - Figure 4-17 show the normalized OASPL defined based on Eq. A1. Figure 4-14 which shows the normalized OASPL directivity for the low frequency component determined with the data from Runs 57 to 73 (see Table 4-1) of clean, large tire configuration. The data were extrapolated beyond approximately 145° based on the general trend observed in flight test data. Similar normalized OASPL directivities for other noise components are shown in Figure 4-15 - Figure

4-17. The constant of Eq.A1 was calculated by a polynomial equation determined by applying curve-fitting to the data of these figures.

4.4.4 Calculation Method

Landing gear noise is calculated as follows:

Step 1: Calculate lossless, de-Dopplerized OASPL(θ) for low, high, mid-frequency components and tire noise

a) Low frequency component

$$OASPL1(\theta) = DELTA1 + 60\cdot\log(V/C_0) + 20\cdot\log(DL\cdot\sin\theta/R) + 10\cdot Log(N_s\cdot N_t) \quad \text{----------(1)}$$

$$DELTA1 = A(1)\cdot EXP(A(2)\cdot ANG(\theta)) \quad \text{---------} \quad (2)$$

$A(1) = 1.641991E+2, \quad A(2) = 4.48107E-4$

b) High frequency component

$$OASPL2(\theta) = DELTA2 + 60\cdot\log(V/C_0) + 20\cdot\log(DH\cdot\sin\theta/R) + 10\cdot Log(N_s\cdot N_t) \quad \text{---------- (3)}$$

For $ANG(\theta) \leq 140°$ $\quad DELTA2 = 180.0$

For $ANG(\theta) > 140°$

$$DELTA2 = C(1) + C(2)\cdot ANG(\theta) + C(3)\cdot(ANG(\theta))^2 + C(4)\cdot(ANG(\theta))^3$$

$C(1) = 2.220403E+2, C(2) = -1.328178, C(3) = 1.325498E-2, C(4) = -4.2385E-5$

c) Mid-frequency component

$$OASPL3(\theta) = DELTA3 + 60\cdot\log(V/C_0) + 20\cdot\log(DMID\cdot\sin\theta/R)$$

$$+ 10 \cdot LOG(N_s \cdot N_t) \qquad \text{---------- (4)}$$

$$DELTA3 = B(1) + B(2) \cdot ANG(\theta) + B(3) \cdot (ANG(\theta))^2 \qquad \text{---------- -- (5)}$$

$$B(1) = 1.933593E+2,\ B(2) = -3.55895E-1,\ B(3) = 1.795617E-3$$

d) Tire noise component

$$OASPL4(\theta) = 162 + 60 \cdot \log(V/C_0) + 20 \cdot \log(DTIRE \cdot \sin\theta/R) + 10 \cdot LOG(N_s \cdot N_t) \qquad \text{---------- (6)}$$

Step 2: Calculate Strouhal number defined as

$$\text{Strouhal number} = St = \log\left(\frac{D_x \cdot f}{V}\right) \qquad \text{---------- (7)}$$

x = L for low freq., x = H for high freq., x = MID for mid-freq., x = TIRE for tire noise

Step 3: Calculate one-third-octave SPL with the following equations

a) Low frequency component

$$SPL(\theta,f) = OASPL1(\theta) + \Delta_1 \qquad \text{---------- (8)}$$

$$\Delta_1 = P(1,j) + P(2,j) \cdot St + P(3,j) \cdot St^2 + P(4,j) \cdot St^3 \qquad \text{--------- (9)}$$

j is the emission angle index and defined as

$$\begin{aligned} j &= 1 && \text{for} \quad \theta \le 60^\circ \\ &= (\theta/10) - 5 && \text{for} \quad 60^\circ < \theta \le 120^\circ \\ &= 7 && \text{for} \quad \theta = 130^\circ \\ &= 8 && \text{for} \quad \theta = 140^\circ \text{ and } \theta = 150^\circ \end{aligned} \qquad \text{---------- (10)}$$

The coefficients P(i,k) are given in Table 4-2.

b) High frequency component

$$SPL(\theta,f) = OASPL2(\theta) + \Delta_2 \quad \text{---------- (11)}$$

$$\Delta_2 = Q(1,j) + Q(2,j)\cdot St + Q(3,j)\cdot St^2 + Q(4,j)\cdot St^3 \quad \text{---------- (12)}$$

The emission angle index j are the same as for a).

The coefficients Q(i,k) are given in Table 4-3.

c) Mid-frequency component

$$SPL(\theta,f) = OASPL3(\theta) + \Delta_3 \quad \text{---------- (13)}$$

$$\Delta_3 = S(1,j) + S(2,j)\cdot St + S(3,j)\cdot St^2 \quad \text{---------- (14)}$$

The emission angle index j are the same as for a).

The coefficients S(i,k) are given in Table 4-4

d) Tire noise component

$$SPL(\theta,f) = OASPL4(\theta) + \Delta_4 \quad \text{---------- (15)}$$

$$\Delta_4 = X(1) + X(2)\cdot St + X(3)\cdot St^2 + X(4)\cdot St^3 + X(5)\cdot St^4 + X(6)\cdot St^5 + X(7)\cdot St^6 + X(8)\cdot St^7 \quad \text{-- (16)}$$

The coefficients X(i) are given in Table 4-5.

4.4.5 Aerodynamic Data

As mentioned above, the local flow velocity in the vicinity of landing gear noise source(s) was determined using the PAN AIR Technology code (A502). Figure 4-18 shows a vertical distribution of local flow velocity under the wing. The code was applied to B737-400 configuration with flap angle = 30° and pitch angle = 4°. The abscissa is the vertical distance

from the bottom surface of wing and the ordinate is the local velocity ratio relative to the free-stream (undisturbed) velocity. In the present study, the local flow velocity at source(s) was assumed to be 83% of the free-stream velocity. (This is the velocity approximately at the mid-point of the main gear strut length exposed to flow.)

4.4.6 Comparison with Data

A landing gear noise prediction code was developed based on the algorithm discussed in Section 2.4. The code tentatively designated LGN4X was written in FORTRAN 77.

The prediction code was tested against the B737 data of selected runs. The sequence Figure 4-19 to Figure 4-30 shows the results of the comparison. The selected runs in the figures are Run 22 (dirty, 2-wheel, large tire, M = 0.24), Run 132 (dirty, 6-wheel, large tire, M = 0.20), Run 133 (dirty, 6-wheel, large tire, M = 0.22) and Run 134 (dirty, 6-wheel, large tire, M = 0.24). The comparison was made at three selected emission angles, 60°, 90° and 140° (nominal). The comparison is made for the frequency range of 200 to 10,000 Hz considering the cutoff frequency (200 Hz) of the LSAF anechoic chamber. It appears that agreement of prediction with the data is very good for high frequencies. Some discrepancy is observed for low to mid-frequencies. Poor collapse of spectra for both tire and mid-frequency components (Figure 4-8 and Figure 4-13) certainly causes the discrepancy. Generally, prediction better matches the data of 6-wheel configuration at high Mach numbers. It is reasonable to assume that the signal-to-noise ratio becomes better for higher Mach number and with a larger model, yielding better quality data.

4.4.7 Comparison with Fink's Code

A limited comparison of the present code with Fink's airframe noise prediction code (MCP version) was performed. As input to the present code, three length scales were chosen for low, high and mid- frequency components; the strut diameter, typical hydraulic pipe diameter and the mean of the sum of strut diameter and hydraulic diameter, respectively. The tire diameter is an obvious choice for tire noise component. The local flow Mach was determined as 83% of the nominal tunnel Mach number based on the panel code output described in Section 2.3.

Spectral comparison is made in Figure 4-31 to Figure 4-33. As noted, Fink's code shows a faster roll-off in the high frequency region. Fink's model does not explicitly address high frequency noise. Although, the database Fink used for the development of his model included flight test data, the data used to develop landing gear noise component were from scale models that lack the dressings associated with the brake assembly. Since these dressings are mainly

responsible for high frequency noise generation, any landing gear noise prediction model that was developed based on scale models is likely to underestimate high frequency noise. Because of the underestimation for high frequencies, large discrepancy could yield as illustrated in Figure 4-34 when these prediction codes are compared in terms of EPNL.

4.5 Conclusions and Recommendations

Free field acoustic data from the LSAF landing gear noise test with a B737-400 full size landing gear assembly was thoroughly analyzed. Based on the normalized 1/3 octave spectra determined in the analysis a new landing gear noise prediction code was developed with the supplemental information from the phased array microphone data and the panel code output. Though the code was developed based on a limited database, it appears to capture the major characteristics of landing gear noise. The code has several features. It explicitly addresses mid- and high frequency components in addition to low frequency and tire noise components. A preliminary comparison with the Fink code (landing gear noise only) showed that one-third-octave spectrum predicted by the Fink code rolls off much faster than the present code at any emission angle. This subsequently results in a significant underestimate of landing gear noise when evaluated in terms of EPNL. As mentioned above, the present code was developed based on a limited database, further validation of the code is certainly desirable whenever new data becomes available.

4.6 References for this chapter :

1. Fink, M. R., "Airframe Noise Prediction Method," FAA-RD-77-29, 1997
2. Stoker, R. W., "Landing Gear Noise Test Report," Contract NAS1-97040, 1997
3. Amiet, R. K., "Refraction of Sound by a Shear Layer," J. Sound and Vib. 58(4), 1978

4.7 Symbols used in this chapter

A(i)	Coefficients for an exponential equation
B(i), P(i,j), Q(i,j), S(i,j), X(i)	Coefficients for polynomial equations
C_0	Local speed of sound, ft/s
DELTA1, DELTA2	Constants for OASPL, dB
DL	Representative length scale for low frequency noise component, ft
DH	Representative length scale for high frequency noise component, ft
DMID	Representative length scale for mid-frequency noise component, ft
DTIRE	Representative length scale for tire noise component, ft
D_x	Representative length scale for x noise component, ft
f	1/3 octave band center frequency, Hz
M	Flight Mach number
N_s	Number of struts
N_t	Number of tires
OASPL1(θ)	OASPL for low frequency component, dB
OASPL2(θ)	OASPL for high frequency component, dB
OASPL3(θ)	OASPL for mid-frequency component, dB
OASPL4(θ)	OASPL for tire noise component, dB
R	Source to monitor distance, ft
St	Logarithmic Strouhal number
V	Air speed, ft/s
Δ_1	Normalized SPL for low frequency component , dB
Δ_2	Normalized SPL for high frequency component , dB
Δ_3	Normalized SPL for mid-frequency component , dB
Δ_4	Normalized SPL for tire noise component , dB
ξ, XI	Landing gear dressing complexity factor
θ, ANG(θ)	Polar emission angle, degrees

Table 4-1: LSAF Gear Noise Test Matrix (2-wheels)

Run	Mach Number	Configuration	Wheel Type	Remark
19	0.18	D	large	D= dirty
20	0.20	D	large	C = clean
21	0.22	D	large	no = no wheel
22	0.24	D	large	
33	0.18	D	small	
34	0.20	D	small	
35	0.22	D	small	
36	0.24	D	small	
45	0.18	C	small	
46	0.20	C	small	
47	0.22	C	small	
48	0.24	C	small	
57	0.18	C	large	
58	0.20	C	large	
59	0.22	C	large	
60	0.24	C	large	
70	0.18	C	large	
71	0.20	C	large	
72	0.22	C	large	
73	0.24	C	large	
84	0.18	C	no	
85	0.20	C	no	
86	0.22	C	no	
87	0.24	C	no	
106	0.18	D	large	
107	0.20	D	large	
108	0.22	D	large	
109	0.24	D	large	

LSAF Gear Noise Test Matrix (6-wheels)

131	0.18	D	large	
132	0.20	D	large	
133	0.22	D	large	
134	0.24	D	large	

Table 4-2 : Coefficients for Equation (8)

k	P(1,k)	P(2,k)	P(3,k)	P(4,k)
1	-9.877825	-7.632699	1.661801E-1	-1.444081
2	-9.675465	-6.857752	-1.117547	-1.222514
3	-9.771083	-5.604022	-2.498093	-7.675554E-1
4	-9.700787	-5.892989	-6.764243E-1	-6.764243E-1
5	-9.791076	-6.587548	-7.746056E-1	-1.553996
6	-1.001907E+1	-6.9668	2.283479	-3.257356
7	-9.975054	-6.810322	2.421265	-3.296517
8	-1.008466E+1	-9.393665	6.13125	-4.564913

Table 4-3 : Coefficients for Equation (12)

k	Q(1,k)	Q(2,k)	Q(3,k)	Q(4,k)
1	-1.025003E+1	-7.112481	-1.52365E+1	1.0224451E+1
2	-1.066351E+1	-8.831999	-1.315696E+1	9.298285
3	-1.018087E+1	-6.14302	-1.525915E+1	5.283273
4	-1.033656E+1	-1.058539E+1	-1.234325E+1	8.264513
5	-1.044686E+1	-7.7798	-1.48045E+1	5.24673
6	-1.076274E+1	-1.142915E+1	-1.585081E+1	9.143245
7	-1.076015E+1	-1.086217E+1	-1.434196E+1	9.873318
8	-1.059679E+1	-9.508286	-1.494926E+1	1.202191E+1

Table 4-4 : Coefficients for Equation (14)

k	S(1,k)	S(2,k)	S(3,k)
1	-3.379221	3.370469E+1	-2.713406E+2
2	-4.897243	2.333926E+1	-2.496018E+2
3	-5.820157	7.075035	-2.482546E+2
4	-6.295315	-6.580083	-1.907594E+2
5	-6.8834	-1.700693E+1	-1.803207E+2
6	-7.390352	3.915408E-1	-1.636399E+2
7	-5.588916	5.34791	-1.92612E+2
8	-3.84597	1.130759E+1	-2.409802E+2

Table 4-5 : Coefficients for Equation (16)

X(1)	X(2)	X(3)	X(4)
-9.992824	-7.587345	-1.474888E+1	3.307829E+1

X(5)	X(6)	X(7)	X(8)
1.141251E+2	-3.080667E+2	2.104914E+2	-4.519879E+1

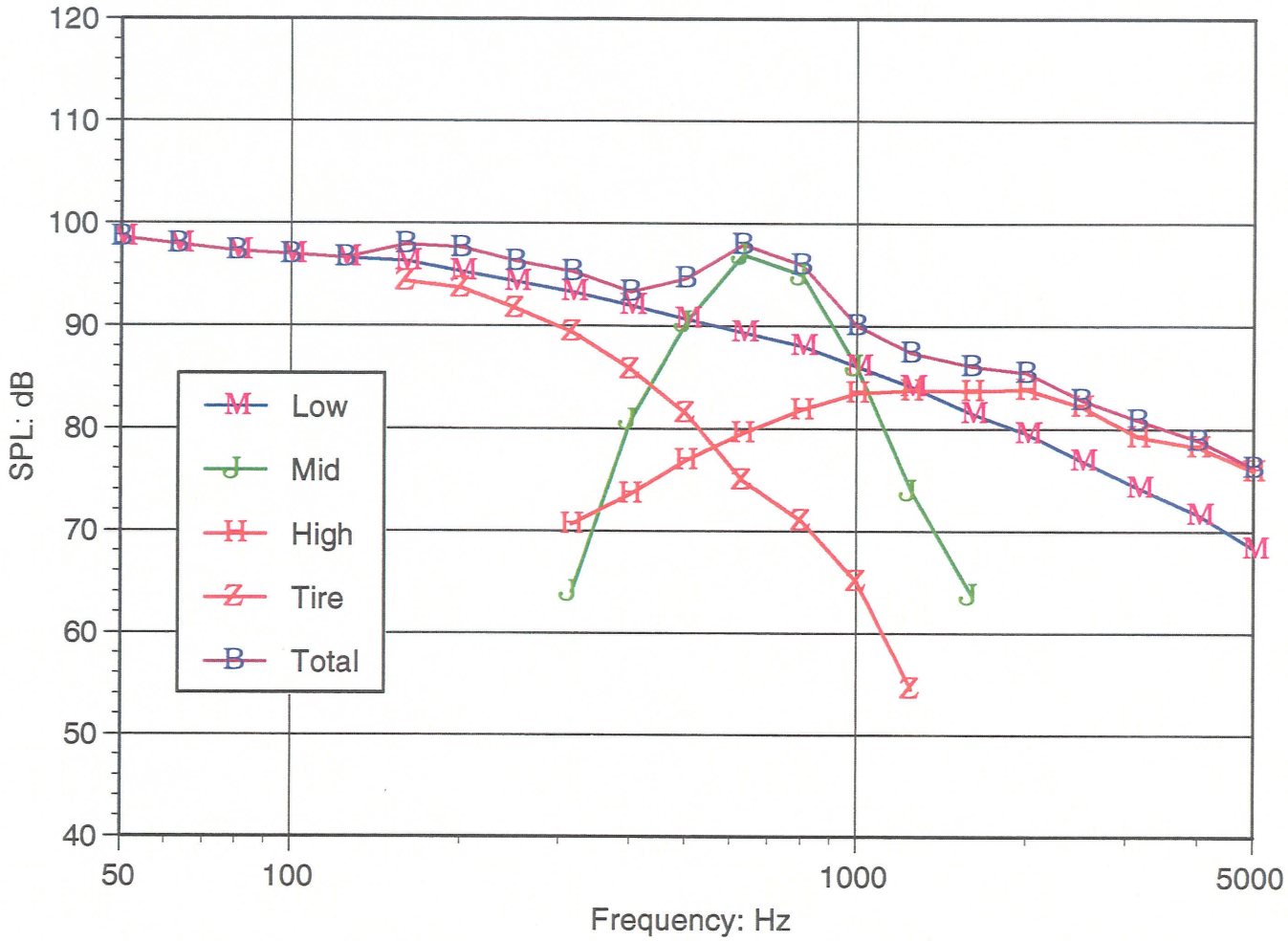

Figure 4-1 : Schematic Illustration of Source Breakdown of Landing Gear Noise

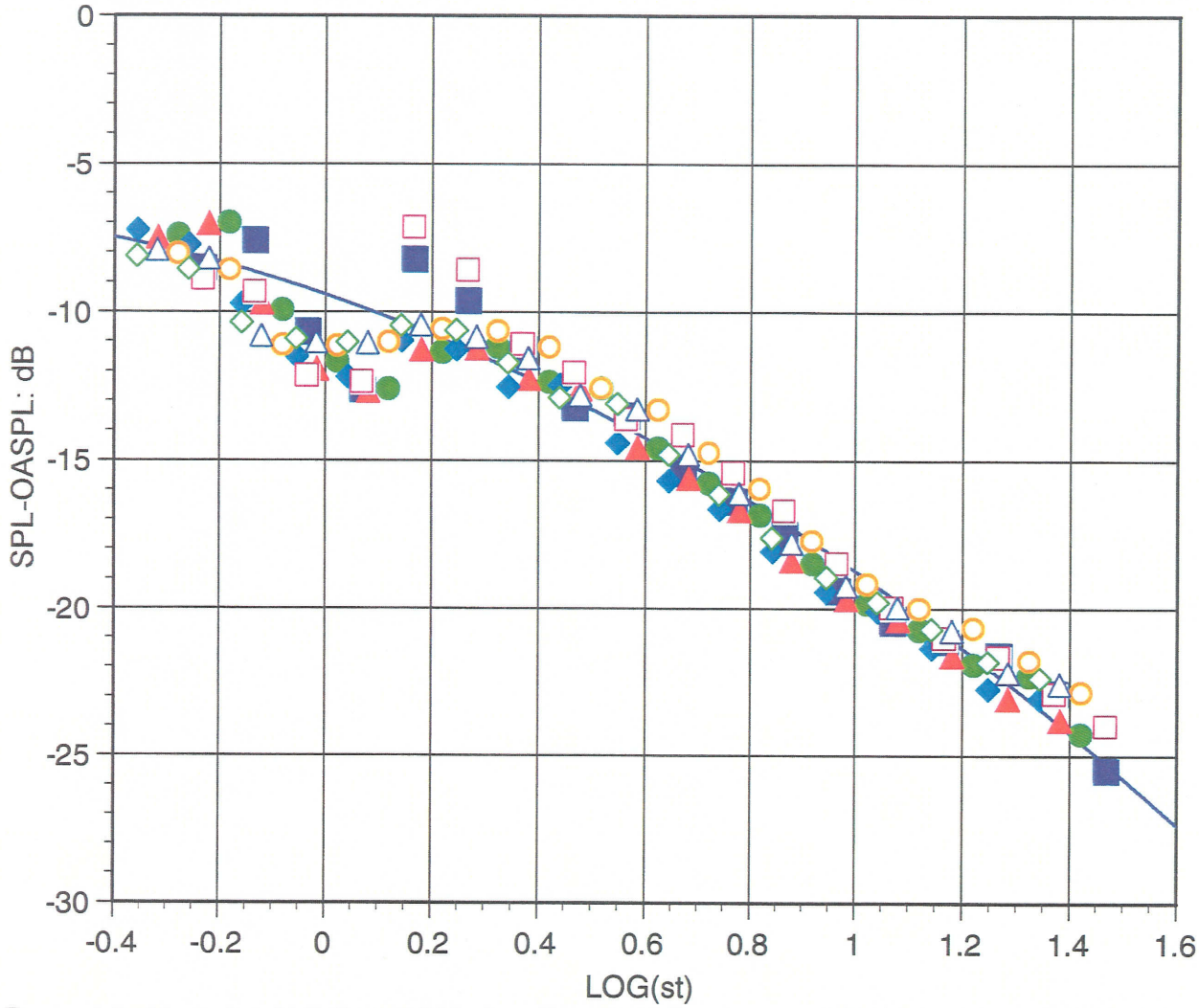

Figure 4-2 : Normalized 1/3-Octave SPL: Low Frequency Component 2-wheel, clean, no tire/small, M = 0.18, 0.2, 0.22, 0.24, θ = 60°

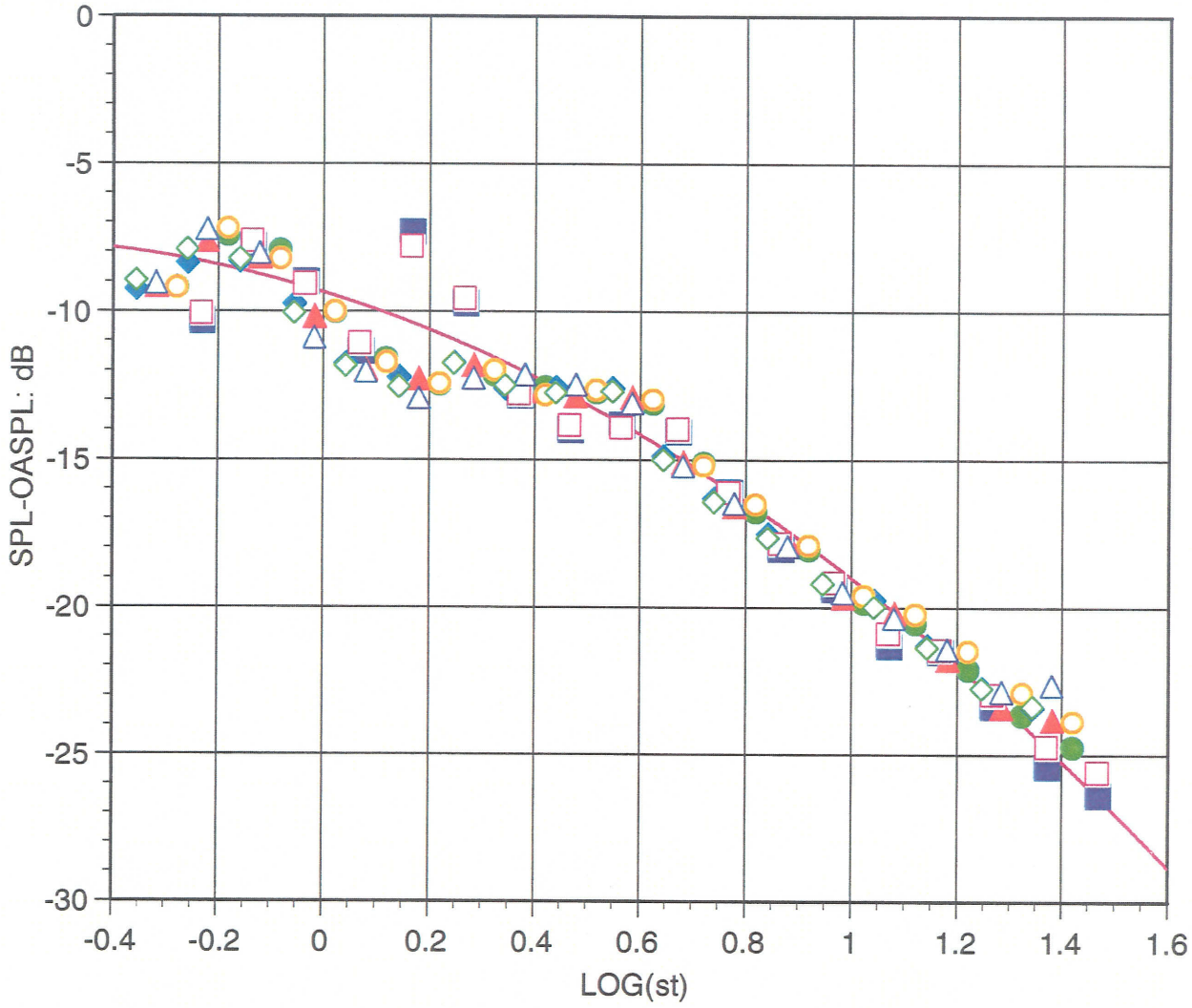

Figure 4-3 : Normalized 1/3 -Octave SPL : Low Frequency Component (2-wheel, clean, no tire/small, M = 0.18, 0.2, 0.22, 0.24, θ = 90°)

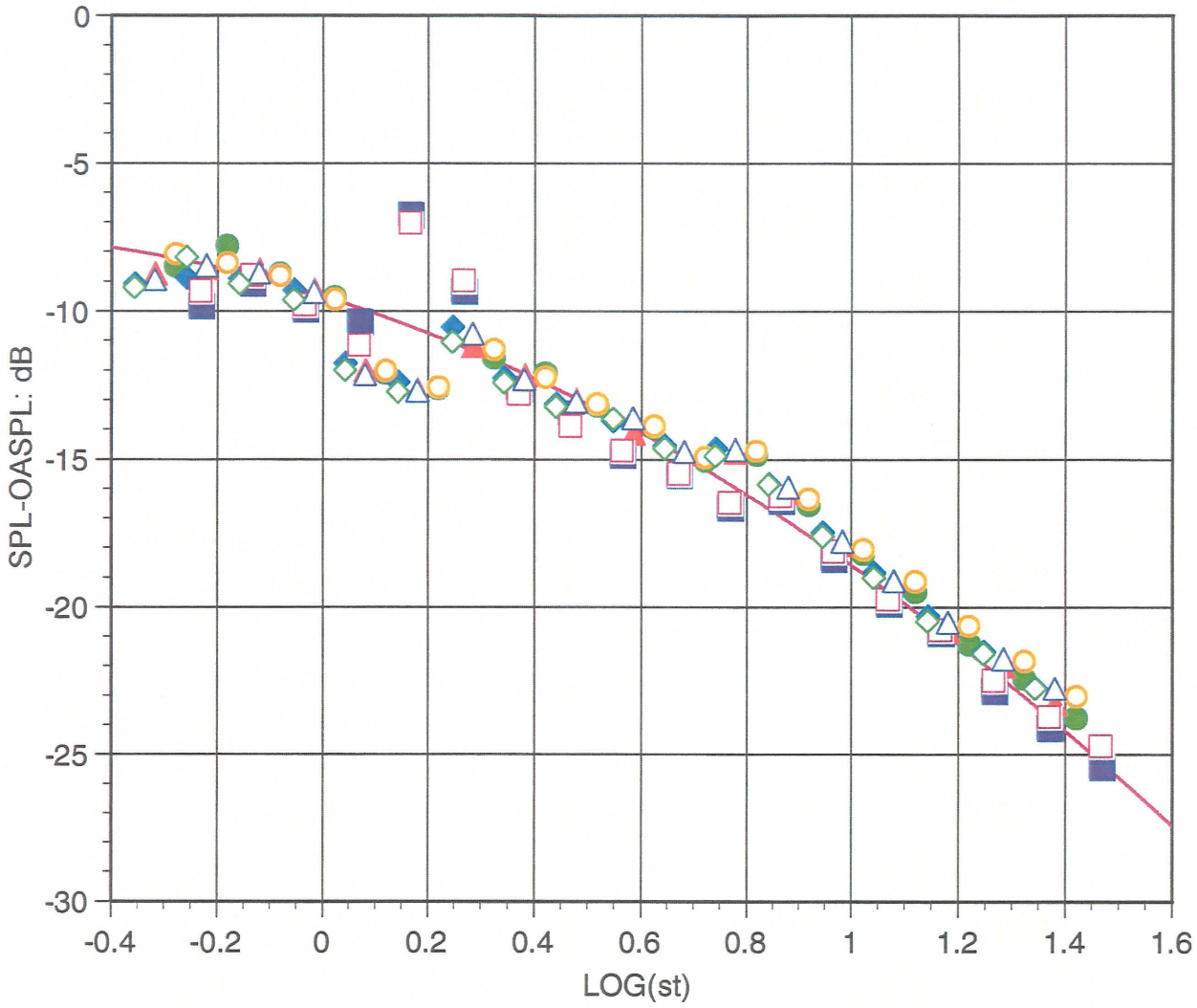

Figure 4-4 : Normalized 1/3-Octave SPL: Low Frequency Component (2-wheel, clean, no tire/small, M = 0.18, 0.2, 0.22, 0.24, θ = 120°)

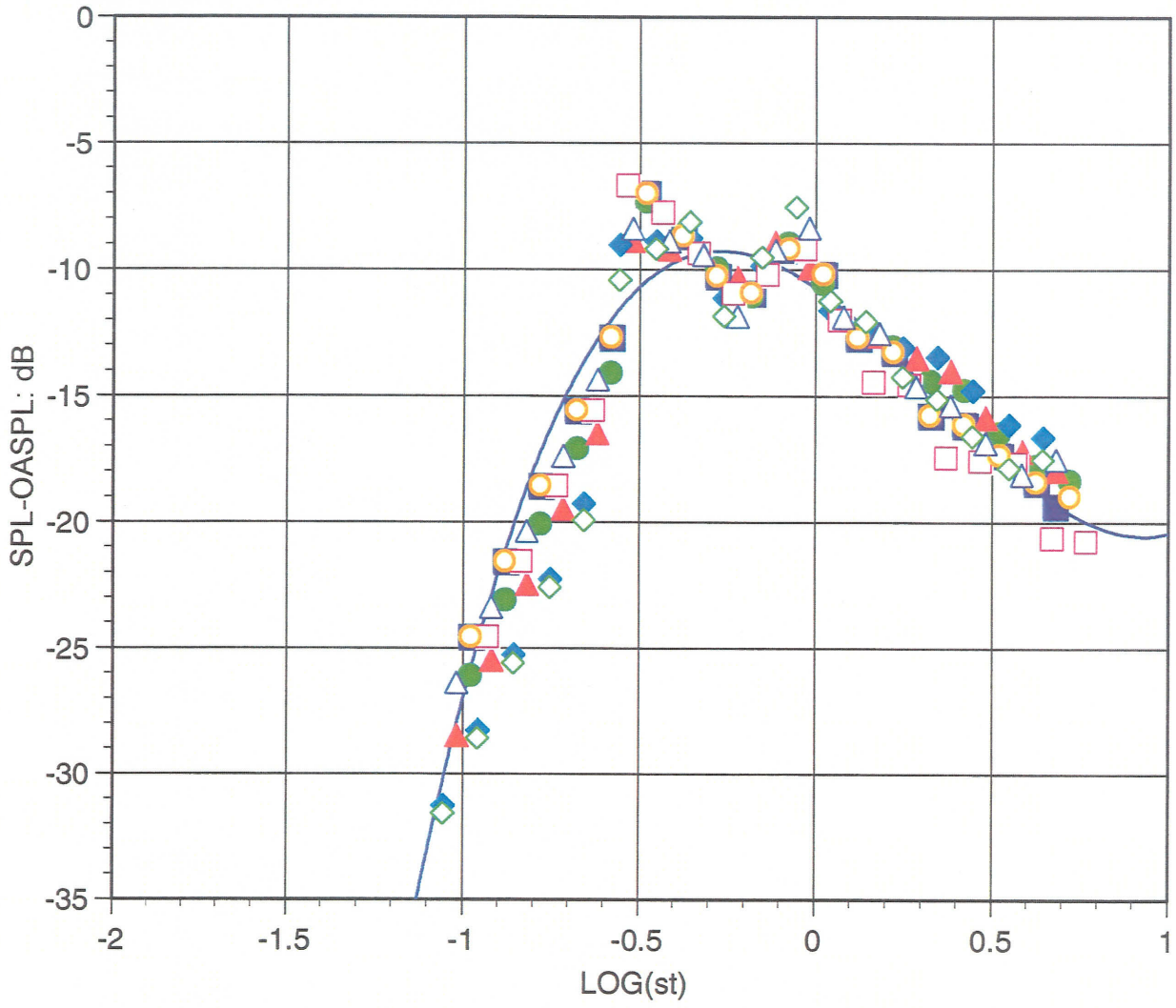

Figure 4-5 : Normalized 1/3 Octave SPL: High Frequency Component (2-wheel, clean/ dirty, large tires, M = 0.18, 0.2, 0.22, 0.24, θ = 60°)

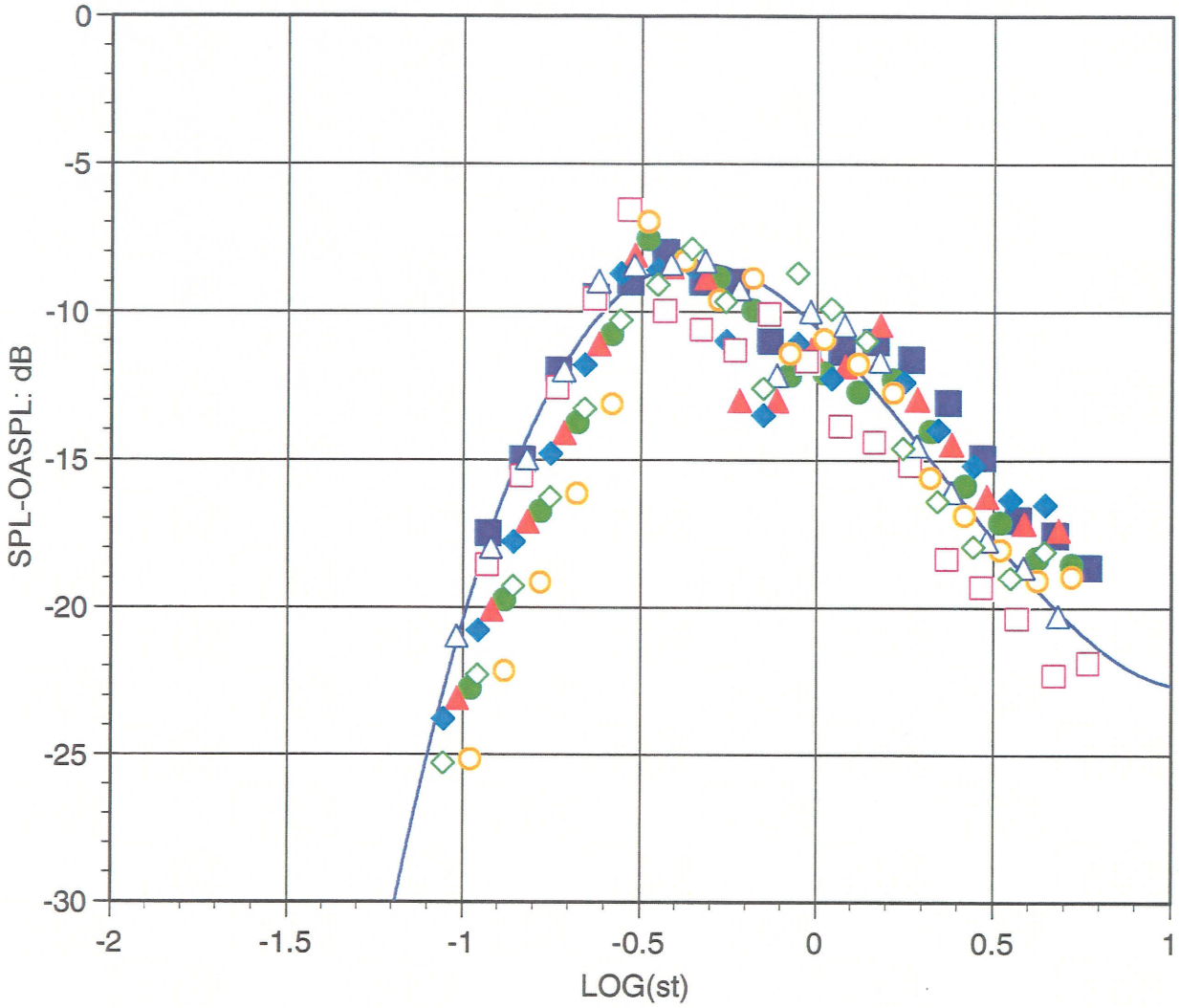

Figure 4-6 Normalized 1/3-Octave SPL: High Frequency Component : 2-wheel, clean/ dirty, large tires, M = 0.18, 0.2, 0.22, 0.24, θ = 90°

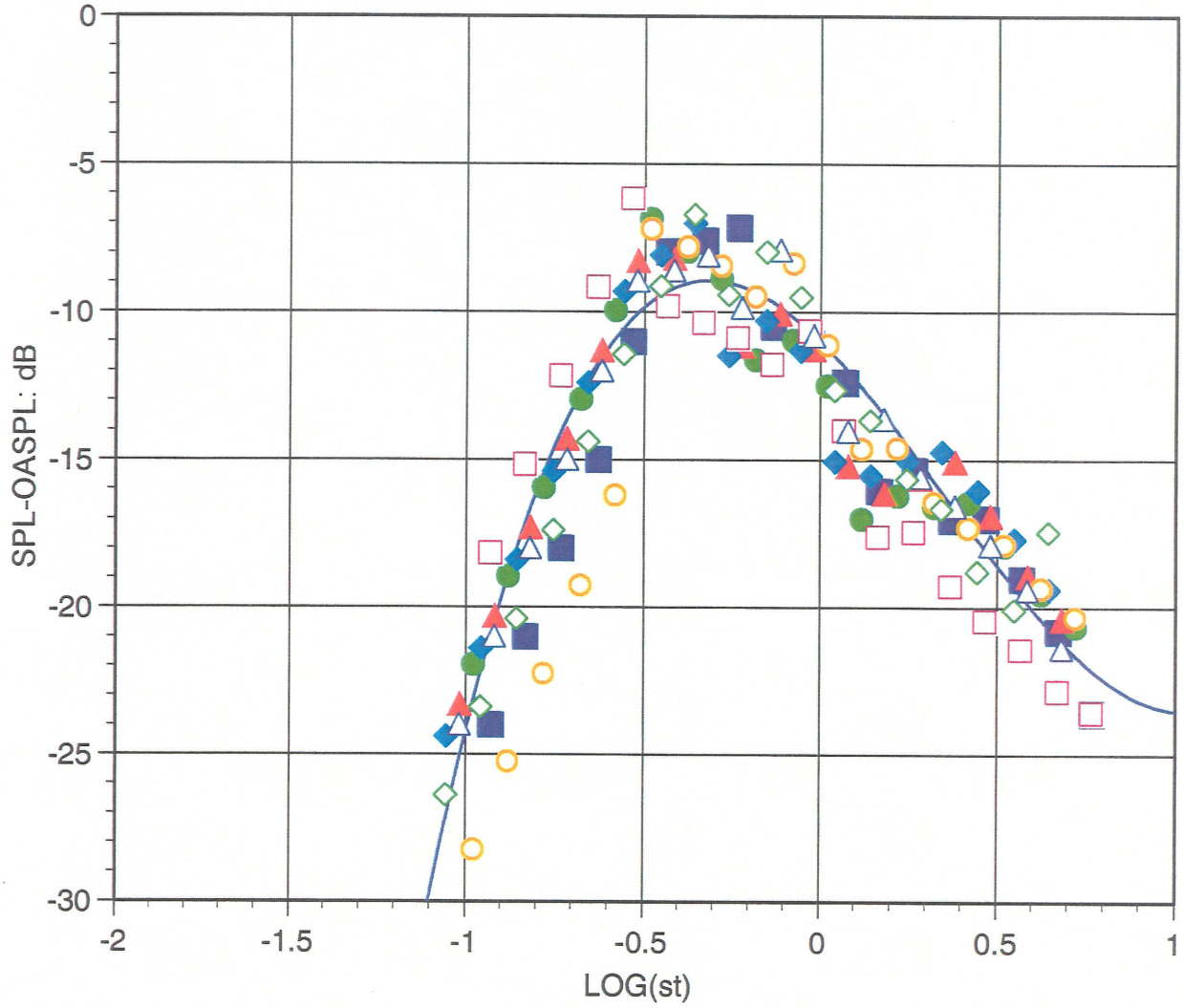

Figure 4-7 Normalized 1/3-Octave SPL: High Frequency Component : 2-wheel, clean/ dirty, large tires, M = 0.18, 0.2, 0.22, 0.24, θ = 120°

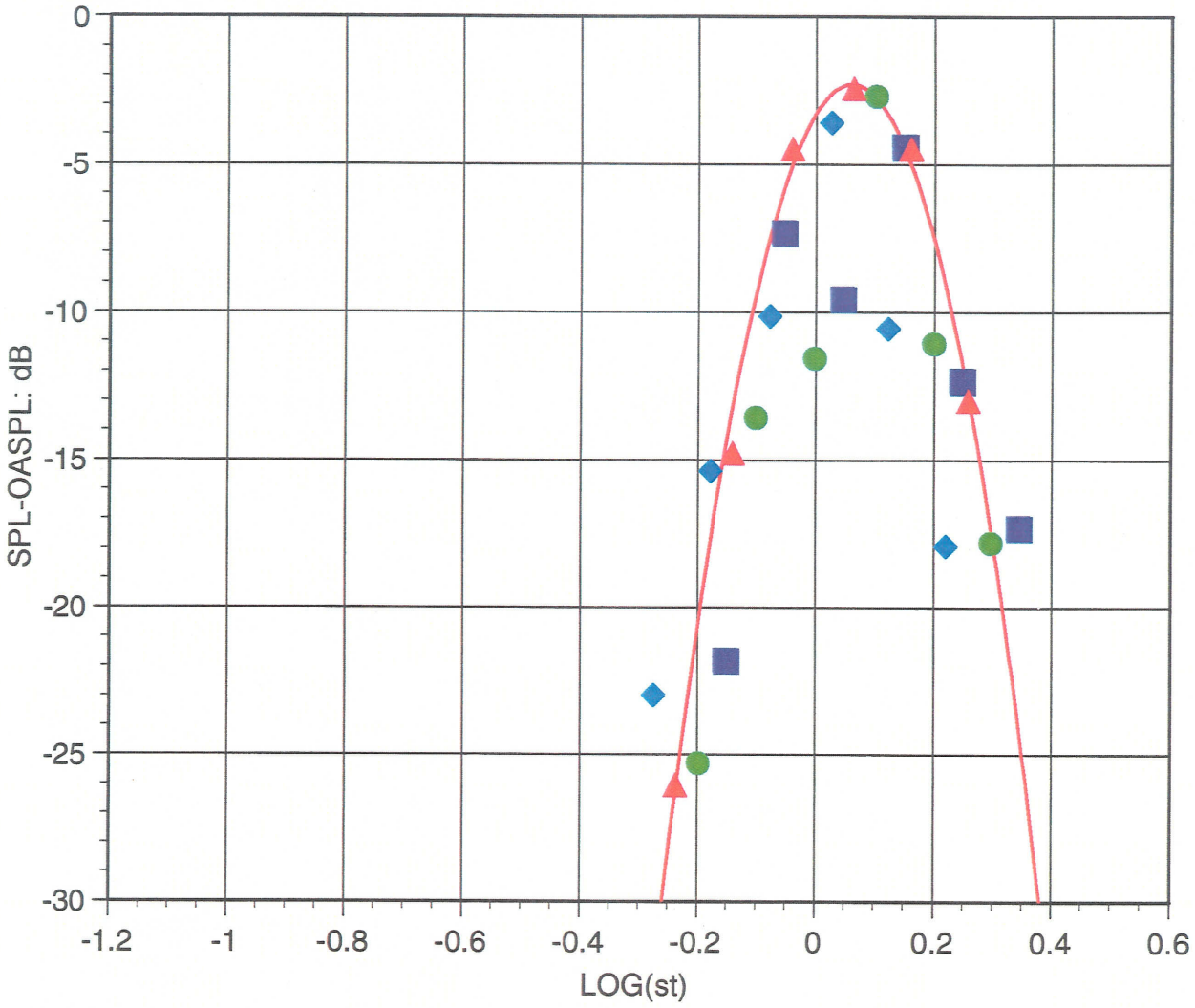

Figure 4-8 Normalized One-Third-Octave SPL: Mid - Frequency Component : 2-wheel, clean/ dirty, large tires, M = 0.18, 0.2, 0.22, 0.24, θ = 60°

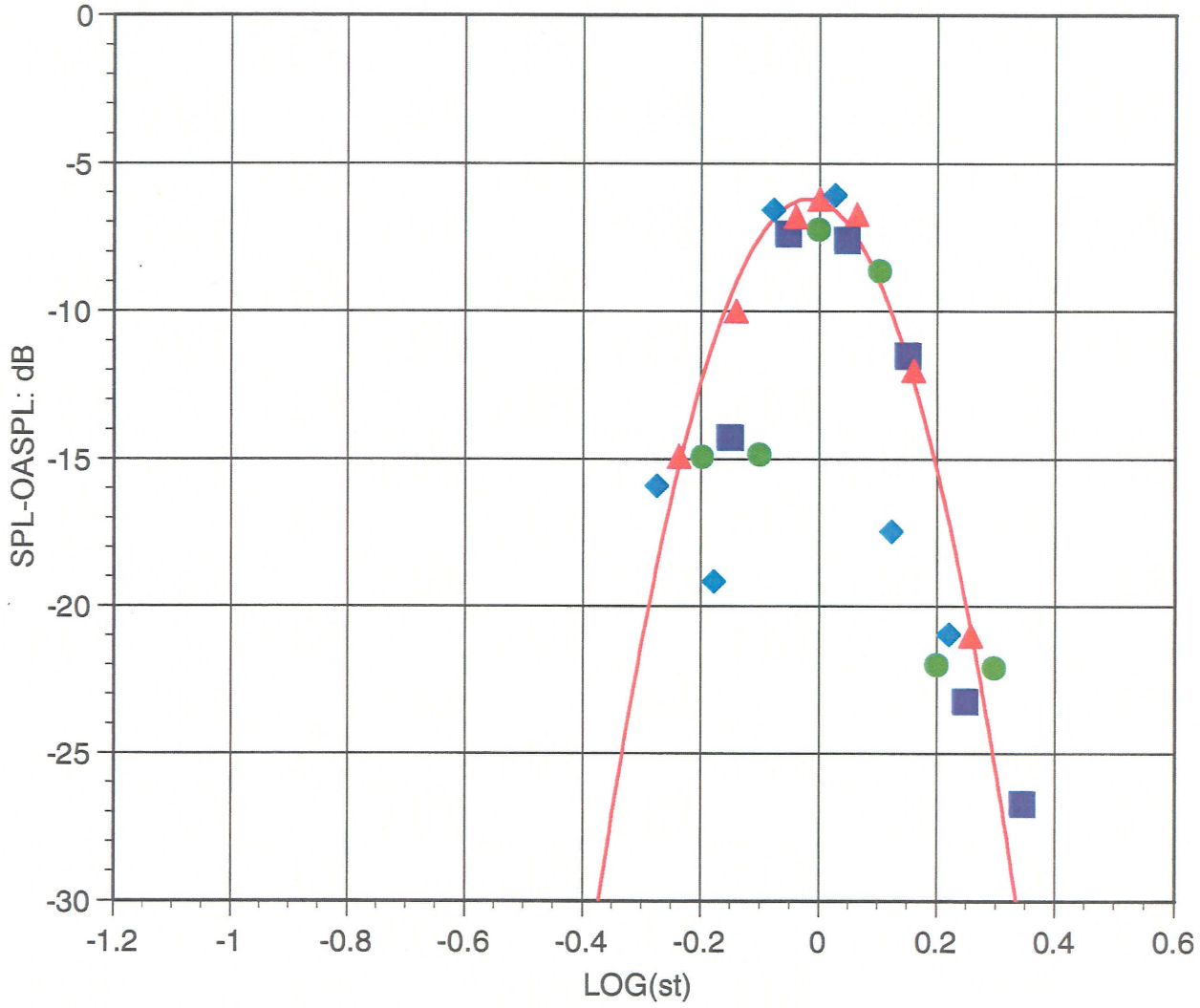

Figure 4-9 Normalized 1/3-Octave SPL: Mid - Frequency Component : 2-wheel, clean/ dirty, large tires, M = 0.18, 0.2, 0.22, 0.24, θ = 90°

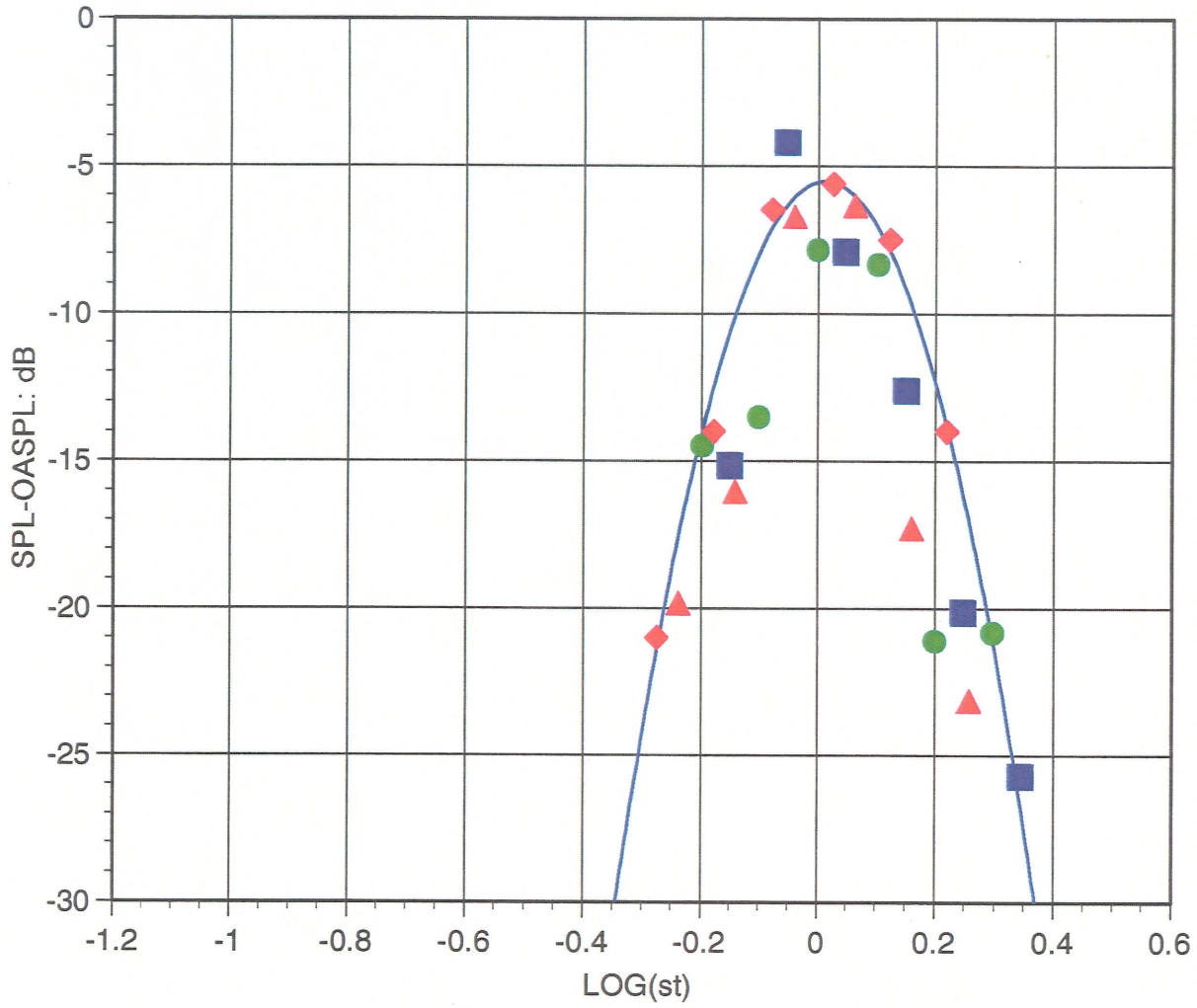

Figure 4-10 Normalized 1/3-Octave SPL: Mid - Frequency Component : 2-wheel, clean/ dirty, large tires, M = 0.18, 0.2, 0.22, 0.24, θ = 120°

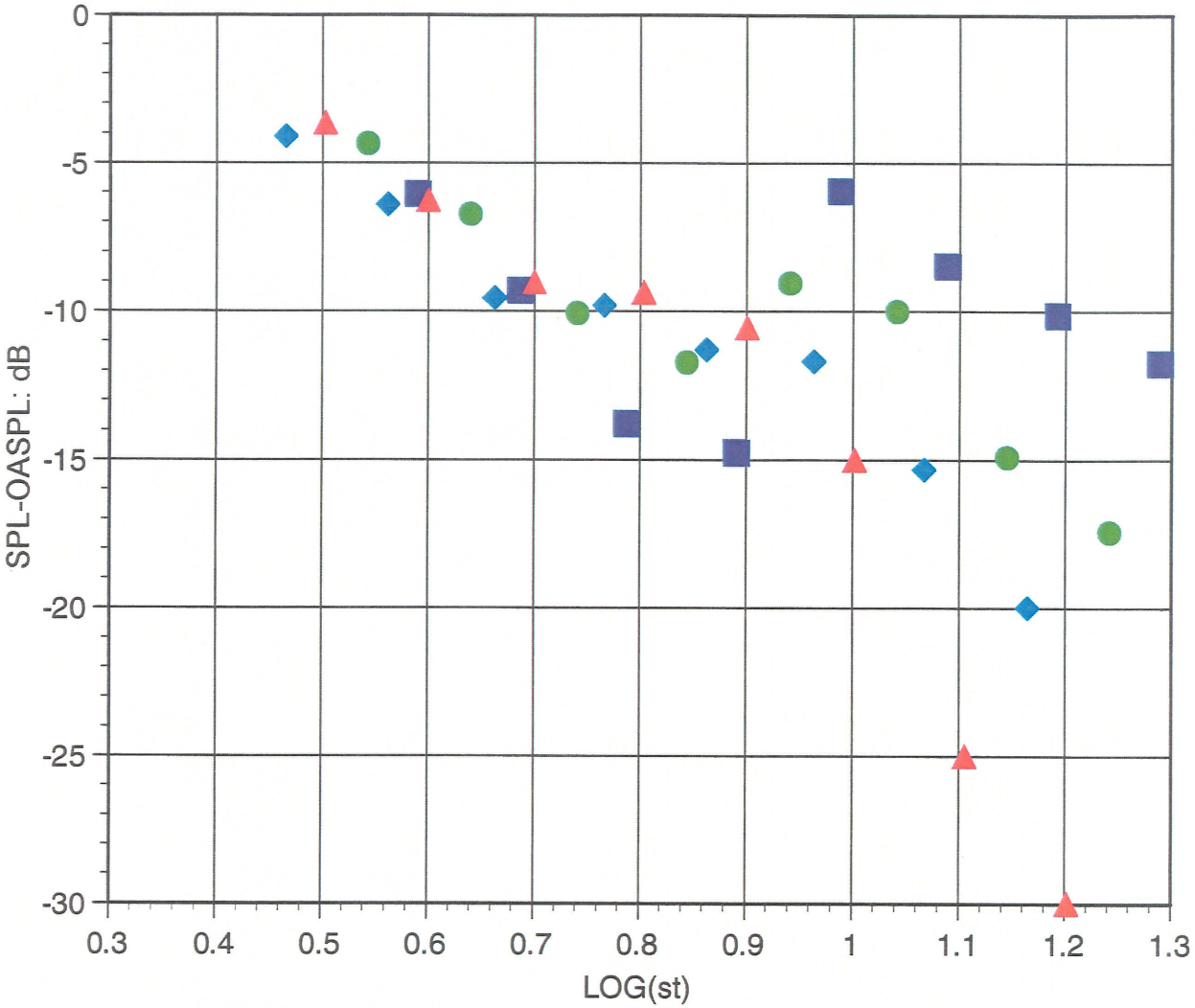

Figure 4-11 Normalized 1/3-Octave SPL: Tire Noise Component : dirty: 2-wheels/6-wheels, large tires, M = 0.18, 0.2, 0.22, 0.24, θ = 60°

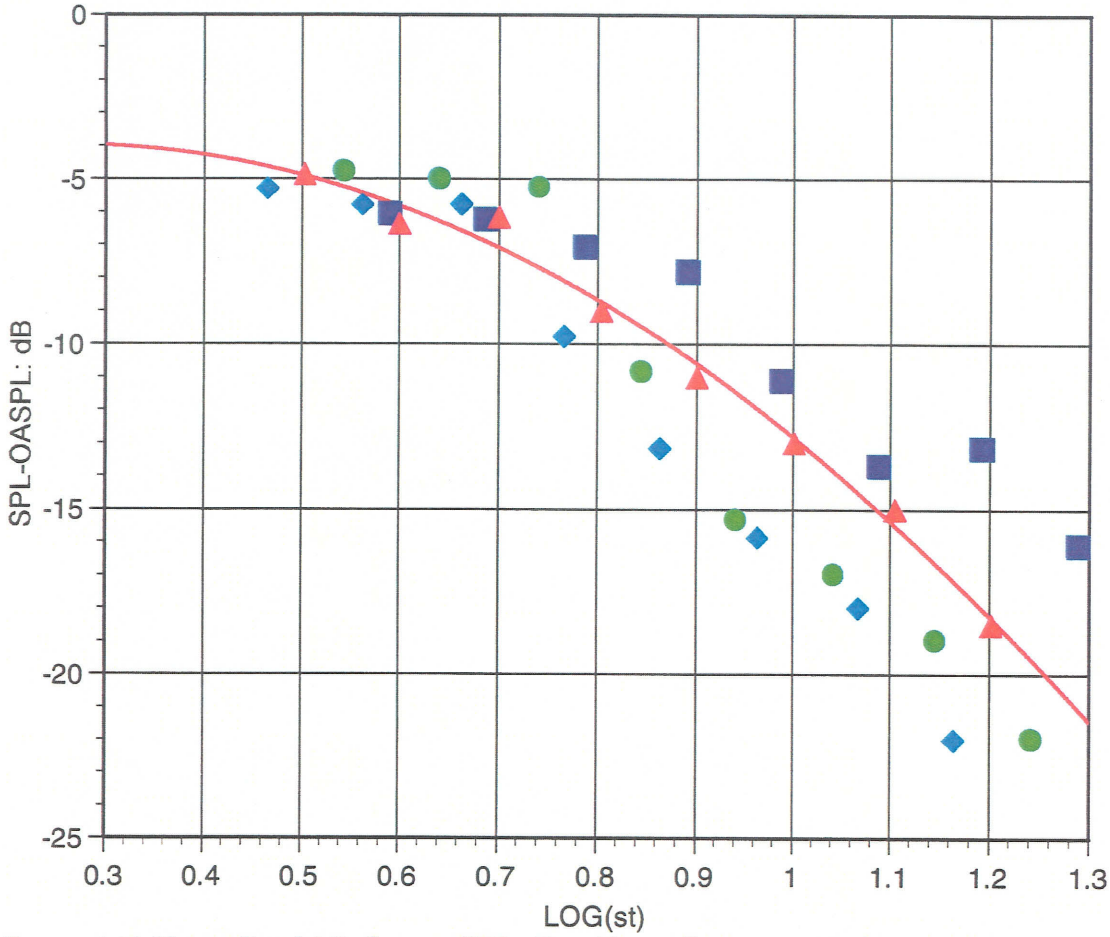

Figure 4-12 Normalized 1/3-Octave SPL: Tire Noise Component : dirty, 2-wheels/6-wheels, M = 0.18, 0.2, 0.22, , θ = 90°

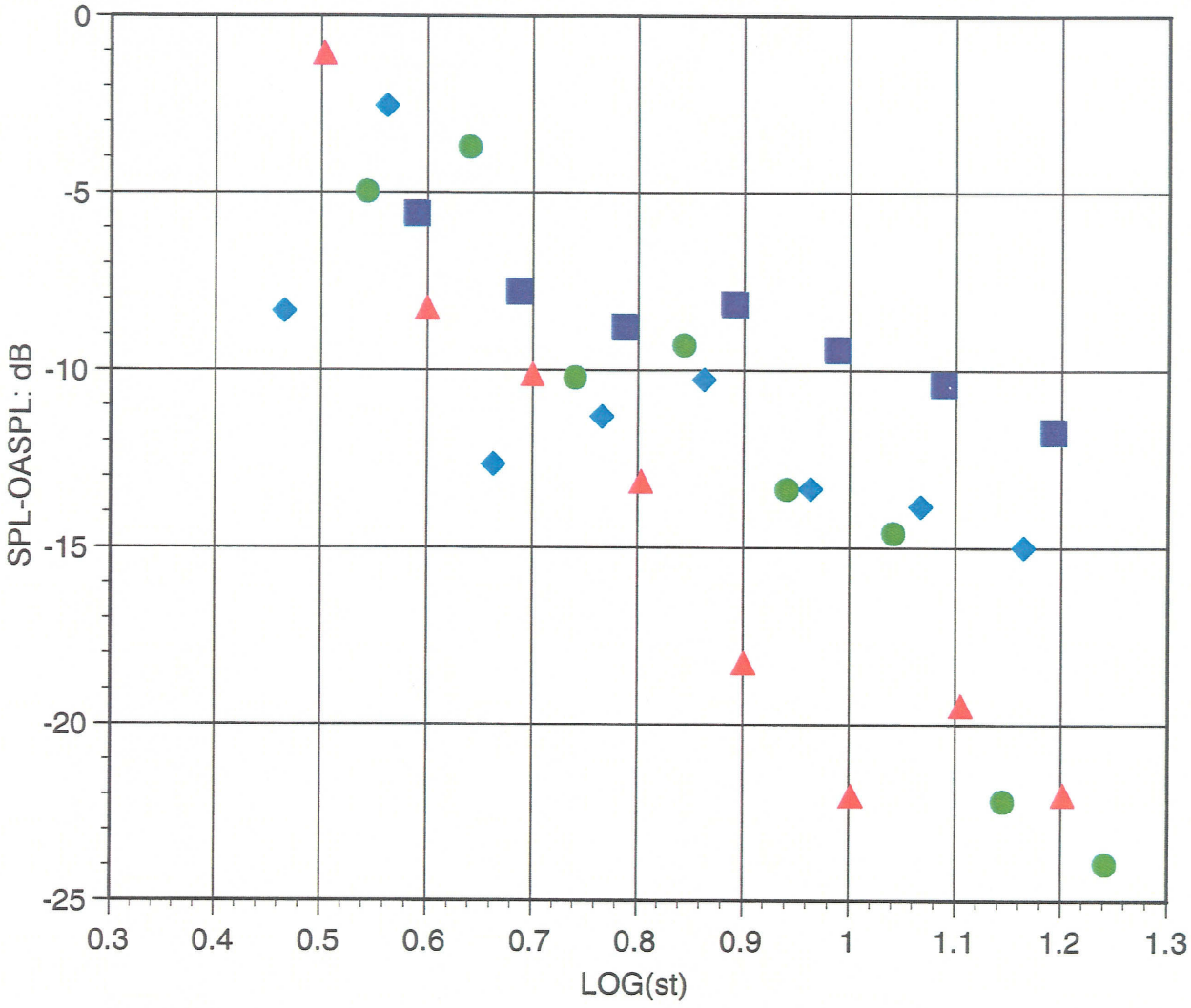

Figure 4-13 Normalized 1/3-Octave SPL: Tire Noise Component : dirty, 2-wheels/6-wheels, M = 0.18, 0.2, 0.22, , θ = 140°

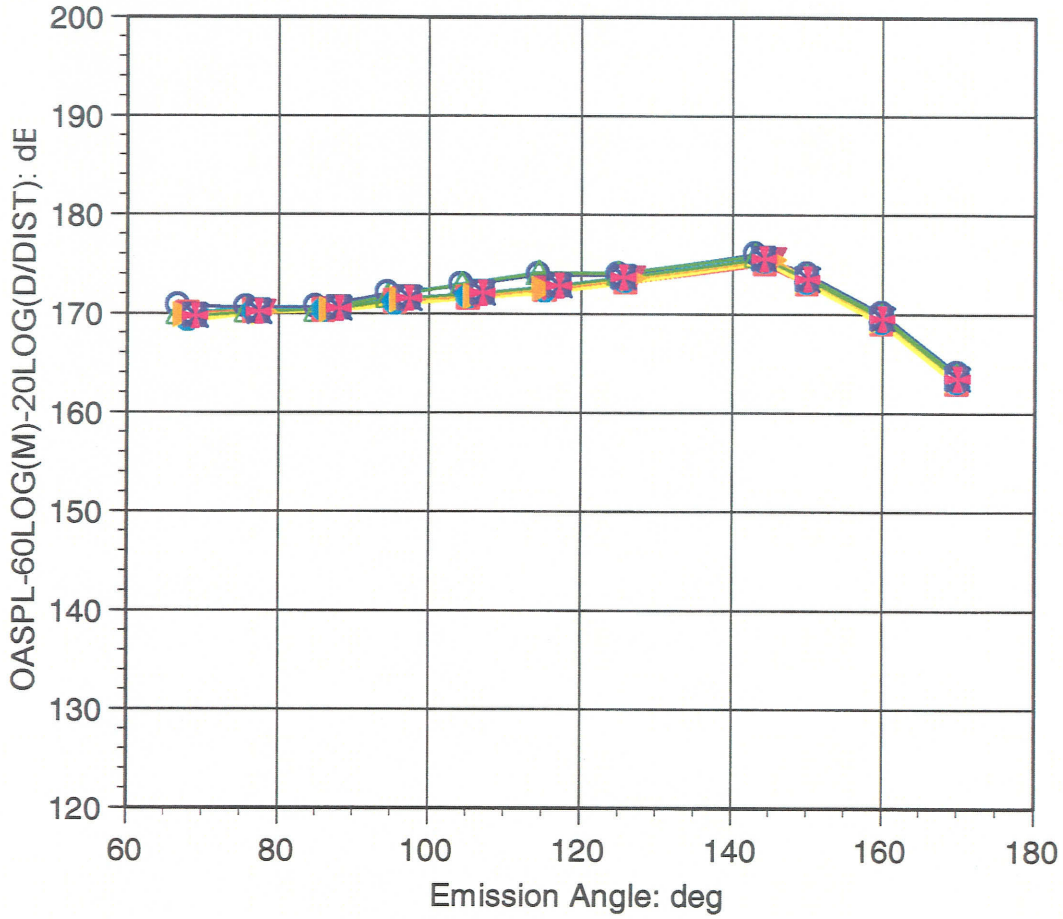

Figure 4-14 Normalized OASPL Directivity: Low Frequency Component : clean, 2-wheels, no tire/small tire, M = 0.18, 0.2, 0.22, 0.24

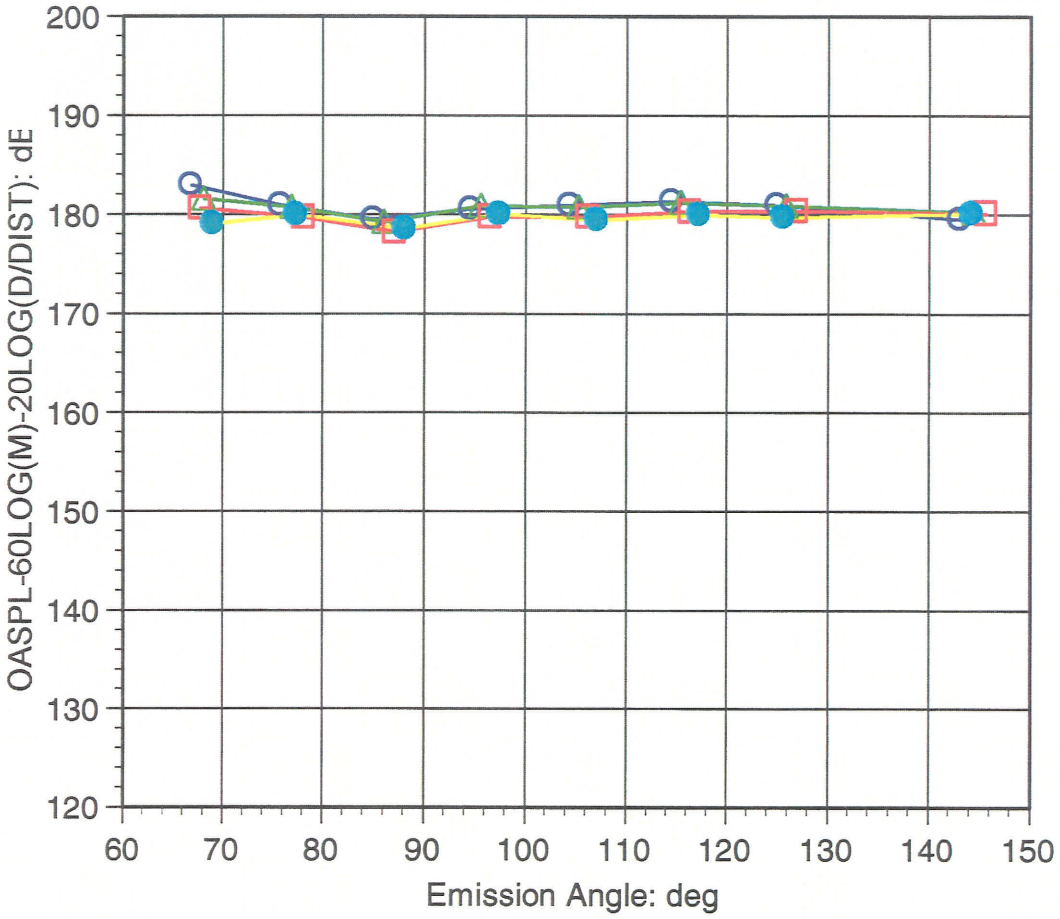

Figure 4-15 Normalized OASPL Directivity: High Frequency Component : clean/dirty, no tire/2-small tires, M = 0.18, 0.2, 0.22, 0.24

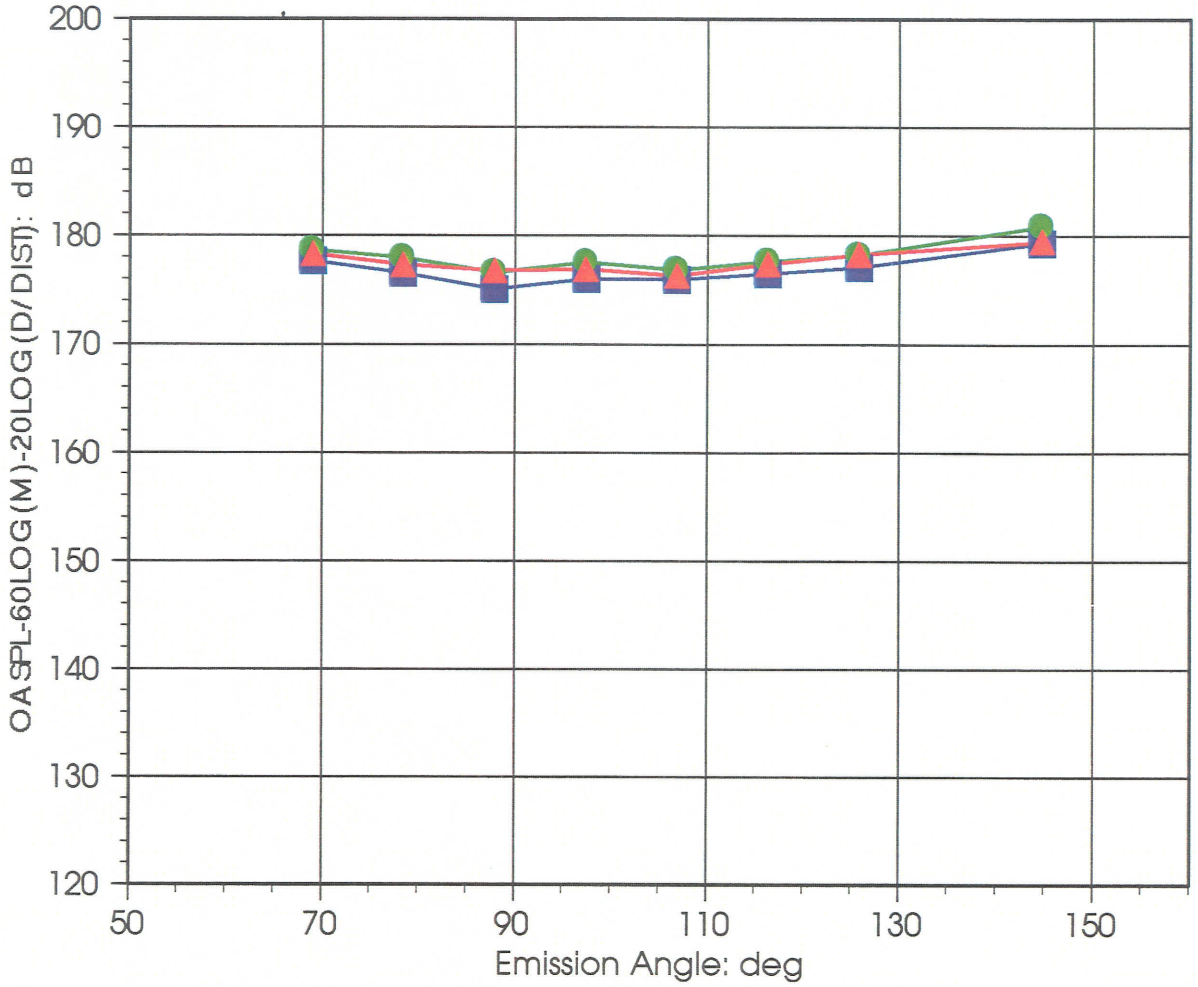

Figure 4-16 Normalized OASPL Directivity: Mid-Frequency Component : clean/dirty, no tire/2-large tires, M = 0.18, 0.2, 0.22, 0.24

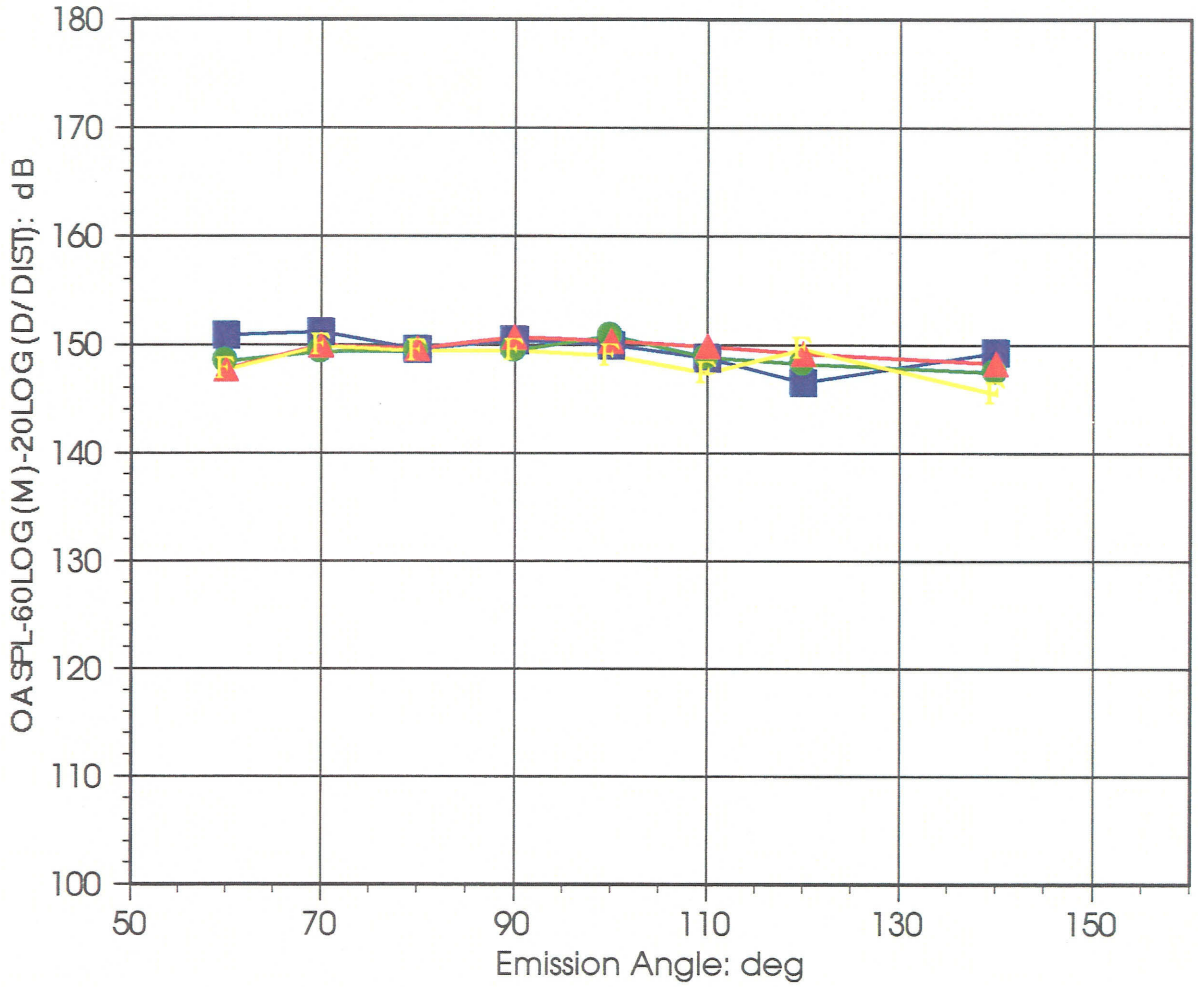

Figure 4-17 Normalized OASPL Directivity: Tire Noise Component : dirty, 2-wheels/6-wheels, large tire M = 0.18, 0.2, 0.22, 0.24

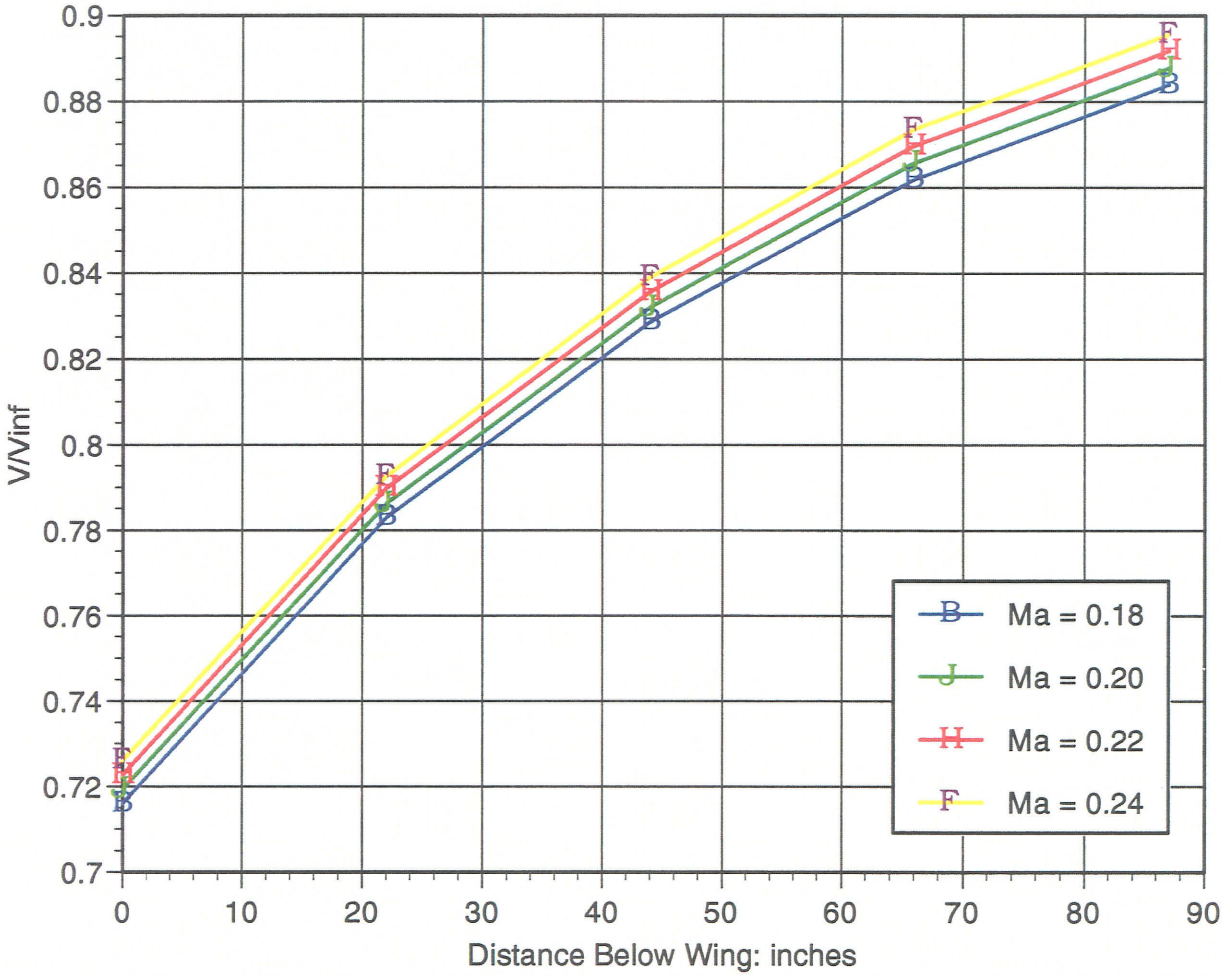

Figure 4-18 Vertical Distribution of Local Flow Mach Number calculated by Panel Code: B378-400 (under the wing) Flap Angle = 30°, Pitch Angle = 4°

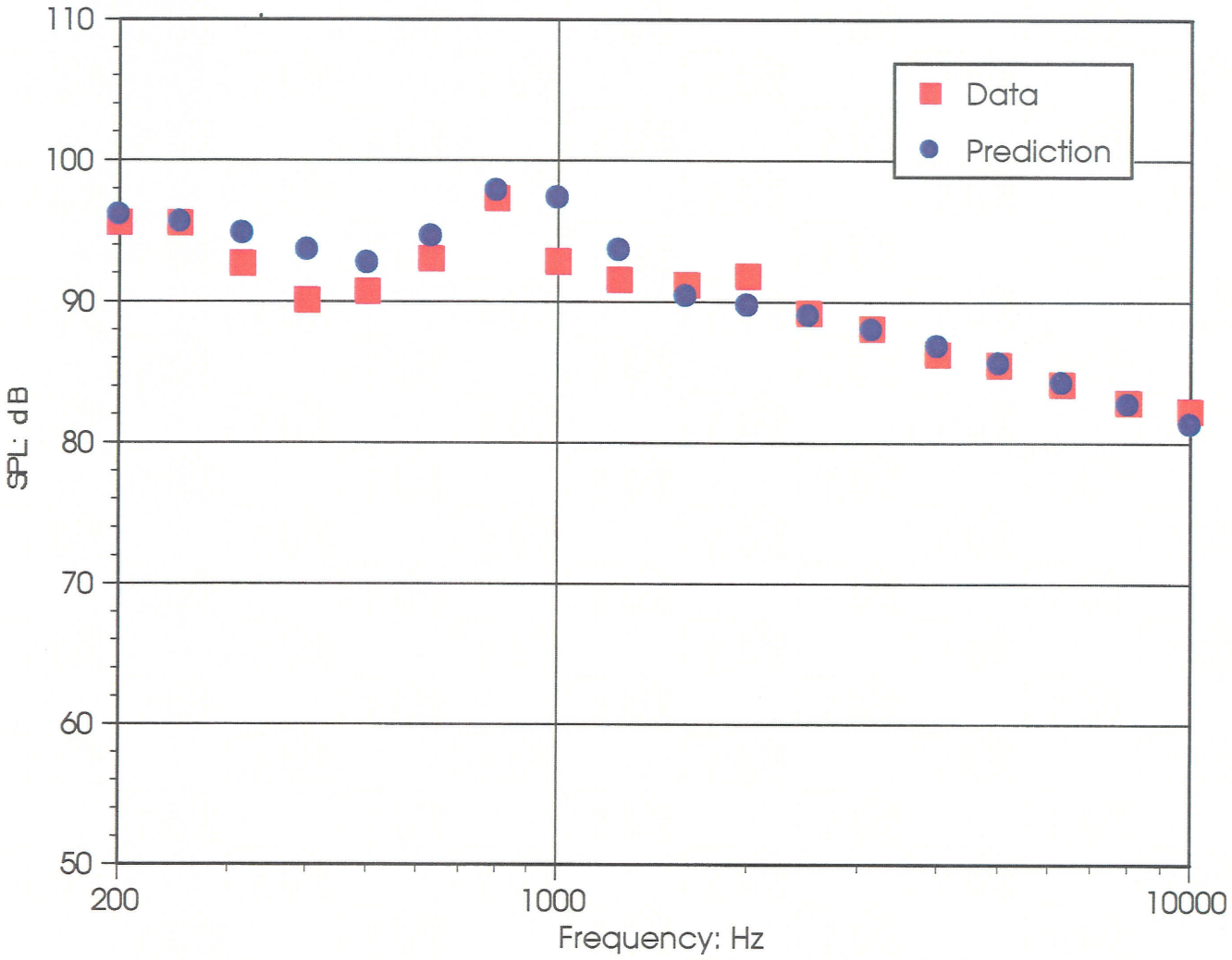

Figure 4-19 Spectral Comparison: Data versus Prediction : Run 22, dirty, 2-wheels, large tire, M = 0.24, θ = 60°

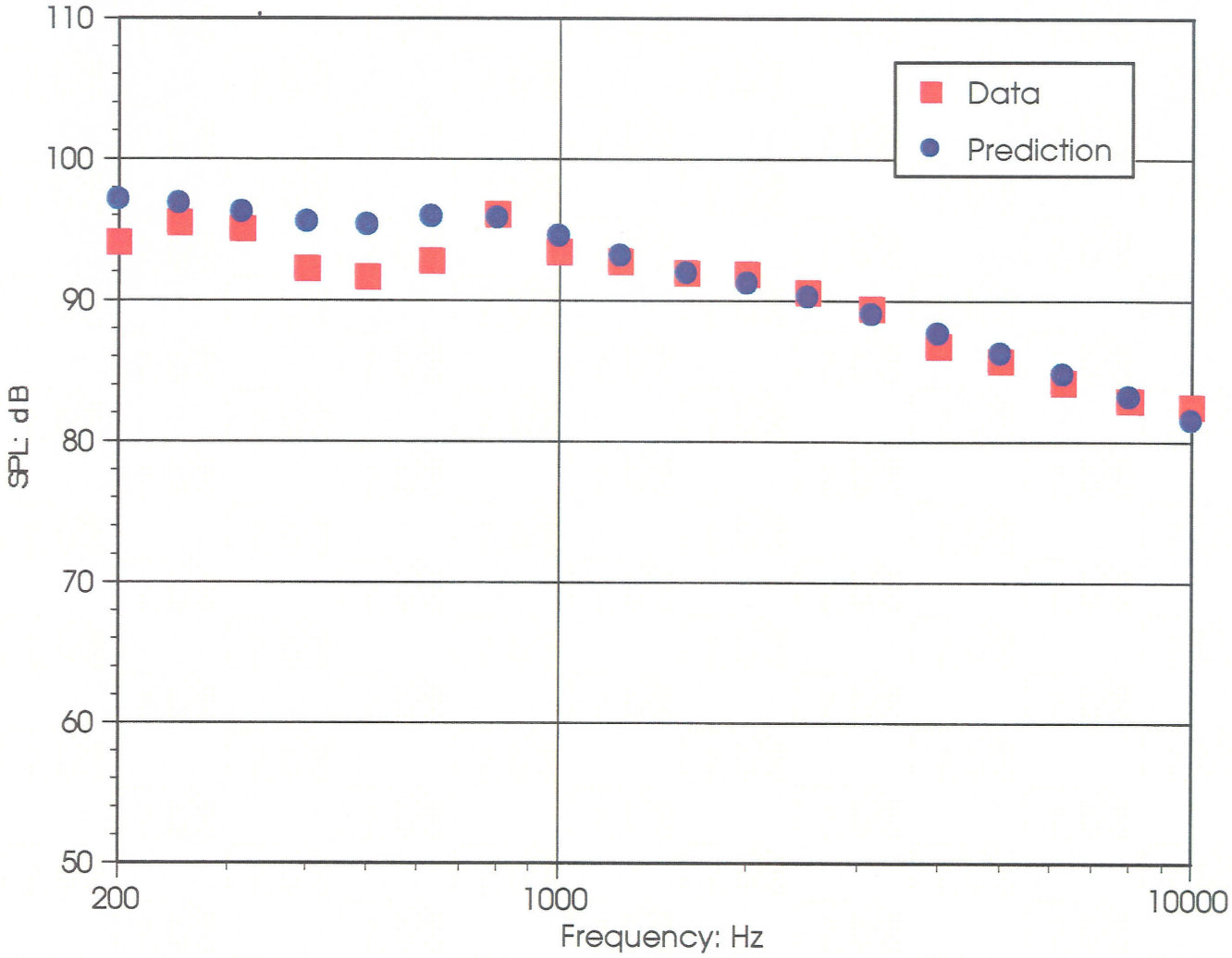

Figure 4-20 Spectral Comparison: Data versus Prediction : Run 22, dirty, 2-wheels, large tire, M = 0.24, $\theta = 90°$

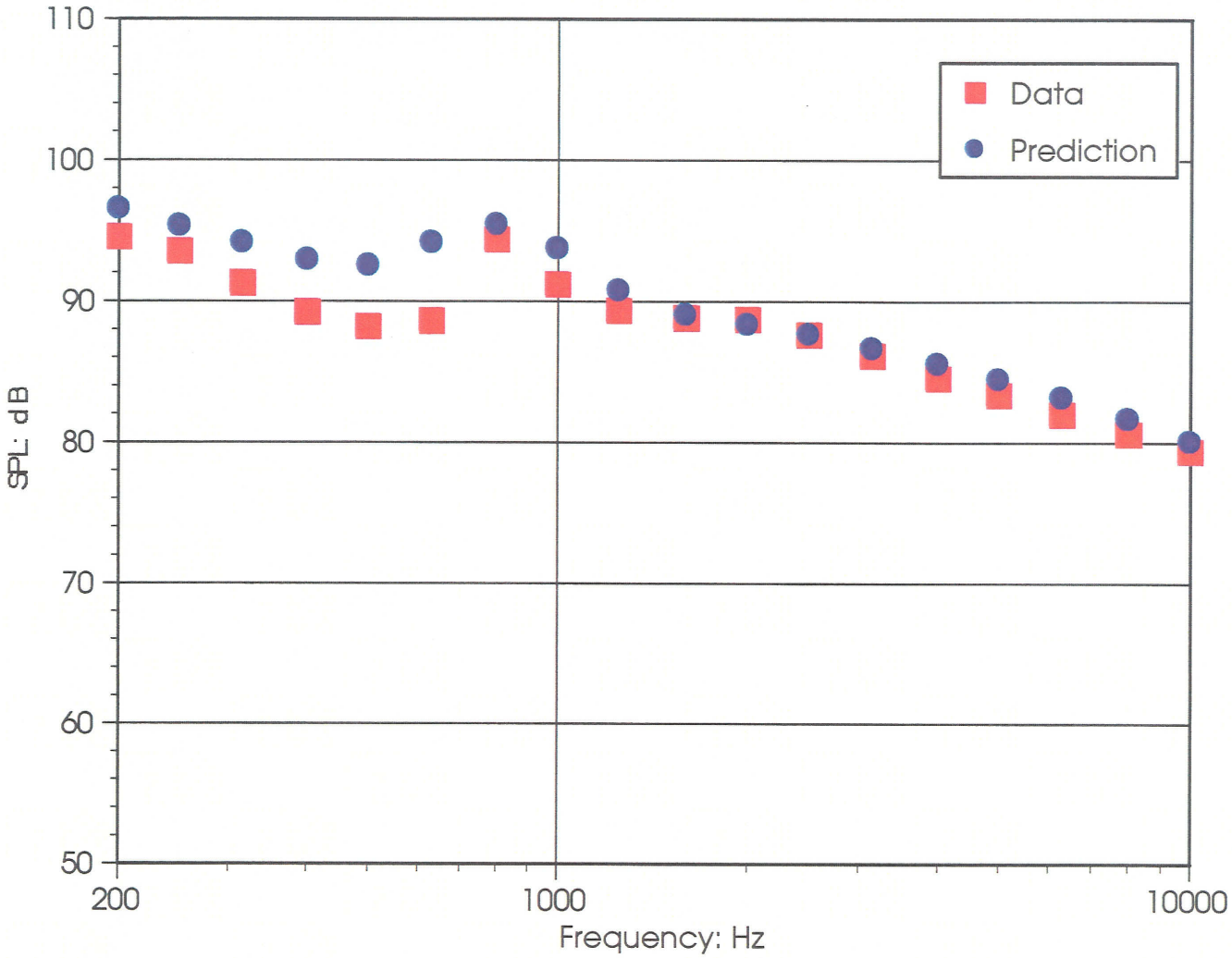

Figure 4-21 Spectral Comparison: Data versus Prediction :: Run 22, dirty, 2-wheels, large tire, $M = 0.24$, $\theta = 140°$

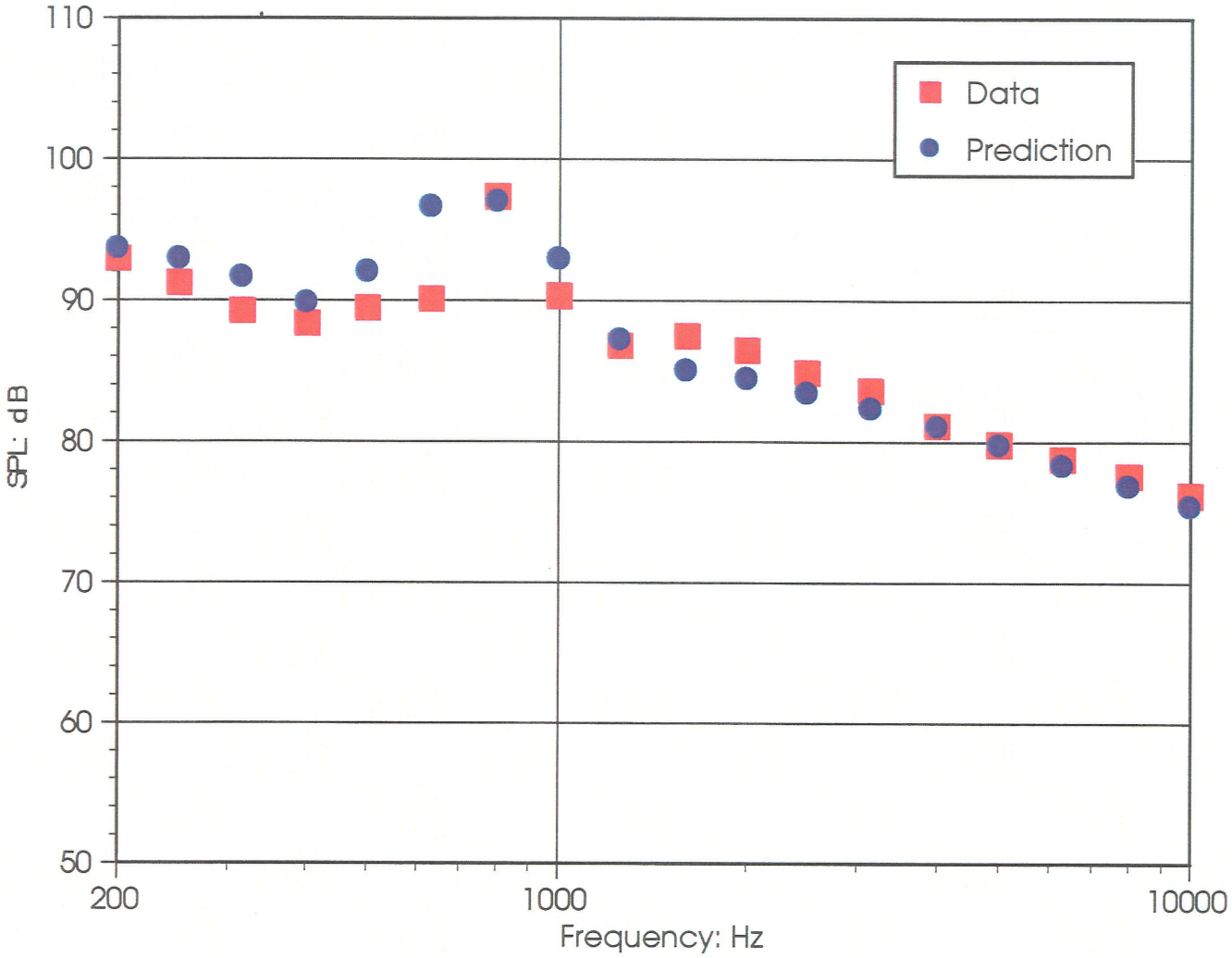

Figure 4-22 Spectral Comparison: Data versus Prediction : Run 132, dirty, 6-wheels, large tire, $M = 0.20$, $\theta = 60°$

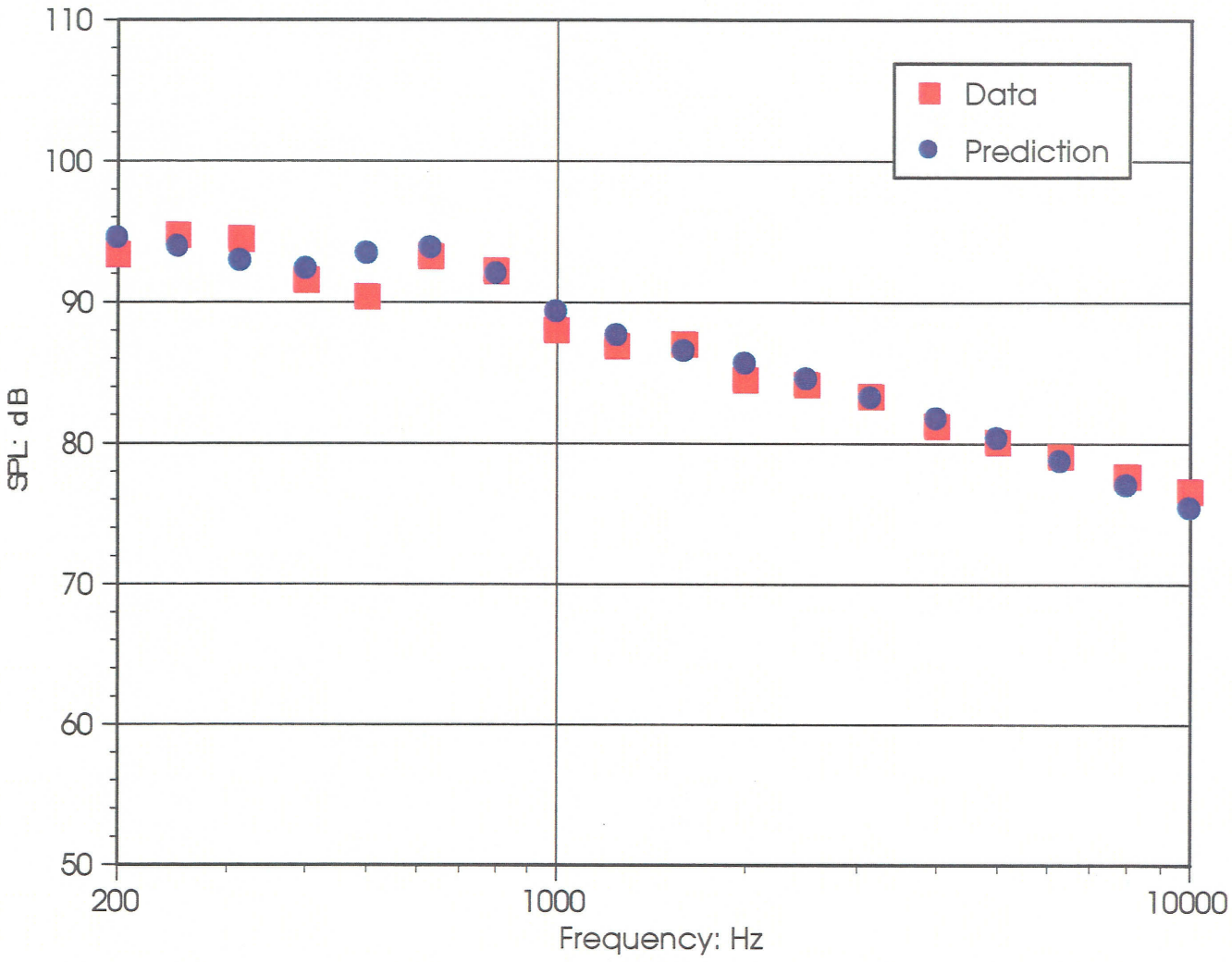

Figure 4-23 Spectral Comparison: Data versus Prediction : Run 132, dirty, 6-wheels, large tire, $M = 0.20$, $\theta = 90°$

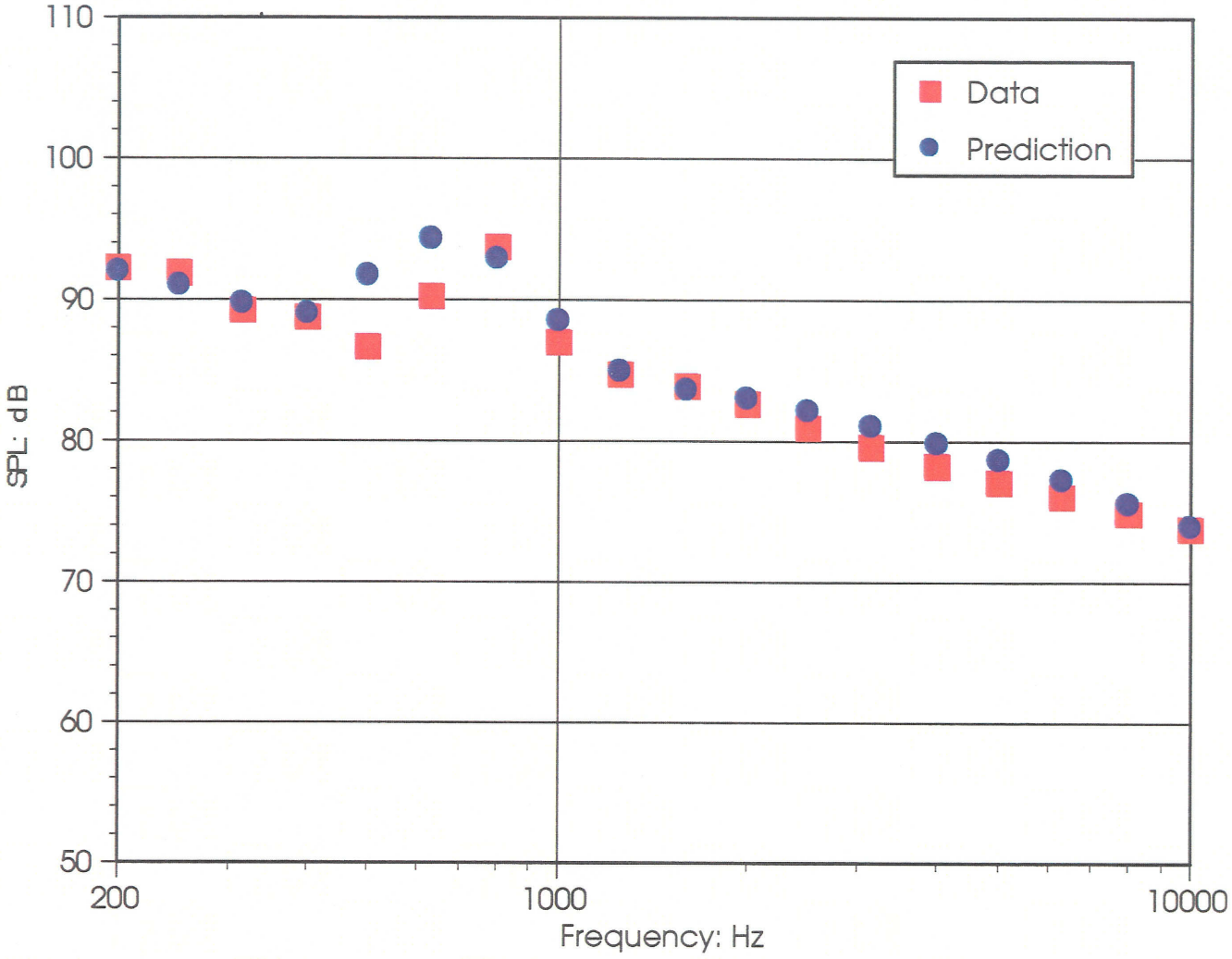

Figure 4-24 Spectral Comparison: Data versus Prediction : Run 132, dirty, 6-wheels, large tire, $M = 0.20$, $\theta = 140°$

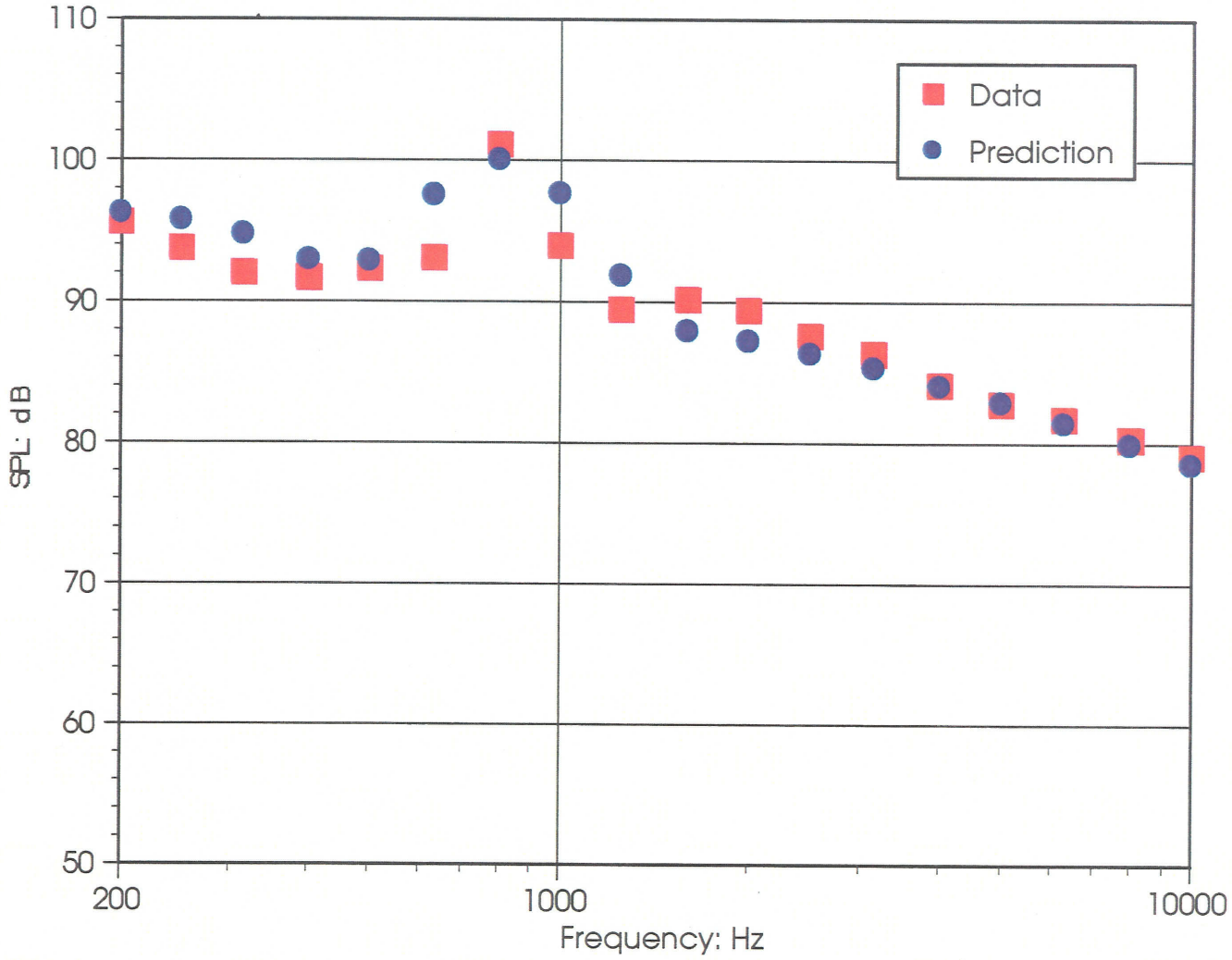

Figure 4-25 Spectral Comparison: Data versus Prediction : Run 133, dirty, 6-wheels, large tire, $M = 0.22$, $\theta = 60°$

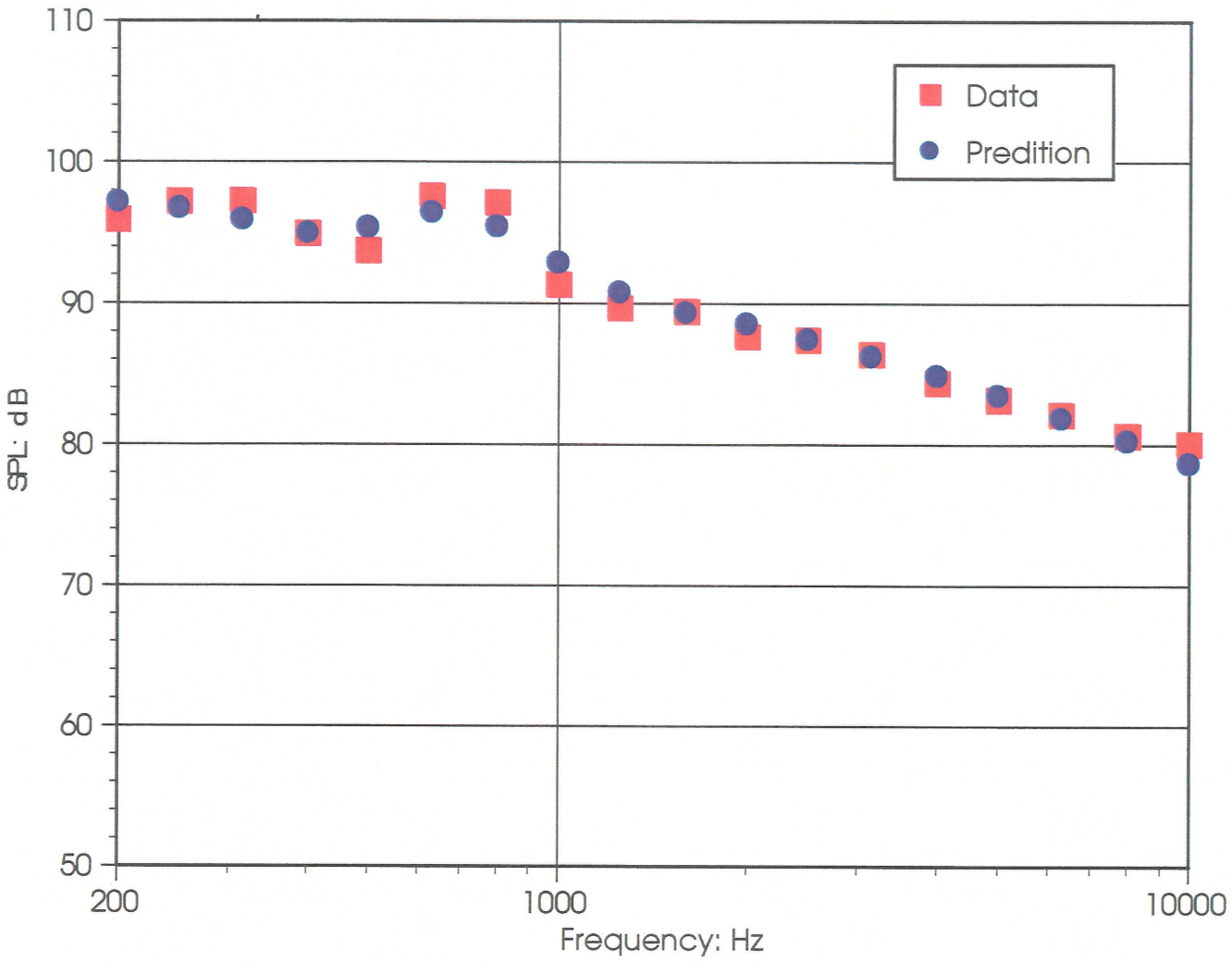

Figure 4-26 Spectral Comparison: Data versus Prediction : Run 133, dirty, 6-wheels, large tire, $M = 0.22$, $\theta = 90°$

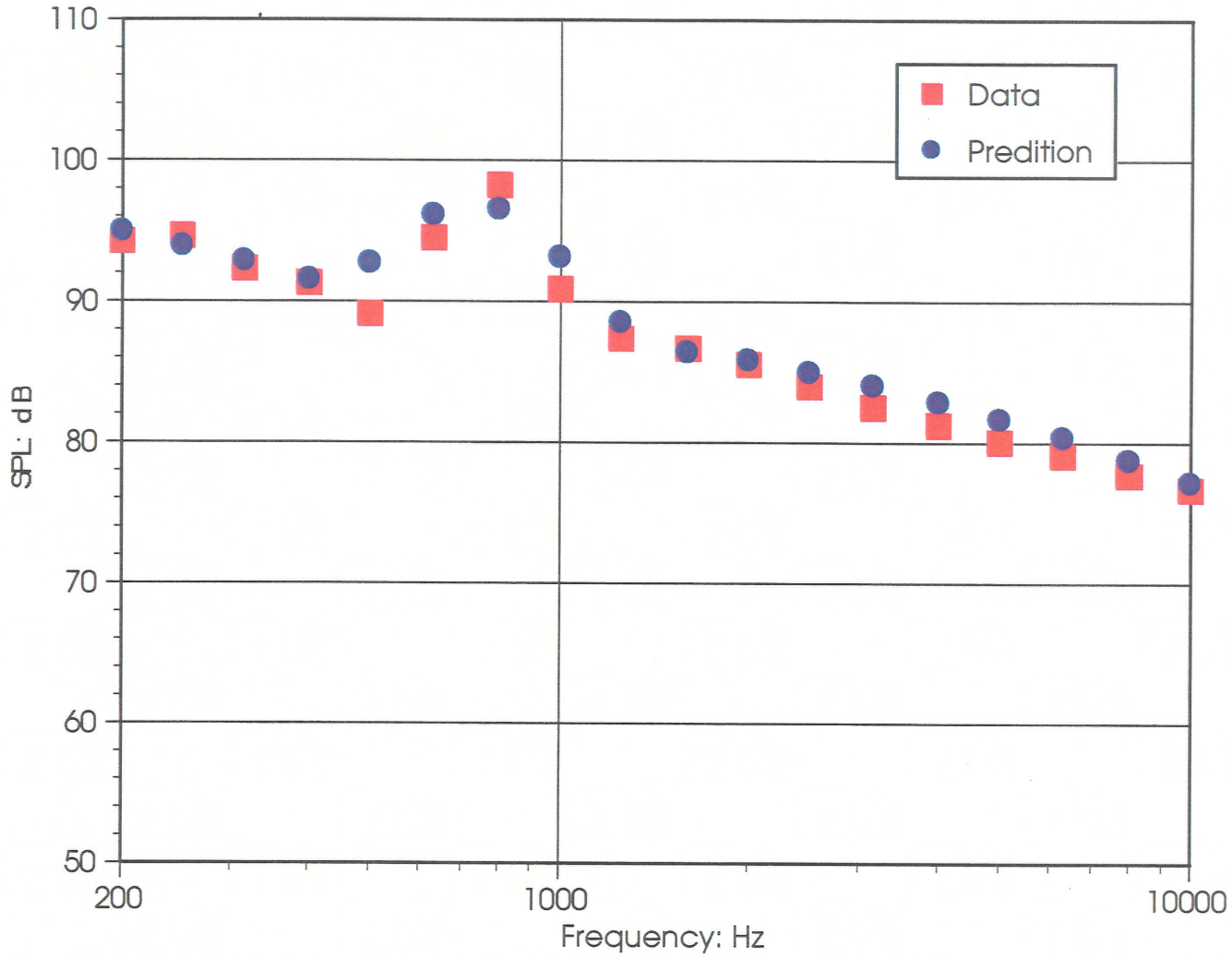

Figure 4-27 Spectral Comparison: Data versus Prediction : Run 133, dirty, 6-wheels, large tire, $M = 0.22$, $\theta = 140°$

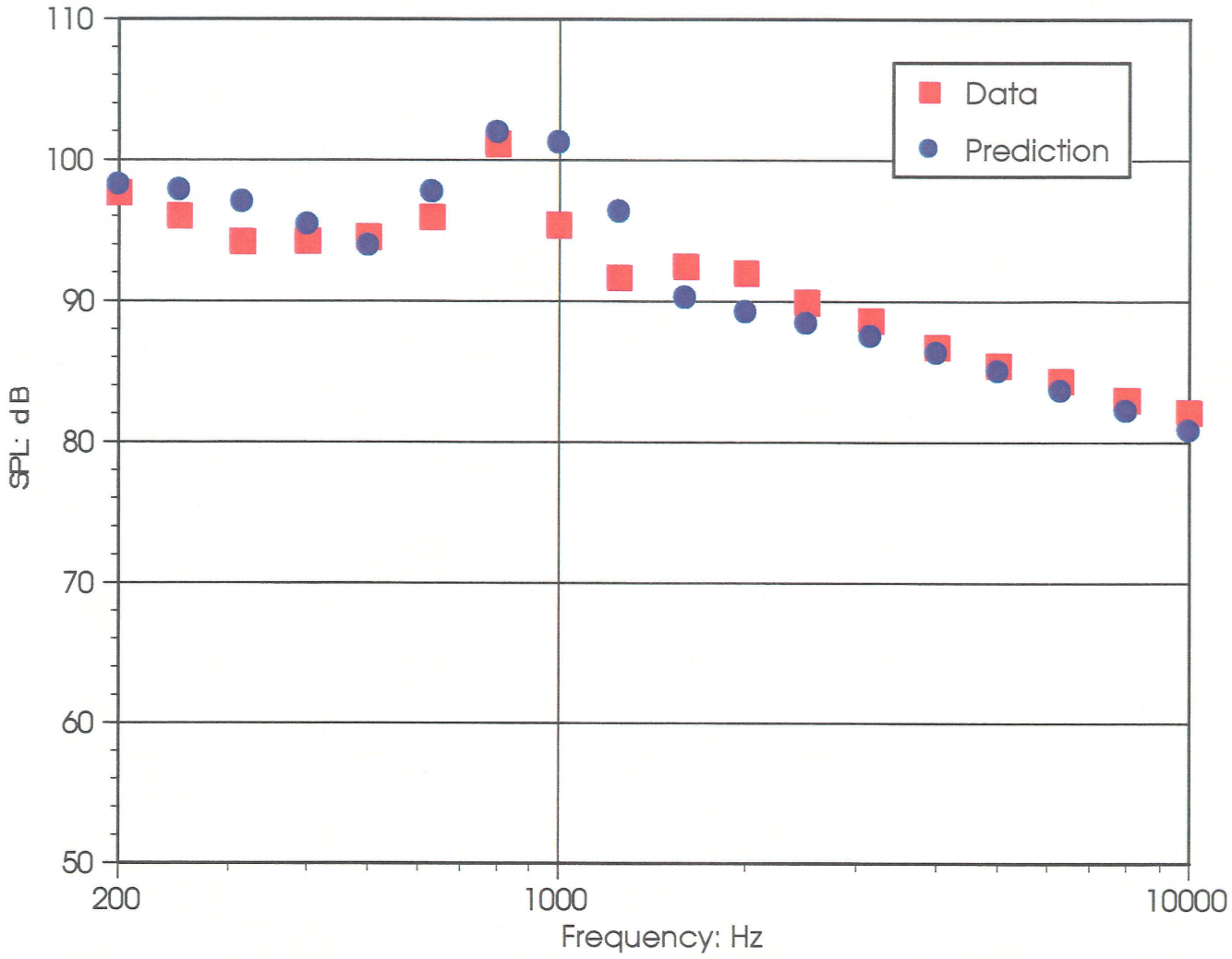

Figure 4-28 Spectral Comparison: Data versus Prediction : Run 134, dirty, 6-wheels, large tire, M = 0.24, θ = 60°

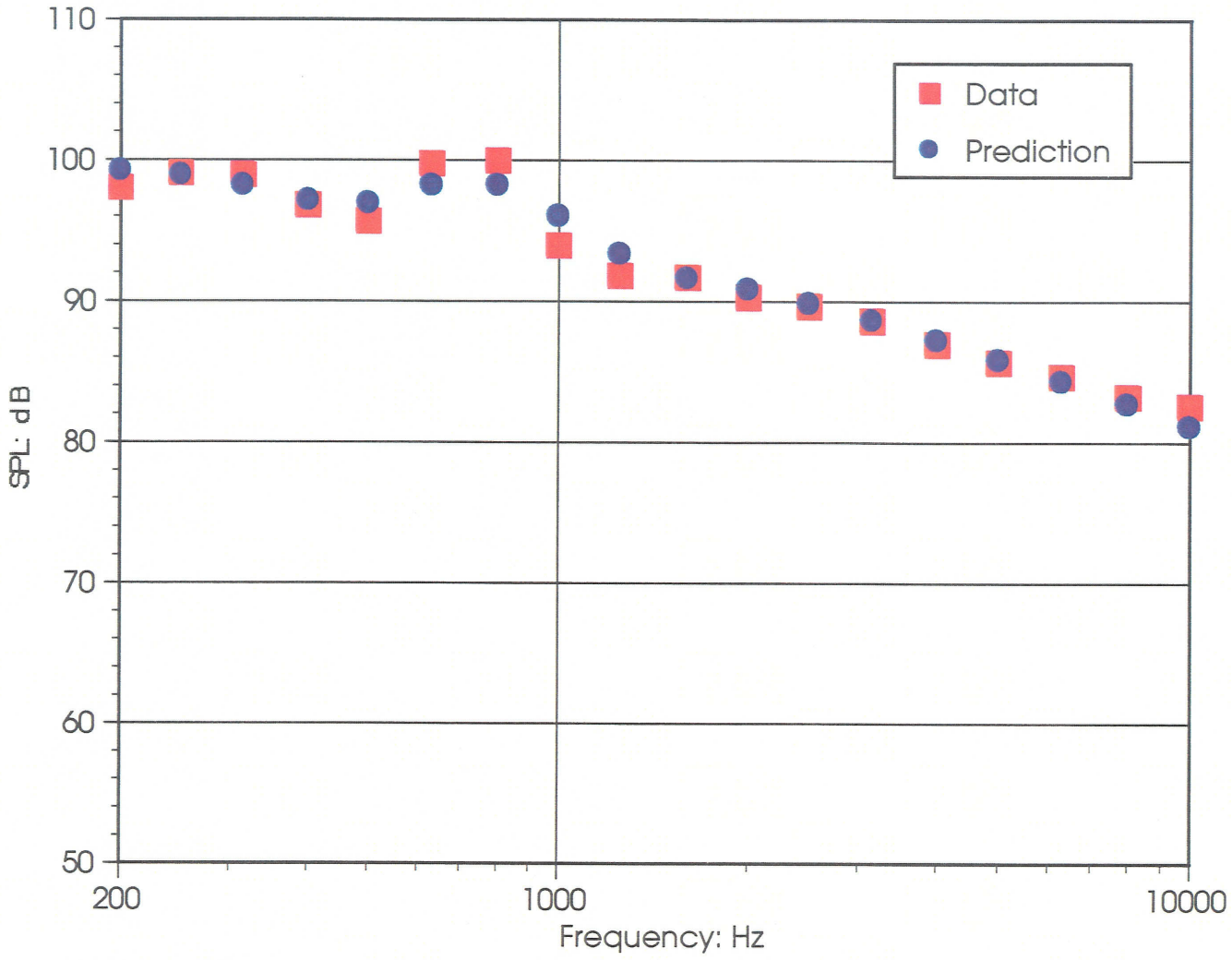

Figure 4-29 Spectral Comparison: Data versus Prediction : Run 134, dirty, 6-wheels, large tire, $M = 0.24$, $\theta = 90°$

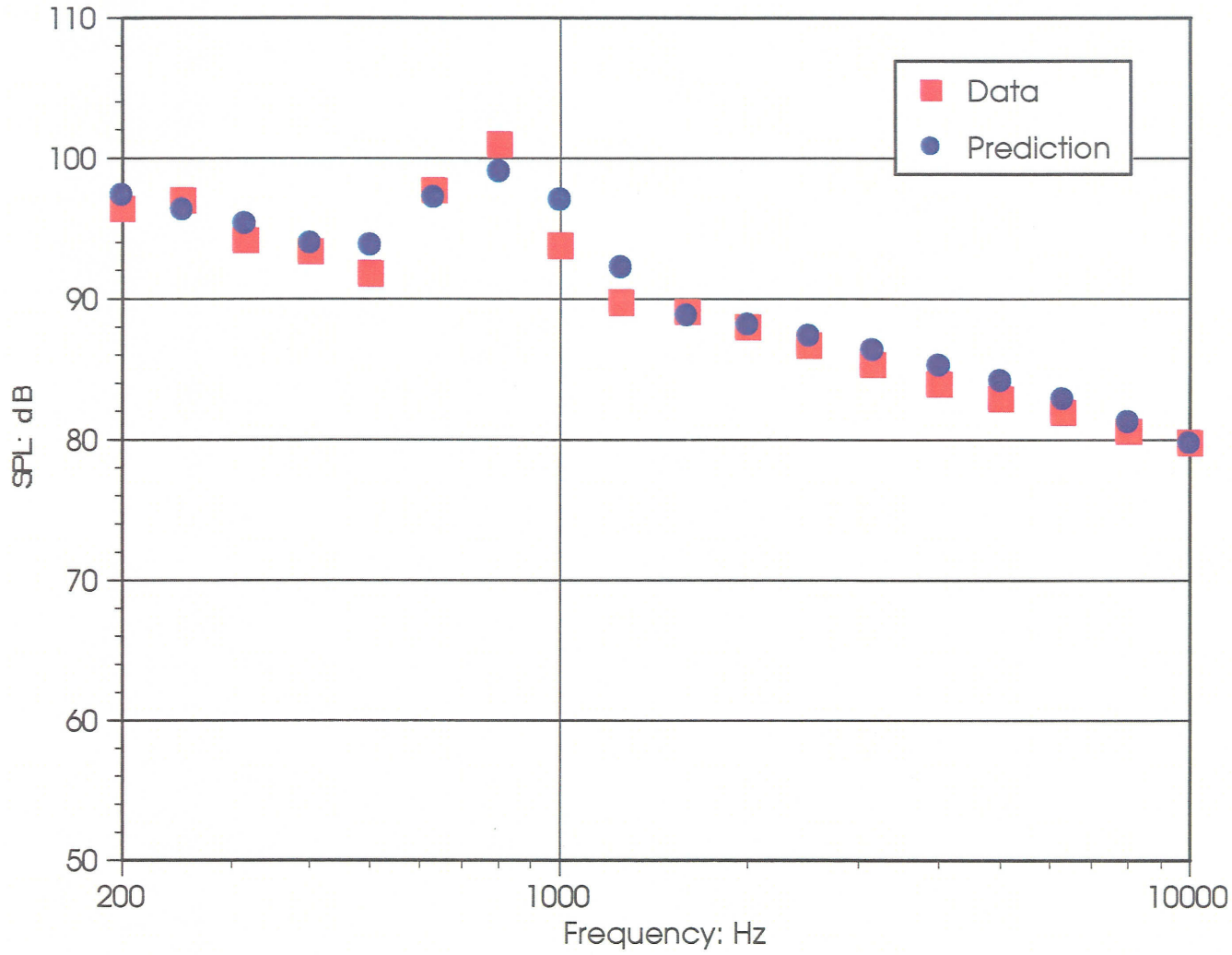

Figure 4-30 Spectral Comparison: Data versus Prediction : Run 134, dirty, 6-wheels, large tire, $M = 0.24$, $\theta = 140°$

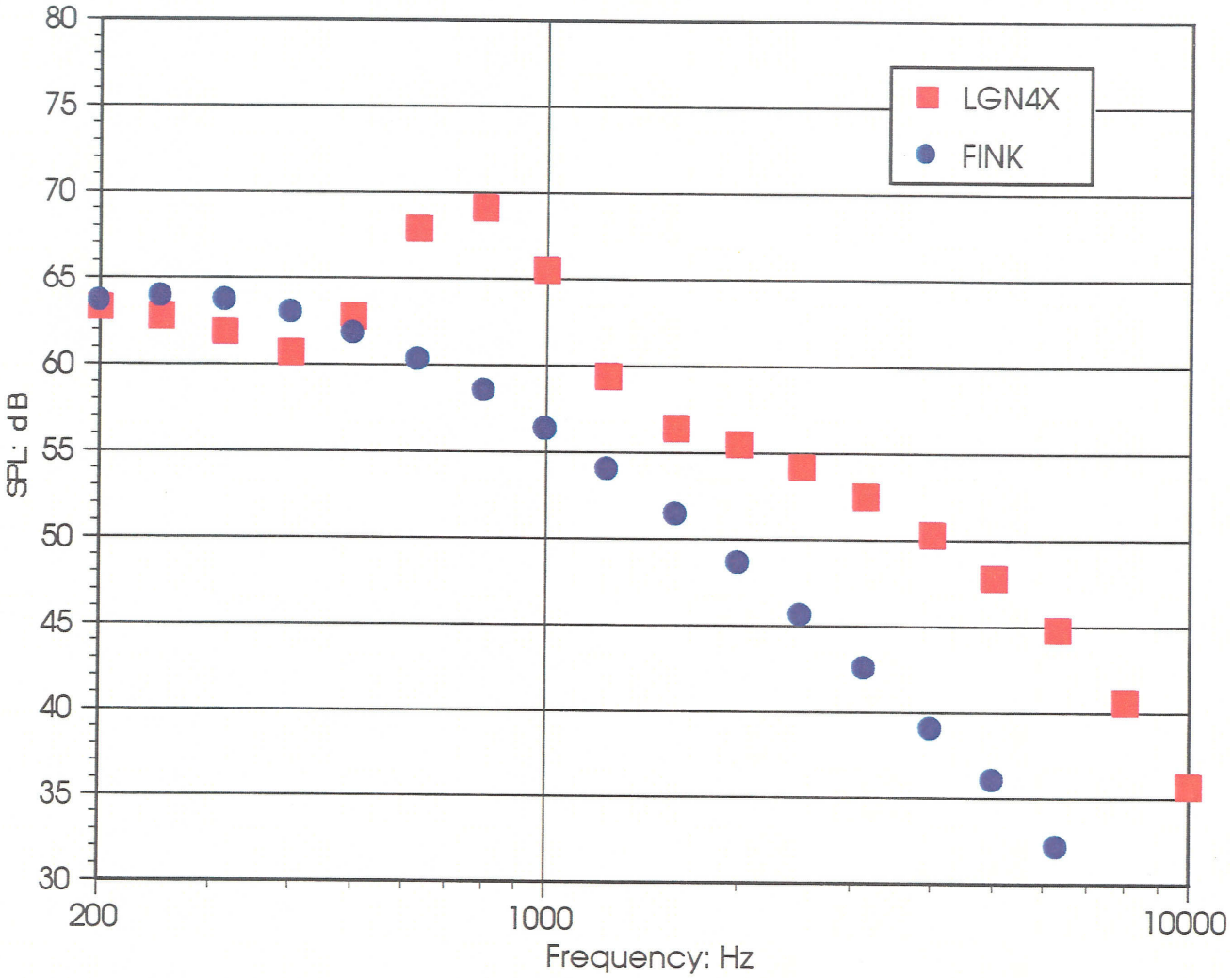

Figure 4-31 Spectral Comparison: Fink's Model versus LGN4X (present model) : B737, Approach Conditions, M = 0.24, θ = 50°

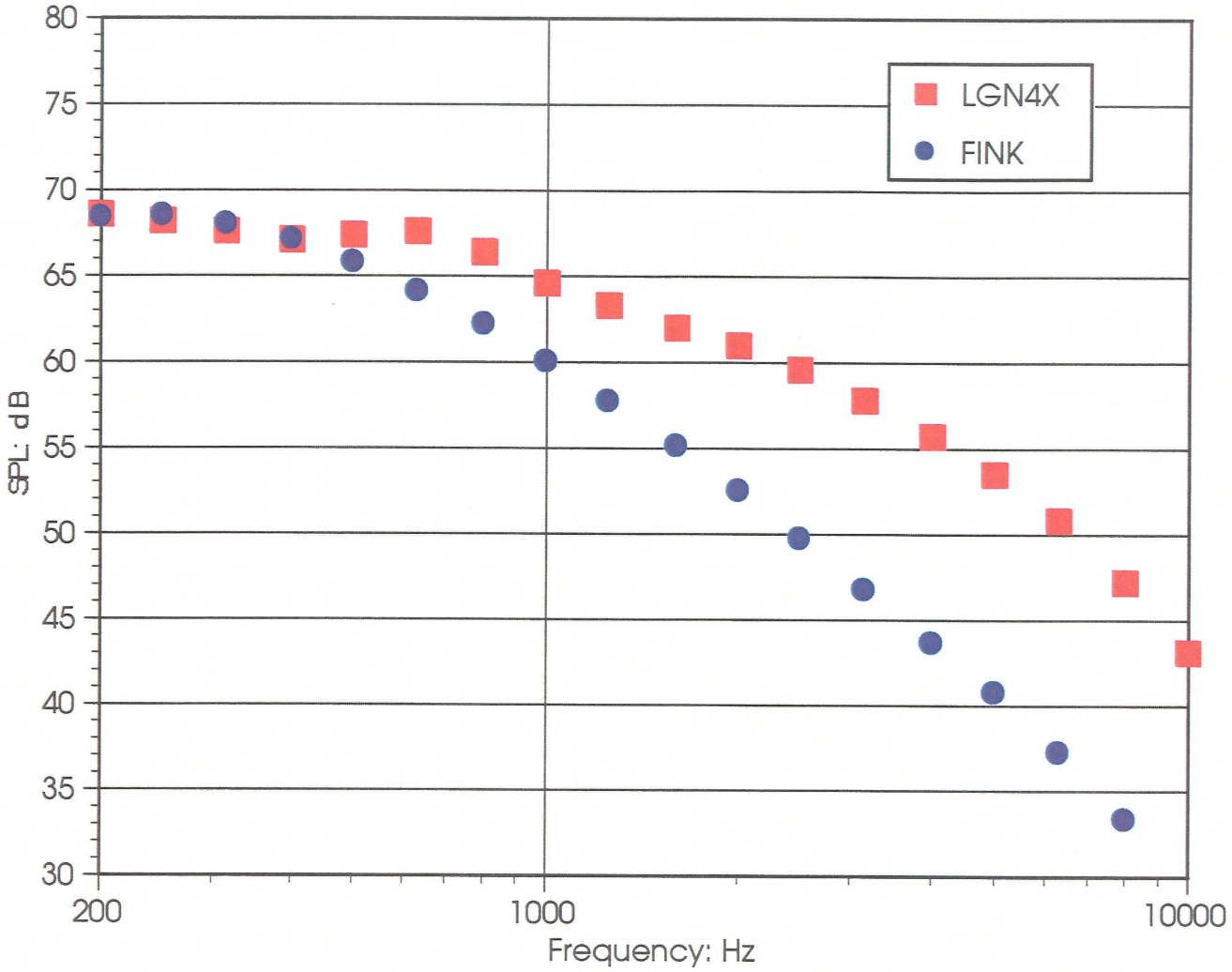

Figure 4-32 Spectral Comparison: Fink's Model versus LGN4X (present model) : B737, Approach Conditions, M = 0.24, θ = 90°

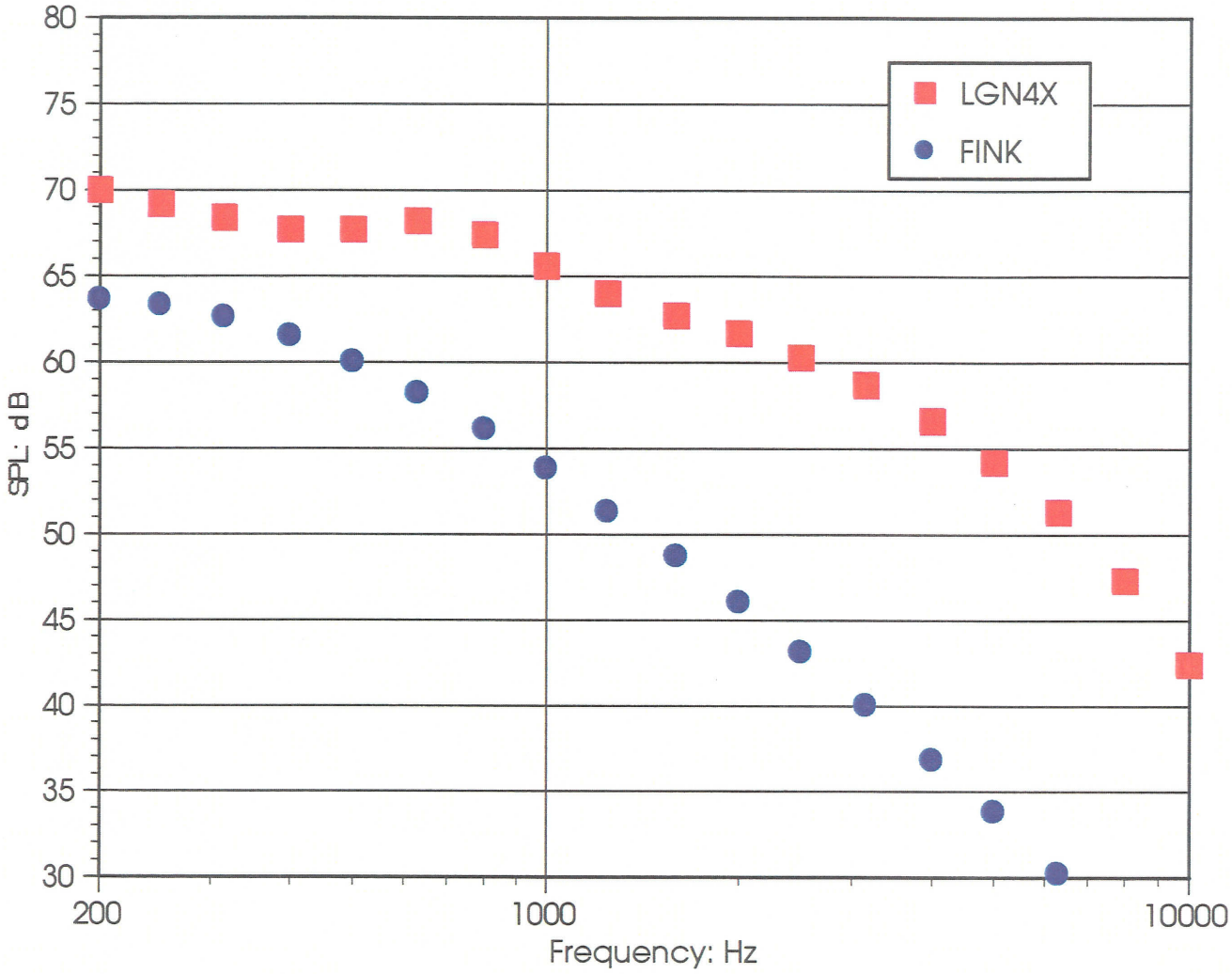

Figure 4-33 Spectral Comparison: Fink's Model versus LGN4X (present model) : B737, Approach Conditions, M = 0.24, θ = 130°

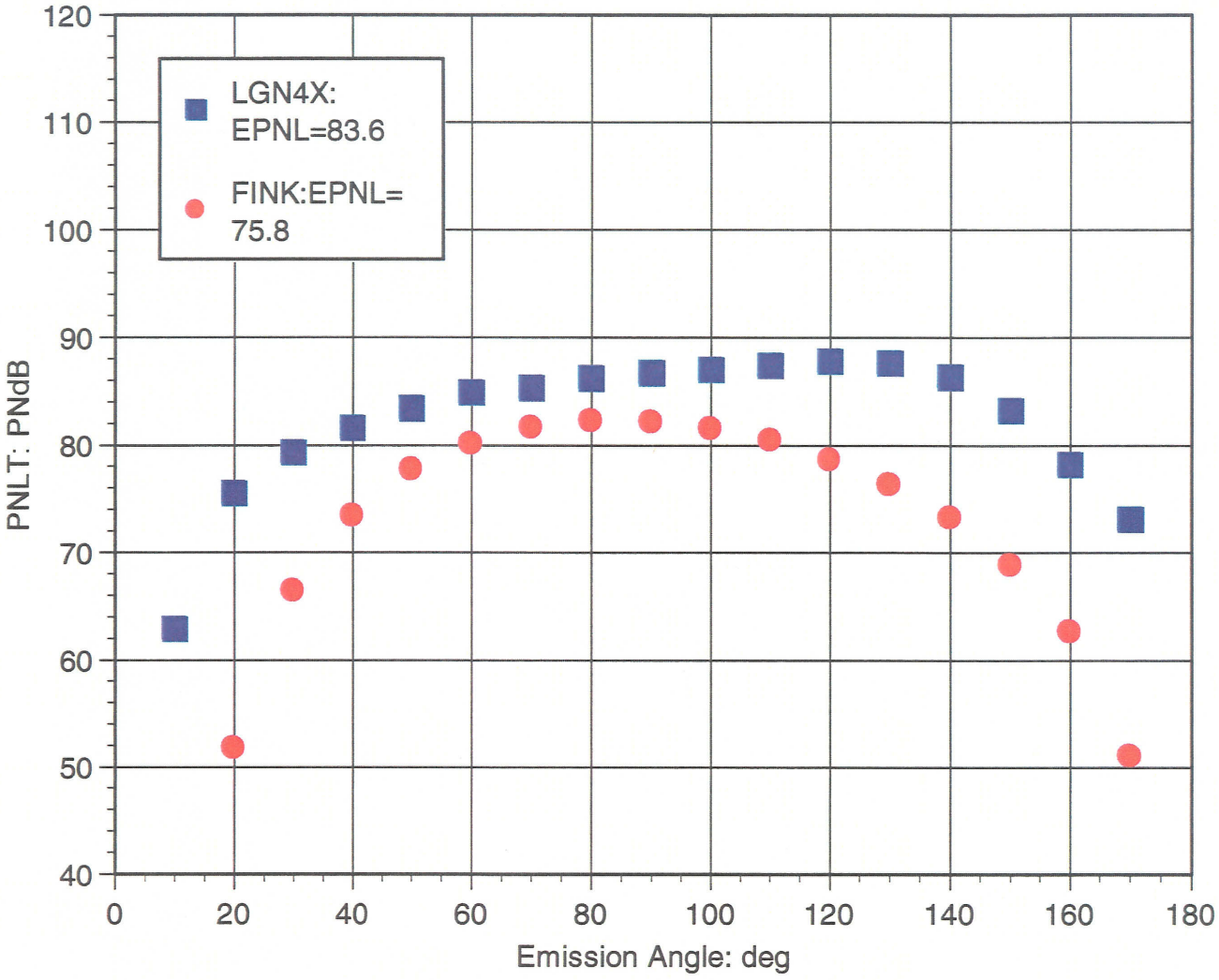

Figure 4-34 PNLT Directivity Comparison: Fink's Model versus LGN4X : B737 Approach Conditions, M = 0.24

5 Aerodynamics Calculations

5.1 Panel calculations

5.1.1 Overview

We analyzed several different Boeing 7-series airplane configurations using the panel codes A449 and A502, and the MD-11 using DACVINE. The following is a brief description of the configurations analyzed, the panel codes, their use, and the utility of the aerodynamic results.

The aircraft of interest, (i.e. those for which aerodynamic noise data already existed) were the 737-300 (737 Classic), 737-700 (737 Next Generation), 757, 767, 777, MD-11. Flap deflections matched those tested in the wind tunnel, including non-standard deflections, and even some non-standard flap geometry. A449 and A502 analysis of the 7-series airplanes was performed by Boeing Seattle, but the DACVINE analysis was performed by Boeing, Long Beach by aerodynamicists more familiar with the MD-11. The present discussion will focus on the A449 and A502 analyses. The following table lists the cases completed:

Table 5-1 : Panel code analysis cases

Airplane	**Flaps**	α	**Analysis**	
737-300	detent 25	6.4, 6.7	A449	
737-300	detent 30	4.7,6.4,6.7,8.7	A449	
737-300	detent 40	4,6,8	A449	A502
737-700	27° (angle of main flap)	4,6,8		A502
737-700	27°, gear flowfield	4		A502
737-700	27°	4.7,6.4,6.7,8.7	A449	
737-700	25° Singe-slotted OB	4,6,8	A449	
737-700	34° Singe-slotted OB	4,6,8	A449	
757	detent 20	7.7	A449	
757	36°	5.7,7.5,7.7,9.7	A449	
767	detent 30	0,2,4,6,8,10,12,14,15.5	A449	
777	detent 30	7.34,9.34	A449	
777	detent 30	7.34,9.34		A502
MD-11	Flaps 25, 35, 50	4.7	DACVINE	

5.1.2 A449 Lifting Surface Analysis:

A449 is a vortex lattice code that models lifting surfaces using networks of vortex panels, and a body using an axisymmetric slender body-theory approximation. The code differs from a strict vortex lattice formulation in that the chordwise variation of vortex panel strength is piecewise linear, rather than discrete on each panel. The planform, camber and twist of a lifting surface are defined by the panel network geometry, but thickness is not modeled. Dihedral and incidence can be specified for the entire lifting surface. A complete description of the theory and use of A449 can be found in Goldhammer (1979). In the present study, separate lifting surfaces were used to define the wing and individual flap elements, while the effect of leading edge slats was simulated by extending the leading edge of the wing forward and drooping it to match the planform and camber of the slat on the wing. Trailing vorticity is automatically continued directly downstream from the trailing edges of lifting surfaces. The body length and diameter matched the airplane geometry, but the slender body-theory formulation enforced axisymmetry, thus masking the (small) effects of a low nose + high cockpit windows at the front, gear fairings, and the up-swept aft body.

5.1.3 A502 & DACVINE Potential Flow Analysis:

A502 and DACVINE are both potential flow codes that solve for source & doublet distributions over a network of panels. The primary difference between the two codes is that these distributions are quadratic for A502, and linear for DACVINE. Panels are used to define the entire external surface of the aircraft and lifting surfaces possess both source & doublet distributions, The effect of thickness of a lifting surface is included, in contrast with the thin surface treatment in A449. The body is modeled by a network of source panels in the shape of the aircraft body. Johnson (1980) provides a complete theoretical description of A502, and Saaris (1992) gives instructions for its use. In the present study, separate lifting surfaces were used to define the slats, wing and individual flap elements. Wake surfaces were defined for carrying trailing vorticity downstream from the trailing edge of each lifting surface.

Although Mach number was an important variable in the wind tunnel tests, the present analysis was essentially incompressible, but with A449 using a Prandtl-Glauert compressibility correction to account for the effect of Mach number, and A502 a Gothert correction (closely related to the Prandtl-Glauert correction, but applied automatically to geometry prior to solution). Therefore, cases were analyzed at a single Mach number that matched a test condition, and the Prandtl-Glauert correction could be applied subsequently to get solutions for the various other

Mach numbers. The total effect of Mach number on the solutions (e.g. the difference in overall lift, local pressure, bound or trailing circulation) between fully incompressible and the maximum Mach = 0.26 was not more than 4%. For a given configuration, the greatest difference between solutions at conditions matching wind tunnel conditions were between the minimum Mach = 0.18 and maximum Mach = 0.24, and was less than 1.5%. Any difference due to compressibility correction was further reduced by analyzing at an intermediate Mach number (M = 0.20 for the majority of cases). The effect of Mach number on these solutions can probably be ignored.

These codes are known to over-estimate the lift generated by flaps as a result of strictly enforcing that flow remains fully attached to the upper surface of all flap elements, without boundary layer development. Thus, either a standard or configuration-specific schedule of flap angle reductions is typically applied to the geometric flap deflections to more closely approximate measured (wind tunnel or flight) loads with these codes. The flap deflections used in the present work are, therefore, lower than the angles that would be found on a wind tunnel model. Needing to introduce an empirical modification such as this into the analysis suggests that incremental results might be more reliable than absolute results.

Engine nacelles and thrust were not modeled, primarily because the effect of the flow-through nacelles used during relevant wind-tunnel testing was expected to be small, and because the codes do not possess great fidelity nor ease in modeling them.

The effects of tip devices (e.g. winglets, or the raked tip extension on the 767-400) were not addressed, since their influence on the flowfield near any flap would be small. The greatest effect of tip devices on the flap flowfield would come as a result of new nominal angles of attack and, perhaps new flap deflection schedules in operational service, but wind tunnel model parts and test conditions would not reflect such changes. Thus, some of the present results can have broader application than the aircraft models specified (e.g. the 767 results are applicable to both the 767-300 and 767-400 wind tunnel data).

While the geometric fidelity and smoothness of the singularity distributions within A502 and DACVINE are better than A449, they come at a cost of more work initially, greater computational time, and more extensive post-processing. However, recent independent effort within Boeing has reduced the pre-processing burden substantially.

Early in the project, results from both A502 and A449 were compared. The promise of greater fidelity from A502 was tempered by difficulty in eliminating unrealistic results at locations where separate lifting or wake surfaces came into close proximity. Such results were typically found near flap and slat edges, where results were critical and objectivity was preferred over results-based adjustments to the paneling. Ignoring these local "hot spots", the A502 results were not substantially different than A449 results over the majority of the span of the lifting surfaces and overall lift levels compared quite well, indicating that A449 could be adequate. This discovery, along with a fairly comprehensive existing set of geometric models prepared for A449 input, made A449 the preferred analysis tool.

Some arbitrariness is introduced in using these results to make estimates of shed vorticity and the flowfield at the flap ends. In both A449 and A502 solutions, the wake provides the spanwise distribution of shed circulation from the entire chord of a lifting surface. This should be a reasonable approximation to the spanwise distribution of wake circulation that could be measured in a wind tunnel test, or in flight, considering that the load distribution is not a bad model for the real load distribution. However, the potential flow model prevents shedding of vorticity from anywhere on a surface other than at the trailing edge, so it does not allow a vortex to develop along a flap side edge, as is known to occur in the real flow. One technique for estimating the strength of the flap edge vortex with these results could be to declare an arbitrary spanwise segment of the wake circulation distribution at the tip to be the flap side edge vortex. Perhaps the size of this spanwise region could be a fixed proportion of the flap chord, thus standardizing the process.

Another arbitrary choice is made in assigning the chordwise distribution of shed circulation using calculated results. The natural choice may be the chordwise panel strength distribution. In A449 this would be the vortex panel strength at the flap edge, and in A502 it would be the chordwise distribution of the spanwise gradient in doublet strength here, and it is approximately the chordwise load distribution. But the chordwise distribution of circulation from free vorticity at the flap edge in the real flow is typically not equivalent to the chordwise load distribution in the vicinity of the tip. Perhaps a model of the shed vorticity with a presumed distribution that is scaled by either the local or overall loading on the flap would be an appropriate means of estimating the characteristics of the flap edge vortex.

Extracting local velocity information from solutions also requires some arbitrary choice in the location where the solution is interrogated. This should be done with care since velocity

depends strongly on proximity to the surfaces and wakes. Consistency in the methods for estimating the strength and chordwise distribution of the flap side-edge vortices, and for extracting other flowfield information is important when making comparisons with acoustic measurements from the wind tunnel.

5.2 Navier-Stokes calculations

5.2.1 Overview

Two-dimensional Navier-Stokes calculations were undertaken for the purpose of calculating mean-flow parameters that are used in the slat source model. An unstructured-grid Reynolds-averaged Navier-Stokes solver (NSU2D) was used. For each airplane considered, a representative two-dimensional high-lift cross-section was constructed. To date, calculations have been completed for the following airplanes : 737-700, 757-200, 767-300, 777-200, DC-10/MD-11. For each airplane, calculations were undertaken for the particular set of Mach numbers, flap settings, and angles of attack for which baseline noise data was available. A total of 51 cases have been run so far. The following parameters have been extracted from the Navier-Stokes calculations : (i) Integrated vorticity (circulation) of the slat separation bubble, (ii) Mass flux through the slat gap, and (iii) lift coefficient for each high-lift element. Due to reasons stated in Chapter 1, not all these parameters are presently incorporated into the slat source model.

5.2.2 Two-dimensional profiles

A representative cross-section was taken for each airplane wing, approximately in the mid-span region, and away from any hinges or fairings. The cross-section was constructed as follows : (i) cut streamwise aft of the local quarter-chord point, (ii) cut normal to the cruise wing leading-edge forward of the quarter-chord point; (iii) rotate the forward part into the streamwise plane by rotating about a vertical line through the quarter chord; (iv) use the local chord of the cruise wing at the aft streamwise plane as the reference length for the section. This is a standard empirical procedure for obtaining representative two-dimensional profiles. An example is shown in Figure 5-1.

A list of reference lengths for the different airplane models is given in Table 5-2. The length L represents cruise wing chord at the streamwise plane corresponding to the cut. Reynolds numbers are also given for the various free-stream Mach numbers considered.

5.2.3 Running the NSU2D code

The NSU2D code solves the Reynolds-averaged Navier-Stokes equations in two dimensions, using an unstructured multi-grid methodology. The code was developed by Dimitri Mavriplis of *Scientific Simulations* (see Ref 5-4 for an example of an application). An advancing-front unstructured grid generator (AFLR2) was used to generate grids; this program was written by David Marcum of Mississippi State University. A typical grid is shown in Figure 5-1.

The solver was run in conjunction with the Spalart-Allmaras turbulence model. The solution strategy is to advance in time until a steady state is reached. Typically 400-500 steps were necessary for this purpose. The solution was taken to have converged to a steady state when variations in the lift coefficients dropped below 0.1%.

5.2.4 Special considerations

Since slat cove and gap flows are of special interest in these calculations, the grid was refined considerably in the neighborhood of the slat. A close-up of the slat region is shown in Figure 5-2. However, grid refinement is not necessarily confined to the slat region. Flow fields around different elements of a high-lift airfoil are typically strongly coupled. Consequently, the effects of insufficient resolution near one element often makes itself felt near other elements as well.

The price of extra grid points is extra run time, and sometimes, numerical divergence in the flow solver. In the latter case, a small adjustment in grid parameters usually alleviated the problem. It is also observed in some cases that a particular airfoil grid is suitable up to a certain angle of attack or inflow Mach number; beyond that point, the grid has to be slightly adjusted in order to avoid numerical divergence.

Thus while the grid and solver 'settings' were generally close to each other through the entire set of runs listed here, they are not totally consistent among airfoils, and sometimes vary for even a particular airfoil. However, the same overall convergence criterion – lift variation of less than 0.1% - was maintained throughout. Results of a typical calculation are shown in Figure 5-3.

5.3 References for this chapter

Ref 5-1 : Goldhammer, M. I., 1979, User's Manual for Computer Program A449B Advanced Lifting Surface methods, Boeing D6-46987

Ref 5-2 : Johnson, F. T., 1980, A General Panel Method for the Analysis and Design of Arbitrary Configurations in Incompressible Flows, NASA CR 3079

Ref 5-3 : Saaris, G. R., 1992, A502I User's Manual-PAN AIR Technology Program for Solving Problems of Potential Flow about Arbitrary Configurations, Boeing D6-54703

Ref 5-4 : Cao, H.V., and Kusunose, K., "Grid Generation and Navier-Stokes Analysis for Multi-Element Airfoils," AIAA Paper 94-0748, January, 1994.

Table 5-2 Navier-Stokes calculations, gross parameters

(L refers to cruise wing chord)

Airplane	L (inches)	L (m.)	M_inf	Re
737-700	145.1032	3.6866E+00	0.18	1.5457E+07
	145.1032	3.6866E+00	0.2	1.7174E+07
	145.1032	3.6866E+00	0.22	1.8892E+07
	145.1032	3.6866E+00	0.24	2.0609E+07
757-200	161.8094	4.1110E+00	0.18	1.7236E+07
	161.8094	4.1110E+00	0.2	1.9152E+07
	161.8094	4.1110E+00	0.22	2.1067E+07
	161.8094	4.1110E+00	0.24	2.2982E+07
777-200	244.196	6.2042E+00	0.2	2.8903E+07
	244.196	6.2042E+00	0.24	3.4683E+07
767-300	206.248	5.2400E+00	0.2	2.4411E+07
	206.248	5.2400E+00	0.24	2.9294E+07
	206.248	5.2400E+00	0.26	3.1735E+07
DC-10/MD-11	251.125	6.3802E+00	0.207	3.0763E+07
	251.125	6.3802E+00	0.259	3.8491E+07
	251.125	6.3802E+00	0.285	4.2355E+07

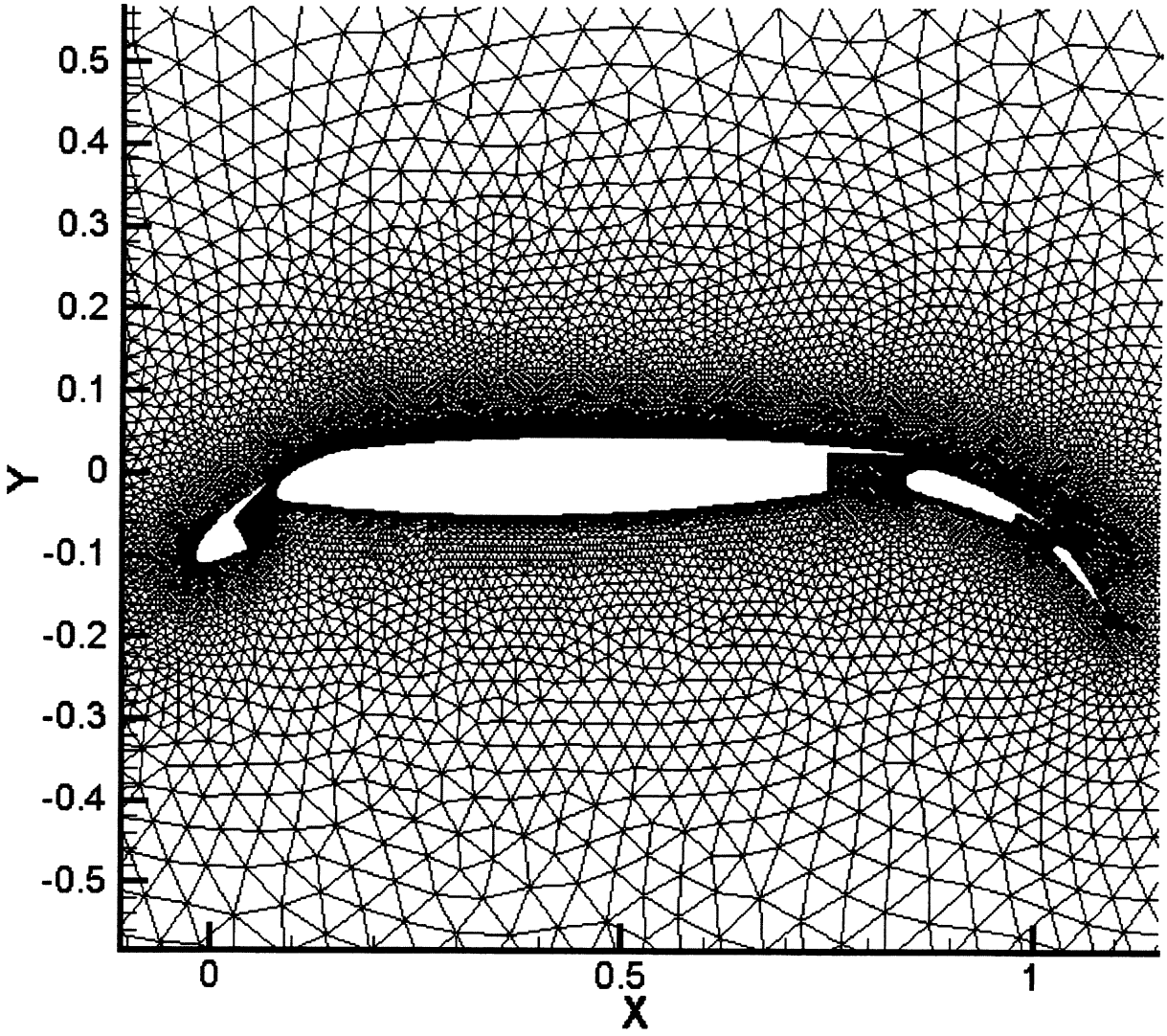

Figure 5-1 : 737-700 Flaps 30 cross-section and grid

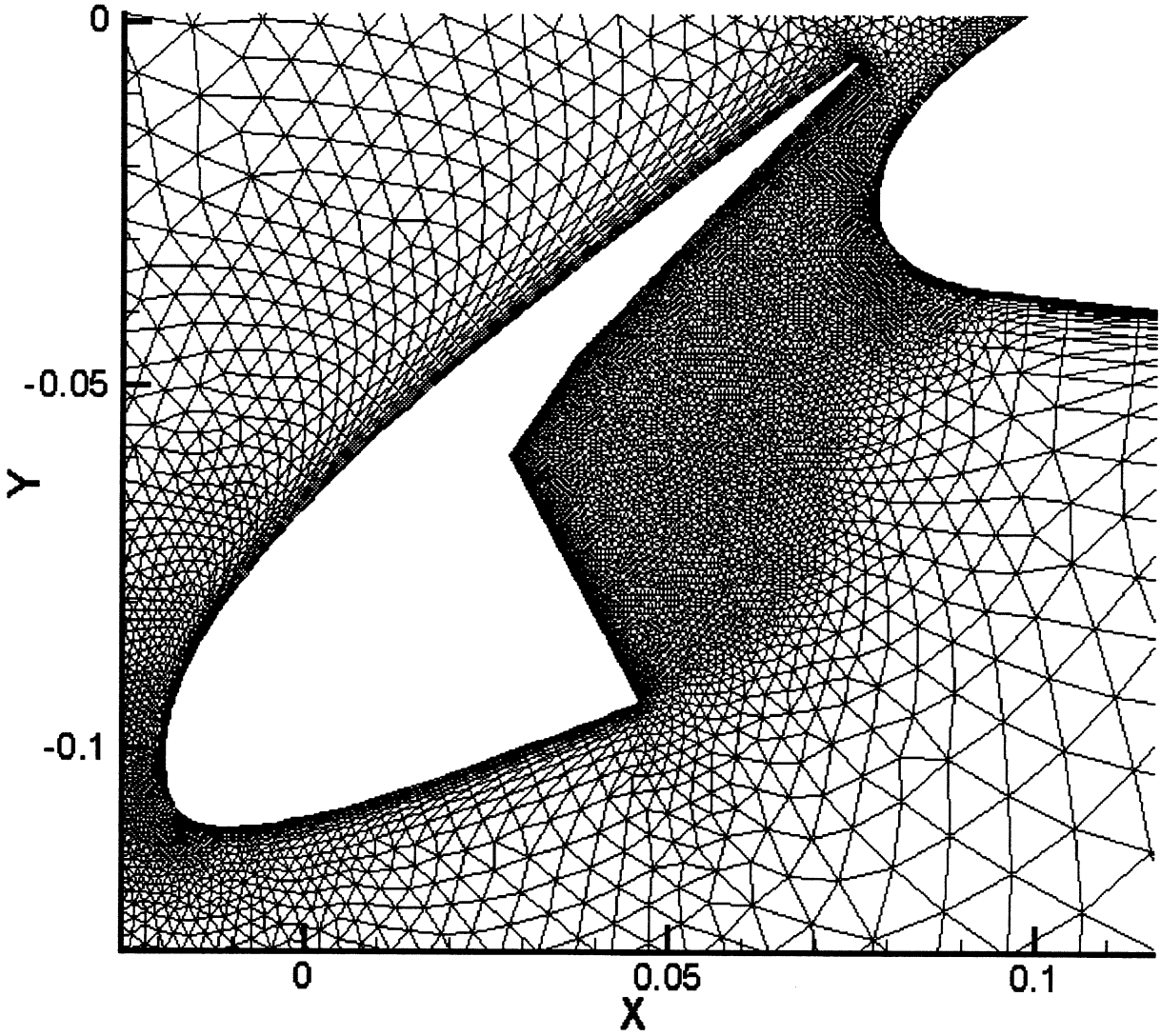

Figure 5-2 : Close-up of grid in slat cove, 737-700 airfoil

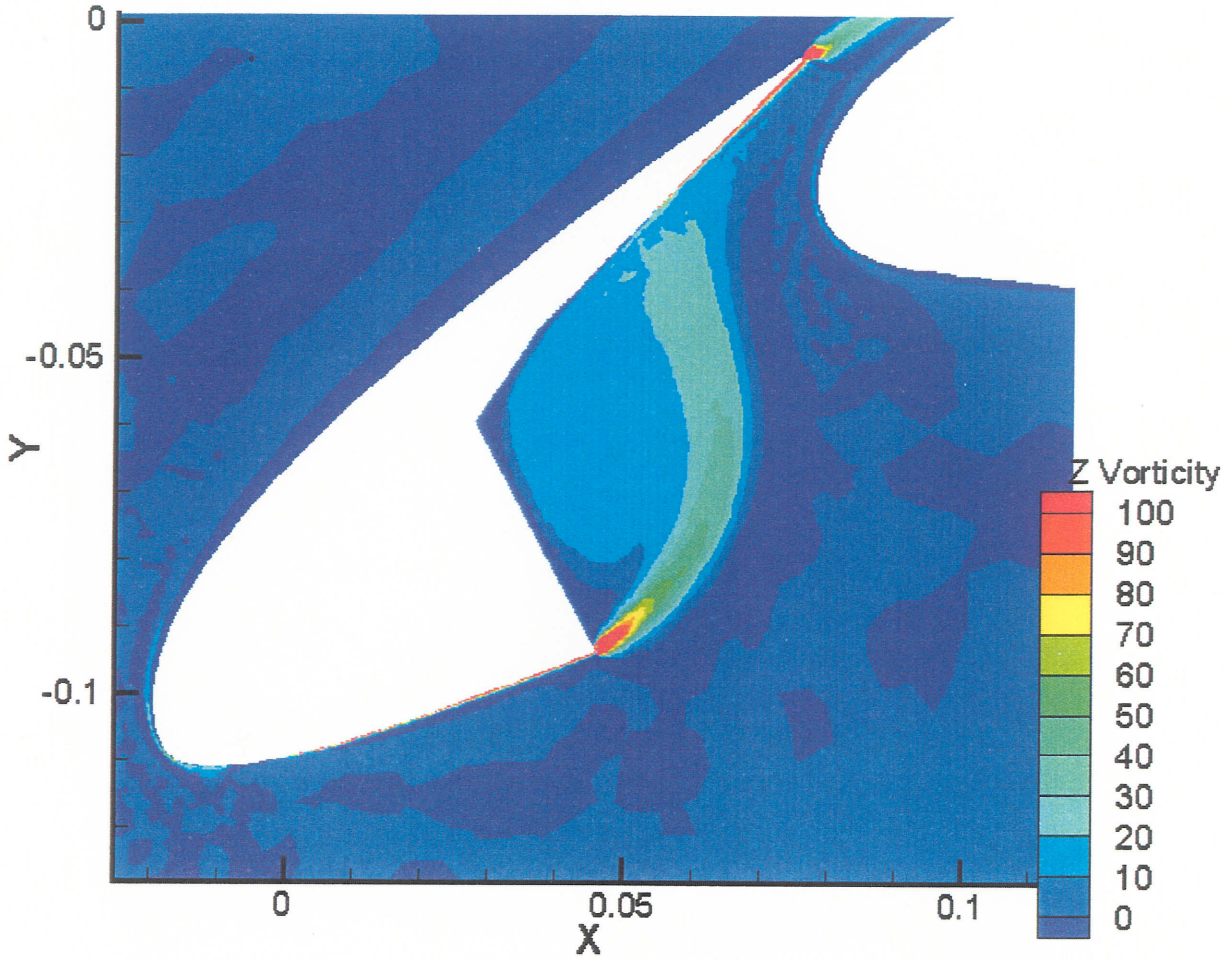

Figure 5-3 : Calculated vorticity (normalized), B737-700 airfoil

REPORT DOCUMENTATION PAGE

Form Approved
OMB No. 0704-0188

1. REPORT DATE *(DD-MM-YYYY)*	2. REPORT TYPE	3. DATES COVERED *(From - To)*
01- 09 - 2004	Contractor Report	

4. TITLE AND SUBTITLE
Airframe Noise Sub-Component Definition and Model

5a. CONTRACT NUMBER
NAS1-97040

5b. GRANT NUMBER

5c. PROGRAM ELEMENT NUMBER

6. AUTHOR(S)
Sen, Rahul; Hardy, Bruce; Yamamoto, Kingo; Guo, Yueping; and Miller, Gregory

5d. PROJECT NUMBER

5e. TASK NUMBER
Task 9

5f. WORK UNIT NUMBER
23-781-20-12

7. PERFORMING ORGANIZATION NAME(S) AND ADDRESS(ES)
NASA Langley Research Center
Hampton, VA 23681-2199

8. PERFORMING ORGANIZATION REPORT NUMBER

9. SPONSORING/MONITORING AGENCY NAME(S) AND ADDRESS(ES)
National Aeronautics and Space Administration
Washington, DC 20546-0001

10. SPONSOR/MONITOR'S ACRONYM(S)
NASA

11. SPONSOR/MONITOR'S REPORT NUMBER(S)
NASA/CR-2004-213255

12. DISTRIBUTION/AVAILABILITY STATEMENT
Unclassified - Unlimited
Subject Category 71
Availability: NASA CASI (301) 621-0390 Distribution: Nonstandard

13. SUPPLEMENTARY NOTES
Sen and Miller, Boeing Commercial Airplane Company; Hardy, Yamamoto, and Guo, Boeing Phantom Works.
Langley Technical Monitor: Robert A. Golub
An electronic version can be found at http://techreports.larc.nasa.gov/ltrs/ or http://ntrs.nasa.gov

14. ABSTRACT

Both, in-house, and jointly with NASA under the Advanced Subsonic Transport (AST) program, Boeing Commercial Aircraft company (BCA) had begun work on systematically identifying specific components of noise responsible for total airframe noise generation and applying the knowledge gained towards the creation of a model for airframe noise prediction. This report documents the continuation of the collection of databases from model-scale and full-scale airframe noise measurements to compliment the earlier existing databases, the development of the subcomponent models and the generation of a new empirical prediction code. The airframe subcomponent data includes measurements from aircraft ranging in size from a Boeing 737 to aircraft larger than a Boeing 747 aircraft. These results provide the continuity to evaluate the technology developed under the AST program consistent with the guidelines set forth in NASA CR-198298 entitled "Definition of 1992 Technology Aircraft Noise Levels and the Methodology for Assessing Airplane Noise Impact of Component Noise Reduction Concepts".

15. SUBJECT TERMS
Airframe noise; Flap edge noise; Gear noise; Slap noise; Trailing edge noise

16. SECURITY CLASSIFICATION OF:			17. LIMITATION OF ABSTRACT	18. NUMBER OF PAGES	19a. NAME OF RESPONSIBLE PERSON
a. REPORT	b. ABSTRACT	c. THIS PAGE			STI Help Desk (email: help@sti.nasa.gov)
					19b. TELEPHONE NUMBER *(Include area code)*
U	U	U	UU	102	(301) 621-0390